ROOM TEMPERATURE DYNAMICS OF QUANTUM EMITTERS THROUGH PHOTON EMISSION CORRELATION SPECTROSCOPY

Rebecca E. K. Fishman

A DISSERTATION

in

Physics and Astronomy

Presented to the Faculties of the University of Pennsylvania

in

Partial Fulfillment of the Requirements for the

Degree of Doctor of Philosophy

2024

Supervisor of Dissertation

Lee C. Bassett, Associate Professor of Electrical and Systems Engineering

Graduate Group Chairperson

Ravi K. Sheth, Professor of Physics and Astronomy

Dissertation Committee

Mariangela Bernardi, Professor of Physics and Astronomy
Cherie Kagan, Stephen J. Angello Professor of Electrical and Systems Engineering
Jay Kikkawa, Professor of Physics and Astronomy
Deep Jariwala, Associate Professor of Electrical and Systems Engineering

ROOM TEMPERATURE DYNAMICS OF QUANTUM EMITTERS THROUGH PHOTON EMISSION CORRELATION SPECTROSCOPY

Dedicated to my friends and family. I am so lucky!

ACKNOWLEDGEMENT

Physics can be an intimidating subject and I nearly did not major in it. Throughout my time studying physics, I have utterly relied on the support and wisdom of the friends I had along the way. Ty and Sophie, when I switched into honors physics in winter quarter knowing nothing about vector calculus, you welcomed me into your study group without hesitation. I remember moments of pure anxiety when faced with a pset that were alleviated by meeting up and working through it together. Sabrina, Juno, Alex, Brandon, Noah, and Martin also supported me in various ways in my physics journey at UChicago.

Jam and Helen, I'm so grateful you were in my cohort (and by pure luck chose to sit quite near me in the zoo), so we could journey through first year together.

David, Raj, and Yung, I literally could not have made it through grad school without you. Your mentorship and insight has shaped me as a researcher. Your feedback on my practice talks shaped the way I communicate science. It was an honor to collaborate with you scientifically and to call you my friends. Raj your unwavering support and encouragement have been instrumental to keeping my spirits afloat and my timeline on track. Yung your wisdom that you have shared with me has been a lifeline in times of fear and despair. I cannot thank you both enough.

Henry and Mathieu, you both make me laugh in different ways. Our chats in the lab would brighten my day. Jordan, Amelia, Sarah it's been a pleasure working with you, but even more fun was going to Candy Kitchen in Delaware together to stock up on candy for ICDS. Joey we've had great discussions these past few months. I can't wait to be at each of your defenses!

Emily, you made my life outside grad school a constant thrill (interspersed with long periods of silence as we'd sit in our dark living room on our computers). During those years, I couldn't wait to get home after the lab to do whatever activity we thought up or have whatever meandering, electrifying conversation that we'd fall into. I'm so happy we got to live the Golden Years together. I can't wait to start our commune.

Frances, in 2015 when I was on my first round of grad school applications, I sat at home for hours unable to start my personal statement. You met me at the Wormhole and sat with me as I wrote the first words. I don't know if you remember, but that day in the cafe, in gratitude, I said would dedicate my thesis to you. Little did I know at that moment that you would play a far larger support role to me in grad school. From your warm empathy and emotional support to the true joy of our shows, chats, and tumbles in the leaves, I am so grateful to have had you here in Philly these past two years.

Laura my sister, I love you so so much. I can't believe I hit the sibling jackpot in only one shot. It's such a beautiful thing how we support each other, and I know that if I call you when I'm down you can help me feel better. I can't believe what we've both gotten through separately and together in our grad school experiences, but now we are both coming out the other side and ready to realize the LoloBobo house of our dreams!

Mom and Dad, I owe so much to you. You have shaped my curiosity for nature, my sense of empathy, my sense of humor. You have raised me with the freedom to find my own way into whatever interests I had without requiring me to fit into any mold. You have always shown me unconditional love and support. Thank you for everything.

And finally, Bubbie, Grandpa, Grandma, and Pop Pop. I am where I am today because of all of you, and I owe aspects of my personality, interests, and life to each of you. I know if you could see me you'd be so proud just as I am proud to have been your grandchild.

ABSTRACT

ROOM TEMPERATURE DYNAMICS OF QUANTUM EMITTERS THROUGH PHOTON EMISSION CORRELATION SPECTROSCOPY

Rebecca E. K. Fishman

Lee C. Bassett

Photon emission correlation spectroscopy (PECS) is an indispensable tool for the study of atoms, molecules, and, more recently, solid-state quantum defects. In solid-state systems, its most common use is as an indicator of single-photon emission, a key property for quantum technology. Beyond single-photon purity, photon correlation measurements can provide a wealth of information that can reveal details about an emitter's electronic structure and optical dynamics that are hidden by other spectroscopy techniques. This thesis explores the application of PECS to study and understand the optical dynamics of quantum emitters. The first part of this thesis presents a guide to a standardized framework for using PECS to facilitate materials exploration for qubit candidates. This includes discussion of theoretical background, considerations for data acquisition and statistical analysis, and interpretation of PECS. It also illustrates how this experimental technique can be paired with optical dynamics simulations to formulate an electronic model for unknown quantum emitters. The second part of this thesis implements the practices discussed in the first part to explore the optical dynamics of two systems: the nitrogen-vacancy (NV) center in diamond and a quantum emitter in hexagonal boron nitride (h-BN). The NV center is a promising platform for applications in quantum sensing, quantum communication, and quantum networks. In particular, its spin and charge dynamics constitute useful attributes that can be harnessed for quantum control protocols. This thesis models and quantifies the transition rates that govern spin and charge dynamics in the NV center, utilizing PECS measurements, analysis, and simulations as a function of magnetic field, and excitation power. These findings can further inform the design of quantum control protocols. H-BN hosts pure single-photon emitters that have shown evidence of optically detected electronic spin dynamics. However, the electrical and chemical structure of these optically addressable spins is

unknown, and the nature of their spin-optical interactions remains mysterious. This thesis discusses time-domain optical and microwave experiments to characterize a single emitter in h-BN exhibiting room temperature optically detected magnetic resonance. It further discusses use of dynamical simulations to constrain and quantify transition rates in the model, and design of optical control protocols that optimize the signal-to-noise ratio for spin readout. This constitutes a necessary step towards quantum control of spin states in h-BN.

TABLE OF CONTENTS

ACKNOWLEDGEMENT iv

ABSTRACT vi

LIST OF TABLES x

LIST OF ILLUSTRATIONS xi

CHAPTER 1 : INTRODUCTION 1

CHAPTER 2 : MATERIALS EXPLORATION FOR QUBIT CANDIDATES 5

2.1 Introduction 5

2.2 Considerations for materials exploration 6

2.3 Tools for materials exploration 9

2.4 Conclusion 15

CHAPTER 3 : PHOTON EMISSION CORRELATION SPECTROSCOPY 17

3.1 Introduction 17

3.2 Theory 19

3.3 Experimental considerations 31

3.4 Analysis 40

3.5 Conclusion 47

CHAPTER 4 : OPTICAL DYNAMICS OF A NITROGEN-VACANCY CENTER 49

4.1 Introduction 49

4.2 Background 51

4.3 Methods 53

4.4 Analysis 56

4.5 Results and discussion 60

4.6 Future directions 69

CHAPTER 5 : OPTICAL DYNAMICS OF A SINGLE SPIN IN HEXAGONAL BORON NITRIDE 70

5.1 Experimental Characterization 70

5.2 Spin Structure 74

5.3 Optical dynamics 79

5.4 Simulations 82

5.5 Spin readout 85

5.6 Previous reports of single spins in h-BN 89

5.7 Conclusion 93

CHAPTER 6 : CONCLUSION 95

APPENDIX A : ALGORITHM FOR PROCESSING PHOTON CORRELATIONS 98

APPENDIX B : AKAIKE INFORMATION CRITERION 101

APPENDIX C : OPTICAL-DYNAMICS SIMULATION 102

APPENDIX D : QUANTUM EMITTER SEARCH THROUGH ANALYSIS OF PHOTOLUMINESCENCE IMAGES 104

APPENDIX E : DESIGN OF AN ULTRA-HIGH VACUUM CONFOCAL SETUP WITH A TUNABLE EXCITATION SOURCE 111

BIBLIOGRAPHY 117

LIST OF TABLES

TABLE 3.1 **Simulation parameters for Fig 3.6** 44

TABLE 4.1 **NV simulation parameters.** 68

TABLE 5.1 **Consistent findings in recent works.** 89
TABLE 5.2 **Parameters from Gaussian fit to ODMR data.** 90

TABLE D.1 **Emitter groups and representative SPE observed in PL images of nanodiamond and h-BN.** 108

LIST OF ILLUSTRATIONS

FIGURE 2.1 Spin-orbit interaction for various quantum emitters. 8
FIGURE 2.2 ZnS nanowires. 10
FIGURE 2.3 Non-exhaustive table of tools to study quantum emitters. 12

FIGURE 3.1 Experimental overview. 18
FIGURE 3.2 Histogram mode and full counting statistics comparison. 21
FIGURE 3.3 Output of time-tagged-time-resolved data processed for photon correlations shown for an example case of an emitter in h-BN with blinking. 32
FIGURE 3.4 Background and timing jitter correction to verify single-photon emission in hexagonal boron nitride (h-BN). 35
FIGURE 3.5 Effect of timing jitter on $g^{(2)}(0)$. 39
FIGURE 3.6 Simulated $g^{(2)}$ traces for four different physical models. 45

FIGURE 4.1 Optical dynamics of an NV center. 50
FIGURE 4.2 ESR 58
FIGURE 4.3 Excitation power correction. 59
FIGURE 4.4 Example $g^2(\tau)$ and saturation measurements 62
FIGURE 4.5 PECS fit parameters. 64

FIGURE 5.1 Optical characterization and ODMR. 71
FIGURE 5.2 Emission Polarization 73
FIGURE 5.3 Magnetic-Field-Dependent Optical Dynamics. 74
FIGURE 5.4 Resonance frequency at various dipole orientations. 75
FIGURE 5.5 B-field-dependent optically detected magnetic resonance. 75
FIGURE 5.6 Calculated metastable rates from 3-level approximation. 77
FIGURE 5.7 Simulation of PECS parameters for pumped and spontaneous k_{MG}. 77
FIGURE 5.8 Energy-level model and optical dynamics. 78
FIGURE 5.9 Antibunching Dynamics 80
FIGURE 5.10 Fluorescence recovery. 81
FIGURE 5.11 Optical Dynamics Model for Simulation. 83
FIGURE 5.12 Excitation-power-dependent bunching amplitudes with simulation results. . . . 86
FIGURE 5.13 Spin properties. 87
FIGURE 5.14 Signal-to-Noise Ratio. 88
FIGURE 5.15 Gaussian fits to ODMR data. 91

FIGURE E.1 C-WAVE laser system on optics table in Bassett lab. 112
FIGURE E.2 ARS cryostat on optical table in Bassett lab. 113
FIGURE E.3 Edwards turbo pump and pump cart with wide range gauge attached. 114
FIGURE E.4 Periscope design. 115

CHAPTER 1

INTRODUCTION

The use of quantum systems as fundamental components of quantum technologies (qubits) necessitates a way to manipulate, store, and read out a quantum state [41]. Systems with light-matter interfaces, such as solid-state quantum emitters, offer a mechanism through which light can be used to accomplish this. When an emitter's electronic or optical dynamics depend on internal orbital and spin states, these states also become accessible as matter qubits that can be manipulated with light. An optically-addressable spin qubit provides the advantage of insulation from electronic noise, allowing the storage or processing of quantum information, while the emitted photoluminescence gives a mechanism for reading out the spin state [8]. Such a configuration can enable a variety of quantum technologies [148]. However, different applications require different system properties. Therefore, it is crucial to thoroughly characterize solid-state quantum emitters to determine their suitability for applications.

When characterizing quantum emitters, the properties of the emitted light can be analyzed to reveal properties of the source. An emission spectrum indicates energy levels and decay processes in a source, emission intensity depends on transition rates between different states, polarization can give information about a source's dipole and physical orientation in a crystal, and most salient to this thesis, the time correlations of emitted photons can give information about the system's dynamics, revealing the rules and patterns that govern the changes in its states over time. Using light to study systems is called spectroscopy, and using light to study the time correlations of emitted light is called Photon Emission Correlation Spectroscopy or PECS. This thesis lies at the intersection of the emergence of PECS and the quantum revolution's quest for application-optimized qubits. In particular, it investigates, given photon time correlations from a quantum emitter, just how much information can be deduced about its full optical dynamics and its resulting suitability for particular applications in quantum information science.

The in-depth application of PECS to quantum information science is relatively new. However, a

trail of advances and discoveries enabled by the emergence of this technique illustrate its utility for studying quantum phenomena. When PECS was pioneered almost 70 years ago, it spurred unprecedented studies of quantum phenomena and inspired the development of the field of quantum optics. Up until the 1950s, scientists had only measured average intensities of light [54], obscuring any quantum features. All this changed when Hanbury Brown and Twiss took a new interferometer that they had developed to measure the diameter of radio stars and pointed it at a visible light source [106]. Their new interferometer looked at correlations between the arrival times of photons at two detectors, marking the first application of PECS. While they expected to observe no correlated photons from visible light sources, what they instead observed was a small increase in likelihood for two photons to arrive at both detectors at the same time compared to any other time separation [106]. This mysterious feature, which we now know as photon bunching from thermal light, was unexpected given the present scientific understanding of photon behavior [54]. Glauber, seeking to formalize the theory behind the observed photon correlations, authored a foundational 1963 paper [53], laying the theoretical framework for higher-order quantum correlation functions and launching the field of quantum optics.

With this new measurement technique and theory to study photon dynamics, PECS soon became a method for exploring previously unverifiable quantum mechanical properties. In 1977, Kimble *et al.* used PECS to observe emission from trapped ions and found a decreased likelihood that two photons would arrive at both detectors at the same time compared to any other time separation [78]. This phenomenon, termed photon antibunching, marked a groundbreaking confirmation of the quantum-mechanical nature of light [78, 145]. Numerous subsequent experiments followed revealing additional quantum phenomena such as quantum jumps [19] and non-classical light fields [49].

The use of PECS for studying optical dynamics of quantum systems evolved in the single-molecule spectroscopy community. In the 1990s when innovations in microscopy enabled a new realm of molecular physics [57], PECS presented as a useful tool to study optical dynamics and electronic structure of single-molecule systems [82]. This allowed for exploration of intra- and intermolecular dynamics [72] that had previously been unresolvable for systems with fast timescales or low quantum

yields [14]. Arguably, the most impactful application of PECS to single molecule spectroscopy is Fluorescence Correlation Spectroscopy (FCS), which is widely used to resolve physical and kinetic dynamics such as diffusion rates, molecule size and orientation, blinking, and binding kinetics [92, 45].

The emergence of quantum information science drove the application of PECS beyond single molecules to solid-state systems such as the nitrogen-vacancy (NV) center in diamond [82, 27] and quantum dots [93]. These systems promised potential platforms for single-photon sources that were more robust to photo-bleaching than molecules. The application of PECS to solid-state emitters has since grown to include many other materials as a part of the search for optimal platforms for quantum technologies. However, its main use remains as a cursory check for single-photon emission. While single-photon emission is a requirement for quantum applications, the potential of PECS can extend beyond this into detailed studies of the optical dynamics of quantum emitters. The challenge in exploring new materials and defect systems is that a plethora of dynamical phenomena, including radiative and non-radiative transitions between electronic levels, spin dynamics, intersystem crossings to metastable states, and ionization/recombination charge transitions, may occur under different conditions, or all in combination. Signatures of these phenomena manifest in the bunching dynamics of PECS measurements. As a result, PECS presents a versatile framework in which to hypothesize and test dynamical models.

While PECS has a long history of applications in different fields, there are a variety of considerations that are specific to its application to solid-state emitters. Experimental considerations such as background corrections may be more necessary when studying a defect in a crystal compared to, for example, a trapped atom. A commonly used criterion for confirming single-photon emission from solid-state quantum emitters assumes that multiple emitters of the same species would have identical emission, as would be the case for a more pure system such as trapped atoms or molecules. However, solid-state quantum emitters can be highly influenced by their local environment. As a result, quantum emitters with the same chemical structure can have different optical properties due to orientation in the crystal or environmental features such as strain or nearby defects. Ultimately,

it is time for a full adaptation of PECS for the specific case of quantum emitters.

The remaining chapters of this thesis seek to expand upon the application of PECS to solid-state emitters in the pursuit of quantum applications. Chapters 2 and 3 are largely pedagogical and lay the framework for best practices and considerations for applying PECS to aid in the process of materials exploration. Chapter 2 discusses a systematic approach to materials exploration, outlining objectives when characterizing new systems and how they can be realized through strategic application of available experimental and theoretical tools. Chapter 3 provides an in-depth guide to the use of PECS for studying solid-state systems including theory, experimental considerations, and analysis. Next, Chapters 4 and 5 draw from the methods described in the previous chapters and detail the application of PECS to two different qubit candidates. Chapter 4 demonstrates the application of PECS to a well known system, the nitrogen-vacancy Center, showing how PECS can clarify charge phenomena and model observed dynamics. Chapter 5 demonstrates the application of PECS and time-domain experiments to a newer system, hexagonal boron nitride, showing how these tools can be used to build a model for an electronic structure and optical dynamics. Finally Chapter 6 discusses conclusions and the future outlook for the application of this technique to the field.

CHAPTER 2

MATERIALS EXPLORATION FOR QUBIT CANDIDATES

2.1. Introduction

Quantum defects originate from substitutional atoms, vacancies, or impurity-vacancy complexes in solid-state lattices. They can exhibit quantum-coherent spin and optical properties, and thus comprise foundational elements in quantum information science [2, 6, 15]. When quantum defects with spin states couple coherently to light, they form a light-matter interface. Spin states are desirable as quantum-mechanical degrees of freedom because they are insulated from most environmental noise yet manipulable through spin resonance techniques, striking a balance between spin control and spin coherence [32]. Quantum defects can also exist in multiple stable charge states, especially in wide-bandgap host materials. Once a defect's spin and charge dynamics are understood and can be controlled, they present new opportunities for optical and electrical control.

Quantum defects are a subset of the larger category of quantum emitters, systems hosting discrete electronic states that interact with individual photons. Examples include quantum dots, which are highly optimized single-photon sources for quantum photonics [63, 44] and quantum communication [5, 150], fluorescent single molecules [17], and solid-state point defects [2]. Inspired by the well-known examples of quantum dots [120, 137] and diamond color centers [42, 112], the list of established quantum defect systems has grown to include defects in silicon carbide [10, 125, 108], emitters in layered materials [101] such as hexagonal boron nitride [87] and transition metal dichalcogenides [149], and rare-earth ions [131]. Despite promising applications, most solid-state defect systems remain unexplored due to the numerous host-defect combinations. However, exploration of these systems promises potential advantages for quantum-information applications in terms of scalability,

device integration, optical properties, spin properties, and quantum coherence [6, 15, 50].

2.2. Considerations for materials exploration

Several considerations come into play when searching for a quantum defect system for quantum information science. The properties of quantum defect systems and their corresponding advantages for applications stem from the interplay of material properties, defect properties, and material morphology [15]. Therefore, it is important to consider each of these factors.

The material properties of the host crystal play an important role in its ability to host viable quantum defects. In particular, semiconductors with large bandgaps are an important prerequisite for hosting sub-bandgap, optically addressable defect states. The spin-orbit interaction of a host material determines the feasability of optical control of the spin states of a quantum defect. Often, material properties will come with advantages and tradeoffs. For example, a high spin-orbit interaction, while beneficial for spin state control, also means that the spin state will be more sensitive to the orbital state of the system and thus have a shorter coherence time. The nuclear spin bath of the material will also have an affect on the spin coherence time. Therefore, semiconductors formed from elements with even numbers of valence electrons that have low concentrations of spin isotopes are ideal. Finally, the crystal structure determines the symmetry properties of the defect, which plays a role in determining the energy level structure and optical dynamics of the system. Other material properties such as piezoelectricity, dielectricity, and conductivity can affect optical properties. Practical considerations such as the availability of a material and the extent of existing reports on its properties also come into play.

For each host material that exhibits favorable properties, there are numerous species of defects within it that come with their own unique properties. While material properties are often well studied, the properties of individual defect species within materials are less studied and more difficult to model and understand. Often, complex calculations such as density functional theory are required to model the electronic levels that arise from a particular defect-host combination. The first prerequisite for a usable quantum defect is its presence in a host. To this end, calculations of formation energy can indicate whether a defect is likely to naturally occur or is possible to create at usable densities. The

next consideration is a system exhibiting electronic levels with favorable properties. The electronic level structure of a quantum defect determines whether a system is able to be optically initialized and whether it exhibits other features such as intersystem crossings or charge transitions.

A final consideration is the material morphology, as quantum defects arise or are fabricated in 0-Dimensional, 1-Dimensional, 2-Dimensional, and 3-Dimensional systems, each of which enables different practical and application-based schemes.

To illustrate the interplay of the material properties, defect properties, and material morphology, we discuss the three distinct systems featured in this thesis: zinc sulfide (ZnS) nanowires, the nitrogen-vacancy (NV) center in diamond, and quantum defects in hexagonal boron nitride (h-BN).

The NV center is among the most well-studied quantum defect systems. It consists of a substitutional nitrogen atom adjacent to a carbon vacancy. The large diamond bandgap of 5.4 eV allows it to host optically-addressable sub-bandgap states [154]. In its ionized state, NV^-, its energy-level structure consists of a $S = 1$ ground and excited state configuration with a metastable intersystem crossing [42]. Its defect properties include optically-addressible spin states that are coherent at room temperature and spin-dependent photoluminscence that can be controlled through optical and microwave pulses. Interactions between the NV-center and nearby nuclear carbon isotopes enable the formation of quantum registers in diamond as optically-interfaced quantum memories supporting multi-qubit quantum algorithms [34, 24, 37, 1]. Diamond's material properties also enable particular applications. Bulk diamond can be milled or detonanted to create low-cytotoxicity fluorescent nanodiamonds facilitating microscopic NV-center sensors that have advanced the field of quantum sensing [107, 95, 80]. However, diamond's high index of refraction makes it less efficient to couple light from the defect out from bulk diamond, which can necessitate additional fabrication such as solid-immersion lenses or metalenses [69].

H-BN is a two-dimensional van der Waals material, which, like diamond, has a large bandgap (5.955 eV [30]) that can host room-temperature optically-addressable states. In contrast to the NV-center in bulk diamond, h-BN's two-dimensional morphology allows more direct access to the light emitted

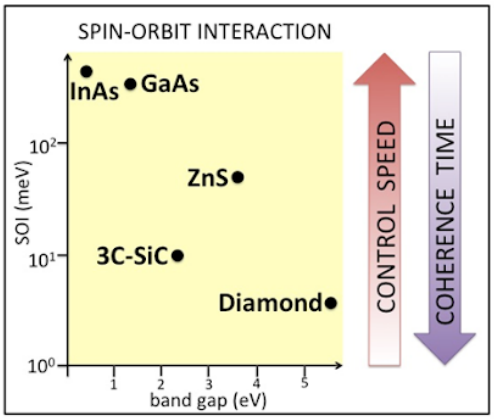

Figure 2.1: **Spin-orbit interaction for various quantum emitters.** InAs and GaAs quantum dots have high spin-orbit coupling strengths that facilitate high control speed but reduce spin coherence. On the other side, diamond has a low spin-orbit coupling that preserves coherence but does not enable fast spin control. ZnS lies in the middle providing a balance between the two competing capabilities of coherence and control.

from the defect. Additionally it's morphology provides distinct fabrication advantages through potential for integration into two-dimensional heterostructures. However, as a newer system than the NV-center, the chemical structure of its defects and their properties are less well understood. Reports have shown significant variation in properties of emitters in h-BN potentially due to strain effects and different species of defect. Furthermore, optically-addressable spin states have only recently been reported in isolated defects in h-BN [33, 127, 58]. While DFT analysis has identified several possible chemical structures [7, 73], none have been conclusively linked to the isolated spin defects. Therefore many questions remain regarding isolated spin defects in h-BN.

While quantum defects in diamond and h-BN have been studied for years, zinc sulfide one of numerous promising materials that is emerging as a potential host for quantum defects. To date, studies of ZnS for quantum information applications are still in the preliminary stages of quantum emitter search. While quantum emitters in bulk ZnS have not yet been reported, ZnS possesses a range of favorable material properties that make it a promising candidate. It exhibits a modest band gap (3.6 eV [43]) and a mid-range spin-orbit coupling interaction compared to other materials that host quantum emitters (Fig. 2.1). In addition ZnS possesses a low concentration of isotopes with nuclear spin

(<5% [143]), signifying marginal nuclear spin contribution to decoherence. ZnS can be produced in a variety of geometries including bulk crystal, 1D nanowires [12], and colloidal nanocrystals [138]. In terms of quantum defect synthesis, bulk crystal provides opportunity for ion implantation, and colloidal nanocrystals can be synthesized with specific properties [138]. Nanowires incorporate both the advantages of a small, 1D system in that they can facilitate evanescent confinement and thus can act as waveguides for visible to infrared light, while meanwhile still being large enough that they can easily be handled and manipulated within a lab setting [59]. This in conjunction with their high mechanical flexibility and strength enables straightforward incorporation into technological devices with low space and material requirements.

2.3. Tools for materials exploration

Once a material is selected for its favorable properties, a variety of tools can be employed systematically to find and characterize an emitter and begin to put together a model for its electronic structure and dynamics. When studying a system where quantum defects cannot be deterministically produced and localized, the first step in materials search is to locate a fluorescent point defect. Confocal microscopy provides a tool through which diffraction-limited, sub-bandgap fluorescence can be used to spatially pinpoint isolated fluorescent defects within a material. Further detail describing practical considerations for a confocal microscope can be found in Appendix E. Diffraction-limited emission suggests a localized point source in the sample, a prerequisite for the detection of a quantum defect. Properties of diffraction-limited spots including a two-dimensional-Gaussian profile and an emission-wavelength-dependent full-width half-maximum can serve as indicators when screening for emitters of interest. While this search is often done manually, automation through image analysis can be a useful tool to reduce the time requirements of the process [97]. For more details on quantum emitter search through analysis of PL images, see Appendix D.

Figure 2.2 shows an example of two images taken in the process of searching for point emitters in ZnS nanowires. In Fig. 2.2(a), the white light image shows how the nanowires appear under a white light microscope. A similar region is shown in Fig. 2.2(b), depicting a PL map of the same nanowires. An inset shows a circular spot with a sub-micron width. The spot's uniformity,

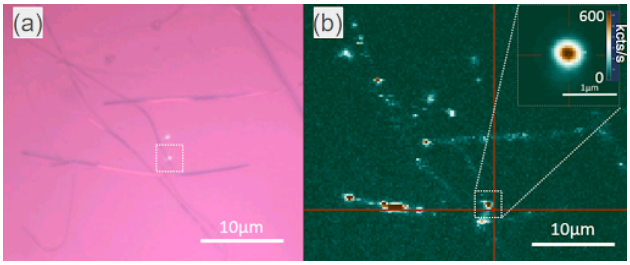

Figure 2.2: **ZnS nanowires.** (a) White-light image of ZnS nanowires. (b) Photoluminescence image of ZnS nanowires from a confocal scan taken with 532 nm excitation. Inset shows a confocal image of a diffraction-limited spot. White boxes show the location of the inset spot in (a) and (b). In the white box in (a), the bright spot shows the location of the excitation laser, and above the box, a refraction of the beam is also visible.

symmetry, and width indicate that it is likely diffraction-limited. However, there are additional considerations to determine the viability of these spots, including their stability and their optical properties. Therefore, following identification of a point emitter, the next step is to characterize the basic optical properties of the emitter. This is particularly essential for new material-defect systems such as ZnS and for systems with remaining unanswered questions about their fundamental properties such as quantum defects in h-BN.

One key property to evaluate at this stage is single-photon emission. A single-photon emitter (SPE) is a quantum system that emits one photon at a time. Single photons are a key requirement for many quantum information technologies [119, 123]. In particular, single-photon purity, the extent to which a system creates a pure, single-photon number state, influences the security of quantum communication protocols [85, 133] and error rates in photonic quantum computing and simulation [119]. High purity single-photon emission is also a prerequisite for realizing indistinguishable single photons [96], which form the basis for linear-photonic quantum information processing protocols [79, 116, 61] or quantum repeaters [105]. PECS is widely used to verify single-photon emission associated with quantum emitters [78, 27, 31, 92, 140, 81], as single-photon emission manifests in PECS measurements as an antibunching dip at zero delay. Characterizing antibunching through PECS also enables precise measurements of photon purity for SPEs [119].

In the case of the ZnS nanowires shown in Fig. 2.2, neither the pictured point emitter, nor any other

emitters in the sample showed evidence of single-photon emission. This indicates that the stable, diffraction-limited spots may have contained multiple point defects within the same diffraction limit or may have been produced from some other source such as debris on the sample. Additionally, the presence of stable defects - those that would not blink or bleach away when exposed to laser excitation - was rare, and varying the growth conditions, growth substrate, measurement substrate, and excitation wavelength did not reveal clear conditions for producing stable defects. This illustrates one of the challenges of new materials exploration, which is producing stable, single-photon emitters. Often, sample treatments such as high-temperature annealing or electron irradiation are employed as a part of a defect-stabilization protocol. Despite the difficulty in identifying single-photon emitters in ZnS nanowires, further effort toward understanding defect stabilization in nanowires, and exploration of the other morphologies of ZnS offer promise for progress toward quantum emitters in ZnS.

In the case that single-photon emission is observed, additional characterization measurements can begin to build a picture of the available electronic states and their transitions. Measurements of polarization-dependent PL intensity can give clarity on radiative transitions by revealing their symmetry. For polarization absorption measurements, the excitation polarization angle is varied, and the collected PL intensity is recorded as a function of excitation polarization angle. For polarization emission measurements, the sample is excited at a fixed polarization, and a filter in the collection path is varied to filter the PL emission according to polarization angle. These polarization measurements help clarify the number of dipole transitions and their orientations [99, 46]. Structured light beams with radial or azimuthal polarization can also reveal dipole orientation [132]. Knowledge of dipole orientation with respect to the crystal axes can help single out potential point groups and can be a key piece of information when considering chemical models in cases where the defect chemistry is unknown [76]. Additional information about higher lying excited states can be gained through polarization measurements at various excitation wavelengths in relation to the zero-phonon line [113, 77, 103].

Other typical characterization measurements include PL emission spectra and PL intensity as a

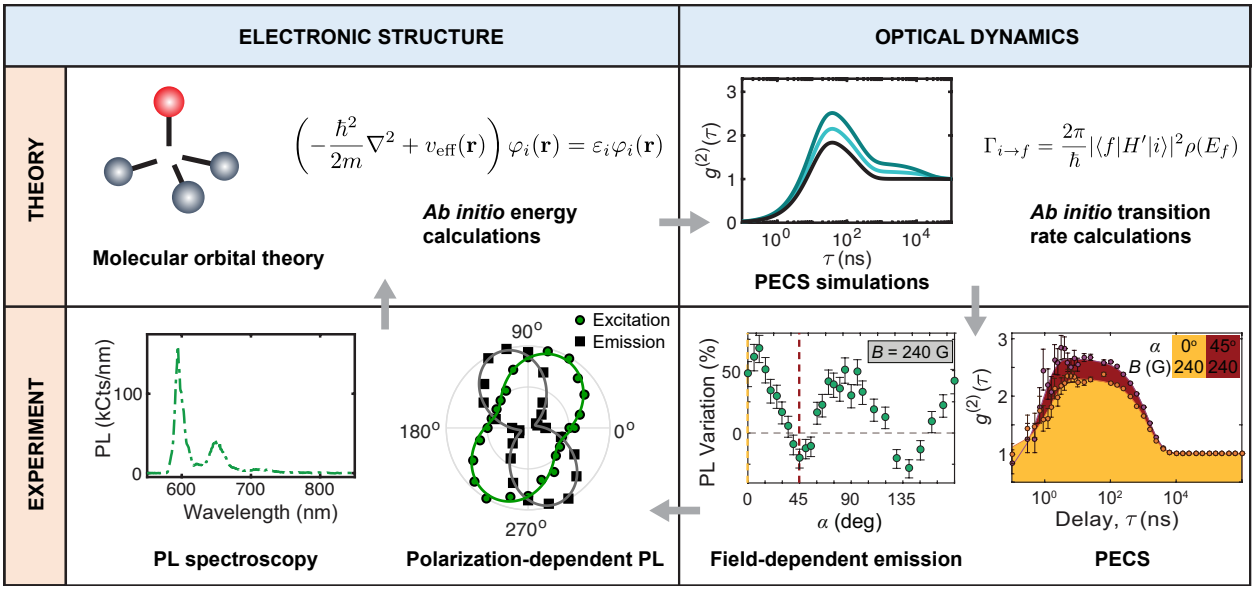

Figure 2.3: Non-exhaustive table of tools to study quantum emitters. A variety of techniques, both experimental and theoretical, can give information about a quantum emitter's electronic structure and optical dynamics. Tools that help clarify electronic structure include experimental techniques, such as PL spectroscopy and polarization-dependent PL, and theoretical techniques of molecular orbital theory and *ab initio* energy calculations. Tools that help uncover optical dynamics include theoretical techniques such as PECS simulations and *ab initio* transition rate calculations, which should be supplemented with experimental techniques such as field-dependent emission and PECS measurements. Images in the lower left quadrant depict h-BN data adapted from Patel *et al.* [103]. Images in the lower right quadrant depict h-BN data adapted from Exarhos *et al.* 2017 [48].

function of excitation power to characterize saturation. These preliminary measurements can provide information about radiative transitions such as number of transitions, their lifetimes, and the strength of vibronic coupling, but they give little insight into non-radiative transitions.

Figure 2.3 illustrates several experimental and theoretical techniques that can be used in conjunction to deduce the electronic structure and optical dynamics of a quantum emitter. While certain techniques yield more information on an emmiter's electronic structure, others are more suited to reveal optical dynamics. The lower left quadrant of Fig. 2.3, experimental techniques to study structure, depicts examples of spectroscopic techniques for initial defect characterization applied to an emitter in h-BN from Patel *et al.* [103]. In this work, the authors observe a single zero-phonon line and a phonon sideband consistent with a vibronic transition through a single optical dipole. This observation is further supported by the emission polarization measurement (black squares), which

shows high polarization visibility. However, the measured PL intensity as a function of excitation polarization (green circles) is not aligned with the emission, and the visibility is reduced. Hence, the optical excitation and emission do not occur through the same optical dipole transition. This measurement implies the presence of previously hidden excited states in the excitation pathway.

Initial characterization can also include measurements tailored toward specific properties of interest. For example, measurements that help identify optical spin signatures, such as magnetic-field-dependent PL can single out emitters with optically addressable spin states. Any features of interest that are identified in initial characterization steps can be expanded upon through additional study including acquisition and analysis of PECS as a function of external fields.

Photon emission correlation spectroscopy (PECS) is a valuable and often underutilized technique for elucidating a quantum emitter's optical and spin dynamics. PECS measurements involve analysis of photon time correlations to reveal different timescales of processes involved in a quantum defect's optical dynamics and their respective bunching amplitudes, which hold clues to the relative frequency of each process. As a steady-state measurement requiring only constant excitation, single-photon detectors, and suitable timing electronics, PECS is relatively simple to implement, and yet it can provide a wealth of information about an emitter's optical dynamics including excited-state lifetimes, radiative and non-radiative relaxation pathways, as well as spin and charge dynamics. Additionally, PECS measurements and simulations can be key to evaluating hypothesized models.

Measurements of PECS at different optical excitation powers and applied magnetic fields, unveil distinct dynamical processes, which are quantified in the changes in PECS timescales and bunching amplitudes. For example, Neu *et al.* measured PECS at different excitation powers to help develop an electronic model for silicon vacancy centers in diamond [98]. Their observation of a bunching timescale with a nonlinear power dependence led them to suggest an excitation-power-dependent de-shelving process involving an additional excited state. As another example, Patel *et al.* proposed an indirect excitation mechanism to account for a nonlinear power-dependence of the antibunching rate observed for several h-BN emitters [103]. Using PECS simulations, Patel *et al.* also clarified the effect of additional optically pumped transitions on the bunching rates and amplitudes. These simu-

lations allowed the authors to distinguish between emitters with metastable states accessed through optically pumped or spontaneous transitions. In general, power-dependent PECS measurements can reveal the presence of non-radiative states and their associated lifetimes.

Meanwhile, PECS measurements as a function of externally applied magnetic fields can reveal the energetics and dynamics of spin states. As an illustrative example, the lower right panel of Fig. 2.3 shows magnetic-field-dependent PL and PECS data from an h-BN emitter observed by Exarhos *et al.* [48]. In this case, the steady-state PL variations in response to applied dc magnetic fields suggested the presence of spin states and spin-dependent optical transitions. Field-dependent PECS measurements revealed that the decreases in PL were correlated with increases in bunching amplitude, but with no change in bunching timescale. Molecular orbital theory also provided some insight into the emitter's electronic structure. Using selection rules from the defect's symmetry group, the authors narrowed down the possible models to two options, which they were able to distinguish between through PECS simulation of both models. As a result, Exarhos *et al.* showed that the magnetic-field dependence of PECS bunching amplitudes and timescales was consistent with a spin-dependent intersystem crossing. Simulated PECS data can be empirically fit to quantitatively compare timescales and bunching amplitudes to those observed in experimental data. In addition, the measured PL data can be compared with simulations as a function of optical power or applied field.

Theoretical tools such as molecular orbital theory and *ab initio* calculations can be applied together with experimental techniques to construct a baseline model for the emitter's electronic structure. The host material's crystal structure and its point groups constrain the types of level structures that can exist within the material. The symmetries of the crystal lattice, supplemented with information about the optical dipoles and from analyzed photon emission statistics, can help narrow down model parameters including the number of electronic levels, the number of spin or charge manifolds, and the characteristics of transitions. Density functional theory can point to likely defect chemistries through quantitative estimates of formation energies, which can be compared with experimental spectroscopic measurements of the emitter to predict the likelihood of different defect candidates.

Dynamical information gained through PECS measurements and simulation can be further supplemented through *ab initio* calculations, which can give quantitative estimates of vibronic coupling strengths, electron capture rates, ionization cross sections, and nonradiative transition rates [3, 154].

2.4. Conclusion

Formulating a structural and dynamical model of a quantum emitter is crucial to harnessing properties for quantum technologies. Deeper understanding of a system allows its strengths to be connected with particular applications. For example, emitters hosting excited states with short optical lifetimes may be useful as single photon sources or in applications that require high signal-to-noise ratio such as quantum communication. Conversely, long-lived electronic spin states can serve as quantum memories for applications that require the storage of quantum states such as quantum registers for quantum repeaters. Even when the optical coupling to spin states is incoherent, as in the case of the NV center's intersystem crossing between triplet and singlet states, spin-dependent optical dynamics can be used for spin initialization [146] and readout [67]. Quantum sensing similarly takes advantage of the intrinsic sensitivity of orbital and spin states to external fields, together with optical readout [39, 135]. On the flip side, many defects feature distinct spin manifolds separated by electric-dipole forbidden transitions. Forbidden transitions to shelving states with long lifetimes can allow a state to be stored and protected in quantum memories [64].

The presence of charge states can enable additional functionality such as electrical generation of single photons [117] and long-term information storage [40]. Charge states coupled to spin states can also be harnessed to significantly improve the efficiency of state initialization [66] and optical readout [121] for quantum computing or quantum sensing, or to enable photoelectric spin readout in microelectronic devices [124]. More generally, detailed understanding of an emitter's electronic structure, along with radiative and non-radiative dynamics can also allow the design of additional resonant excitation schemes that improve spin readout efficiency [111] or achieve higher photon indistinguishability and entanglement [71].

Ultimately, controlling and harnessing a defect's quantum properties requires a detailed understanding of its electronic structure as well as its optical and spin dynamics, presenting formidable obstacles

for efficient experimental or theoretical characterization. The process of studying a quantum emitter using the tools in Fig. 2.3 should be iterated until there is enough experimental information to support a particular proposed model, and simulations can reproduce similar phenomena to those observed. The result may still be an approximation of the true underlying model. However, in revealing key properties of the emitter, the outcome of the combined experimental and theoretical approaches can provide enough of a foundation to begin to realize applications.

CHAPTER 3

PHOTON EMISSION CORRELATION SPECTROSCOPY

This chapter has been adapted with permission from R. E. K. Fishman *et al.* "Photon-Emission-Correlation Spectroscopy as an Analytical Tool for Solid-State Quantum Defects" *PRX Quantum* **4**, 010202 (2023) [51], published under a Creative Commons Attribution 4.0 International license (CC BY 4.0).

3.1. Introduction

This chapter describes the application of PECS as a general-purpose characterization tool for solid-state quantum emitters. We present application-specific guidelines for reliable data acquisition, analysis, and interpretation. In particular, we demonstrate how PECS can be used to reliably confirm single-photon emission and to hypothesize a model of the system's electronic states and optical dynamics, enabling an assessment of the emitter's suitability for quantum technology applications.

3.1.1. The autocorrelation function

While higher-order intensity correlations can be useful for studying many-body interactions and multi-photon states [128, 29, 4], the primary way of characterizing photon correlations is through the second-order intensity correlation function, often called the autocorrelation function. In its most general form, the autocorrelation function is given by

$$g^{(2)}(\tau) = \frac{\langle I(t)I(t+\tau)\rangle}{\langle I(t)\rangle^2}, \tag{3.1}$$

where $I(t)$ is the intensity at time t, τ is the time delay between two intensity measurements, and $\langle\rangle$ represents the time-average of the enclosed quantity [86]. Acquisition and analysis of $g^{(2)}(\tau)$ comprises the fundamentals of PECS.

There are two important types of correlations that can appear in a measurement of $g^{(2)}(\tau)$. Regions where $g^{(2)}(\tau) < 1$ indicate a decreased probability of detecting two photons separated by τ. This phenomenon is referred to as antibunching and corresponds to a quantum source with a

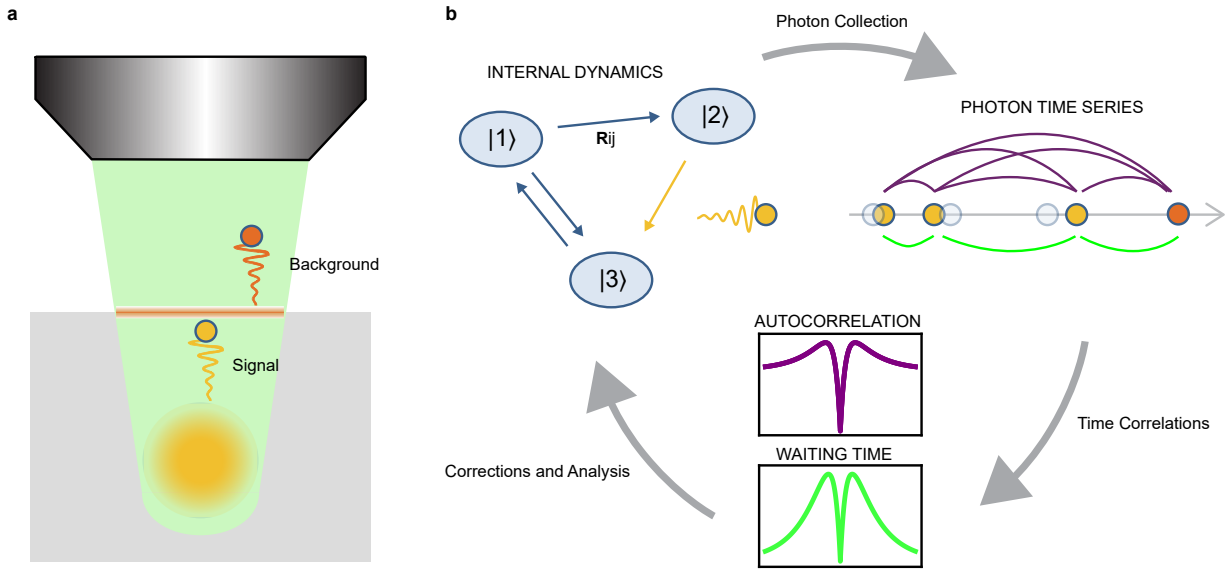

Figure 3.1: Experimental overview. (a) Laser light is focused through a microscope objective onto a quantum defect in a solid-state crystal (grey block). The resulting fluorescence from the defect is emitted isotropically and collected through the objective as the signal. Background photons arising from surface fluorescence and other fluorescent defects are also collected. (b) The full process of PECS is illustrated. Starting in the upper left, excitation from a laser source causes the system to evolve between different electronic states, emitting a photon when passing through a radiative transition. The emitted photons (yellow circles) are collected into a photon time series, which includes experimental noise such as timing error, represented by light grey circles, and background photons (orange circle). Time correlations are calculated between either all photons or only subsequent photons to make up the autocorrelation or waiting time distribution respectively. Corrections and analysis of the photon emission statistics helps paint a clearer picture of the emitter's internal dynamics model.

sub-Poissonian photon distribution [86]. Regions where $g^{(2)}(\tau) > 1$, indicating increased detection probability, are referred to as bunching and correspond to a super-Poissonian photon distribution. Any region where $g^{(2)}(\tau) = 1$ corresponds to uncorrelated, Poissonian light.

3.2. Theory

PECS involves exciting and collecting emission from quantum emitters, often using a confocal microscope, as shown in Fig. 3.1(a). The experimental situation is similar for different types of emitters, including quantum dots, single molecules, and quantum defects, since these are all much smaller than the optical diffraction limit. Figure 3.1(b) presents an overview of the acquisition and analysis of PECS data. The process begins with the internal dynamics of the quantum emitter system, which we assume is initially unknown. The evolution of this unknown system in response to excitation determines the timing of photon emission. The goal of PECS analysis is to infer the optical dynamics from the experimental data, and ultimately to develop a theoretical model for the quantum system.

3.2.1. Types of photon correlations

There are two types of photon intensity correlations that are often measured in experiments (see Fig. 3.2(a)). In addition to the autocorrelation function (Eq. 3.1), which represents the likelihood of receiving any two photons separated by a specific time delay, the waiting time distribution, $W(\tau)$, depends only on correlations between subsequent photons. Intuitively, $W(\tau)\mathrm{d}\tau$ represents the probability of detecting two subsequent photons with a time delay between τ and $\tau + \mathrm{d}\tau$. Hence, $W(\tau)$ depends both on the dynamics of the system of study and on details of the experimental setup, such as the collection efficiency. On the other hand, $g^{(2)}(\tau)$ captures correlations between all photons in the time series and reflects the full counting statistics of the system alone, independent of the collection efficiency.

Figure 3.2(a) depicts the experimental setups used to acquire $W(\tau)$ and $g^{(2)}(\tau)$. The optical excitation is the same for both cases as is the use of a beamsplitter in the collection path to address detector dead time (see Sec. 3.3). However, the manner in which the collected photons are processed differs. For $W(\tau)$, an incoming photon is registered as a start pulse, starting the clock until

a subsequent photon is registered as a stop pulse. This time difference is then collected into a histogram of photon time delays. As a result, the method of acquiring $W(\tau)$ is referred to as histogram mode. On the other hand, for $g^{(2)}(\tau)$, the arrival time of each photon is recorded, which requires a multi-channel, high-timing-resolution machine, such as a time-correlated single-photon counter, as well as additional processing to yield the correlations. While $W(\tau)$ is often simpler to acquire experimentally, $g^{(2)}(\tau)$ is more straightforward to analyze for meaningful results.

3.2.2. Two-level model

The internal evolution of an emitter's states is determined solely based on the initial conditions, electronic states, and transition rates between the states. Emission of a photon is dependent on which transitions are radiative. Therefore, an analytic expression that captures the photon time correlations must be a function of the state of the system over time and must reflect which transitions are radiative. The simplest model to consider is a two-level model, consisting of an excited state and a ground state. The system transitions from the ground state to excited state at a rate Γ_{ge} dependent on the excitation source, and then decays through a radiative transition from excited to ground at an intrinsic rate of Γ_{eg}, emitting one photon each time it decays. Initially, we assume unity collection efficiency (C=1) in which every transition from the excited state to the ground state corresponds to a detected photon. We will subsequently relax that assumption.

To derive an expression for $W(\tau)$ we must consider the probability of receiving the first subsequent photon at time t_2, given that a photon was received at time t_1. For a two-level model, this is equivalent to the probability of the system starting in the ground state at time t_1, then evolving to the excited state at time t after delay $\tau' = t - t_1$ and decaying back to the ground state at delay $\tau = t_2 - t_1$, integrated over all possible excitation times:

$$W(\tau) = \int_0^\tau d\tau' P_{e\to g}(\tau - \tau') P_{g\to e}(\tau'). \tag{3.2}$$

Here,

$$P_{a\to b}(t) = \Gamma_{ab} e^{-\Gamma_{ab} t}, \tag{3.3}$$

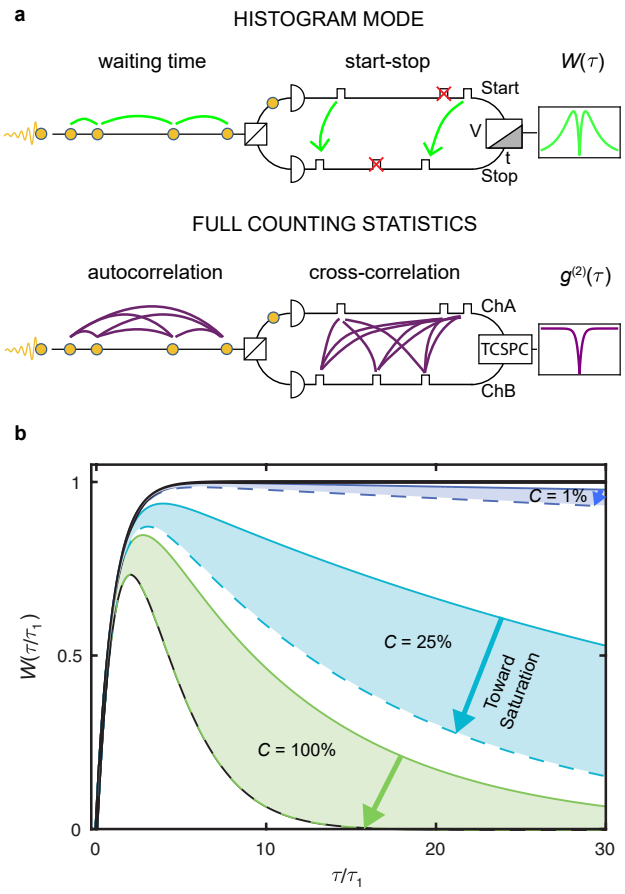

Figure 3.2: Histogram mode and full counting statistics comparison. (a) Schematic depicting the experimental setup for measuring histogram mode and the full counting statistics. A snapshot in time shows photons and electric pulses travelling left to right. A beamsplitter directs the photon stream into two separate detectors (semi-circles), each of which corresponds to a channel. In histogram mode, one channel acts as a start pulse for a ramp circuit and the other is a stop pulse. Additional start (stop) pulses that occur before (after) the stop (start) pulse are neglected. For the full counting statistics, a time correlated single-photon counter (TCSPC) tags the absolute times of photon arrivals at each channel. (b) The effect of collection efficiency and pump rate on the shape of the waiting time distribution for a two-level system. Collection efficiency is represented by differently-colored shaded regions, and pump rate relative to emission rate is represented on a spectrum from solid [maximally different pump and emission rates ($\alpha \to 1$)] to dashed [pump rate = emission rate ($\alpha = 0$)] lines. The solid black curve represents $g^{(2)}(\tau/\tau_1)$. The dashed black curve represents the waiting time distribution at unity collection efficiency and equal pump and emission rates, at which point it is the farthest from approximating $g^{(2)}(\tau)$. Traces have been normalized by pump rate and collection efficiency for ease of comparison.

is the normalized probability density function for a transition from state $|a\rangle$ to $|b\rangle$ with transition rate Γ_{ab}. Therefore, for a two-level system with unity collection efficiency, the waiting time distribution

is given by

$$W(\tau) = \frac{\Gamma_{ge}\Gamma_{eg}}{\Gamma_{ge} - \Gamma_{eg}}(e^{\Gamma_{eg}\tau} - e^{-\Gamma_{ge}\tau}). \tag{3.4}$$

To derive an equivalent expression for $g^{(2)}(\tau)$, we must consider the probability of receiving *any* photon at time t_2, given one was received at time t_1. For any model with a single radiative transition, this is equivalent to $P_e(t_2|P_g(t_1) = 1)$, the probability of being in the excited state at time t_2, given that the system was in the ground state at t_1. Normalized by the steady-state population of the excited state, P_e^{∞}, this gives the autocorrelation function,

$$g^{(2)}(\tau = t_2 - t_1) = \frac{P_e(t_2|P_g(t_1) = 1)}{P_e^{\infty}}, \tag{3.5}$$

so that $g^{(2)}(\tau) = 1$ corresponds to uncorrelated light and any deviations from 1 correspond to positive or negative correlations.

The time-dependent probability of each state's occupation is determined by the transition rates. Therefore, the probability of excited state occupation can be found by solving a system of coupled ordinary differential equations (ODEs), which for a two-level model is

$$\frac{dP_g}{dt} = -\Gamma_{ge}P_g(t) + \Gamma_{eg}P_e(t) \tag{3.6a}$$

$$\frac{dP_e}{dt} = \Gamma_{ge}P_g(t) - \Gamma_{eg}P_e(t). \tag{3.6b}$$

Solving with the initial conditions of

$$P_g(0) = 1, \tag{3.7}$$

results in the expression for autocorrelation from a two-level model,

$$g^{(2)}(\tau) = 1 - e^{-(\Gamma_{eg}+\Gamma_{ge})\tau}. \tag{3.8}$$

3.2.3. Collection-efficiency dependence

The deriviation of the waiting time distribution in Eqs. 3.2-3.4 assumes the condition of perfect collection efficiency. However, in a realistic experiment, the setup collection efficiency, C, significantly impacts the probability of receiving consecutive photons. Thus, a derivation of $W(\tau)$ that accurately captures experimental realities must incorporate C. For simplicity, we show the derivation for a two-level system with imperfect collection efficiency.

As with perfect collection efficiency, we consider the probability that the system starts in the ground state, evolves to the excited state, then decays back to the ground state after delay τ, emitting a photon. However, in this case the system can evolve through any number of cycles between excited and ground before the detection of a subsequent photon. Additional multiplicative factors, C and $1-C$, account for the respective probabilities that the subsequent photon is detected or is not detected once it is emitted, and we integrate and sum over all possible combinations of losing n photons before detecting the next photon. This is equivalent to the infinite sum of convolutions,

$$\begin{aligned} W(t) = \frac{C}{1-C}\Big(& (1-C)P_{g\to e}(t) * P_{e\to g}(t) + \\ & (1-C)^2 P_{g\to e}(t) * P_{e\to g}(t) * P_{g\to e}(t) * P_{e\to g}(t) \\ & + \cdots \Big), \end{aligned} \tag{3.9}$$

where $P_{a\to b}(t)$ is given by Eq. 3.3.

Equation 3.9 can be evaluated in Laplace space following the general relation for an infinite sum of convolutions of the same function, $h(t)$,

$$h(t) + h(t) * h(t) + \cdots = \mathcal{L}^{-1}\left\{ \frac{\mathcal{L}\{h\}(s)}{1-\mathcal{L}\{h\}(s)} \right\}(t), \tag{3.10}$$

where $\mathcal{L}$ is the Laplace transform and s is a complex frequency parameter.

Therefore, defining $h(t)$ as

$$h(t) = (1-C)P_{g\to e}(t) * P_{e\to g}(t), \tag{3.11}$$

the probability that the system evolves but a photon is not received, yields the collection-efficiency dependent expression for $W(\tau)$ for a two-level system,

$$W(\tau) = \frac{2C\Gamma_{eg}\Gamma_{ge}}{\sqrt{-4C\Gamma_{eg}\Gamma_{ge} + (\Gamma_{eg} + \Gamma_{ge})^2}} e^{-\frac{\Gamma_{eg}+\Gamma_{ge}}{2}\tau} \sinh \frac{1}{2}\sqrt{-4C\Gamma_{eg}\Gamma_{ge} + (\Gamma_{eg} + \Gamma_{ge})^2}\tau. \tag{3.12}$$

This relation between C and $W(\tau)$ for a two-level model is illustrated in Fig. 3.2.

3.2.4. Generalizing to models with $n > 2$ levels

In order to capture more complicated dynamics, models with $n > 2$ levels are necessary. Experimentally observed optical dynamics can often be the product of multiple electronic levels involving additional radiative and non-radiative transitions.

One example of a multi-level model, a three-level model, might include a two-level model with an additional non-radiative pathway from the excited state to a third metastable state, then to the ground state. In the following, we will consider the general cases of multi-level models with a single radiative transition and unity collection efficiency.

In the case of $W(\tau)$, the addition of non-radiative decay pathways requires accounting for all possible combinations of non-radiative loops through electronic states that can occur before the emission of a second photon after delay τ. For a general system with n possible non-radiative decay pathways from the excited state back to the ground state,

$$W(\tau) = P_{g\to e}(\tau) * P_{e\to g}(\tau) * \left(1 + \sum_{k=1}^{\infty}\left[\left(\sum_{i=1}^{n} h_i(\tau)\right)^{*k}\right]\right). \tag{3.13}$$

Here $h_i(\tau)$ is the probability density function for evolution through each non-radiative decay loop, i, starting and ending in the ground state with a total duration τ, and

$$h(\tau)^{*n} = \underbrace{h(\tau) * h(\tau) * ... * h(\tau)}_{n}. \tag{3.14}$$

The prefactor of Eq. 3.13 represents the PDF of travelling through the radiative loop one time, while the part enclosed in parentheses represents all possible combinations of non-radiative loops. With increasingly complex models, evaluating $W(\tau)$ quickly becomes intractable.

Here we consider the most basic example of a three-level model with both a radiative and non-radiative pathway to the ground state and perfect collection efficiency. As with the derivation for imperfect collection efficiency, there is a need to account for all cases where the system evolves to the ground state, but a photon is not detected. In this case, a delay in receiving a subsequent photon stems from the non-radiative transition through a third, metastable state to the ground state. The system can evolve through any number of non-radiative cycles prior to the emission of a subsequent photon.

Starting with Eq. 3.13, we define the probability density function of a full non-radiative cycle from ground state to excited to metastable back to ground as,

$$h(t) = P_{g\to e}(t) * P_{e\to m}(t) * P_{m\to g}(t), \tag{3.15}$$

where the subscript, m, indicates the metastable third state. The waiting time distribution for a three-level model is then given by,

$$W(t) = P_{g\to e}(t) * P_{e\to g}(t)(1 + h(t) + h(t) * h(t) + \cdots), \tag{3.16}$$

which can be evaluated using Eq. 3.10. Additional model complexity such as other nonradiative decay pathways or imperfect collection efficiency further complicate the derivation of $W(\tau)$. However, such features are common in realistic models. As a result, autocorrelation presents a more tractable tool for measuring the optical dynamics of realistic models.

While $W(\tau)$ requires a unique derivation for each specific electornic model, generalizing $g^{(2)}(\tau)$ to multi-level models is more straightforward. As in the case of the two-level model, for any n-level electronic structure, the full dynamics are given by a system of n coupled differential equations.

This system of equations can be summarized by the rate equation

$$\dot{P} = GP, \tag{3.17}$$

where P is a vector of state occupation probabilities and G is the transition rate matrix. Each off-diagonal element of the rate matrix, G_{ij}, where $i \neq j$, is the total transition rate into state $|i\rangle$ from state $|j\rangle$. Each diagonal element $G_{ii} = -\sum_{j \neq i} G_{ji}$ is the total transition rate out of state i and thus preserves probability. Examples of transition rate matrices are further discussed in Sec. 3.4.1. The time-dependent population of each state can be obtained by solving Eq. 3.17 with the initial condition set immediately following emission of a photon (Eq. 3.7 for systems with a single ground state, and Eq. 3.21 for multiple ground states). $g^{(2)}(\tau)$ can then be calculated from Eq. 3.5, letting P_e be the population of the excited state from which the radiative transition occurs.

3.2.5. Autocorrelation from multiple radiative transitions

So far, we have simplified the discussion by limiting it to models with a single radiative transition. While this suffices in many situations, it also is common for systems to have multiple radiative transitions whether they be due to different spin states or charge manifolds or some other mechanism. In all cases the transition rate matrix, G, still determines the state evolution according to the rate equation, Eq. 3.17. However, the initial condition, P_0, which is the state immediately following photon emission, is dependent on which transitions are radiative. Similarly, optical dynamics such as intensity are also affected, which in turn impacts the autocorrelation function.

In order to account for the effect of multiple radiative transitions on $g^{(2)}(\tau)$, we introduce the transition collection efficiency matrix, C. C is made up of individual elements, C_{ij}, that give the probability of detecting a photon from each transition from state j to state i. C_{ij} can take on values from 0 to 1 with fractional values accounting for different collection efficiencies for different transitions, which might arise from polarization selection rules or different emission wavelengths.

With the collection efficiency matrix defined, PL can be calculated. The steady-state rate at which photons are detected from a transition j to i (I_{ij}) depends on the steady-state population of state

j (P_j^∞), the transition rate from the state j to state i (G_{ij}), and the probability of collecting a photon from that transition (C_{ij}):

$$I_{ij} = C_{ij} G_{ij} P_j^\infty. \tag{3.18}$$

The total steady-state photoluminescence (I_{PL}), which is the average rate at which photons are detected from any transition, is given by summing over the photon detection rates from all transitions,

$$I_{PL} = \sum_{ij}^{n} I_{ij}. \tag{3.19}$$

Therefore the probability of detecting a photon from a specific transition from j to i ($P_\gamma^{\infty(j\to i)}$) is given by the fractional contribution of that transition to the total PL:

$$P_\gamma^{\infty(j\to i)} = \frac{I_{ij}}{I_{PL}} = \frac{C_{ij} G_{ij} P_j^\infty}{\Sigma_{ij}^n C_{ij} G_{ij} P_j^\infty}. \tag{3.20}$$

As a result, the distribution of states following the detection of the photon is a column vector, P_0, with components given by the probability of detecting a photon from any transition into state i,

$$P_0^i = \sum_{j}^{n} P_\gamma^{\infty(j\to i)} = \sum_{j}^{n} \frac{C_{ij} G_{ij} P_j^\infty}{\Sigma_{ij}^n C_{ij} G_{ij} P_j^\infty}. \tag{3.21}$$

As discussed in the main text, the autocorrelation function is proportional to the probability of receiving any photon at time t_2, given one was received at time t_1. Therefore, writing $g^{(2)}(\tau)$ for multiple radiative transitions requires accounting for the time-dependent populations of all radiative states and the transition rates and collection efficiency of the transitions out of those states. With the initial state given by Eq. 3.21, and properly normalized to the steady-state, this gives the equation for autocorrelation from multiple radiative transitions:

$$g^{(2)}(\tau = t_2 - t_1) = \frac{\Sigma_i^n \Sigma_{j\neq i}^n C_{ij} G_{ij} P_j(t_2 | P(t_1) = P_0)}{\Sigma_i^n \Sigma_{j\neq i}^n C_{ij} G_{ij} P_j^\infty}. \tag{3.22}$$

In the case of a single radiative transition, this reduces to Eq. 3.5.

3.2.6. Relationship between $W(\tau)$ and $g^{(2)}(\tau)$

$W(\tau)$ and $g^{(2)}(\tau)$ can be analytically related, as both sets of correlations originate from the same physical process, and the correlations contained in $W(\tau)$ make up a subset of all those included in $g^{(2)}(\tau)$. As a result, $g^{(2)}(\tau)$ can be constructed from $W(\tau)$ through an infinite sum of self-convolutions [28]

$$\begin{aligned} g^{(2)}(\tau) &= W(\tau) + W(\tau) * W(\tau) + \cdots \\ &= \mathcal{L}^{-1}\left\{\frac{\mathcal{L}\{W\}(s)}{1-\mathcal{L}\{W\}(s)}\right\}(t), \end{aligned} \tag{3.23}$$

where $\mathcal{L}$ is the Laplace transform and s is a complex frequency parameter. This is due to the fact that the probability of receiving two photons separated by time τ with m intermediate detection events is equivalent to m convolutions of the probability of receiving consecutive photons.

Equation 3.23 shows how $W(\tau)$ can be thought of as a first order approximation of $g^{(2)}(\tau)$. This relationship has led to the occasional practice of using $W(\tau)$ and $g^{(2)}(\tau)$ interchangeably in experiments. However, $W(\tau)$ depends dramatically on the apparent brightness of the signal, while $g^{(2)}(\tau)$ does not. Therefore, the accuracy of this approximation is tied to the setup collection efficiency, C, and α, the relation between the pump rate (Γ_{ge}) and radiative decay rate (Γ_{eg}),

$$\alpha = \frac{|\Gamma_{eg} - \Gamma_{ge}|}{\Gamma_{eg} + \Gamma_{ge}}, \tag{3.24}$$

both of which impact apparent brightness.

Fig. 3.2(b) illustrates the effect of C and α on the shape of $W(\tau)$ and its comparison to $g^{(2)}(\tau)$ (solid black line) for a two-level model. Each shaded region depicts a set of $W(\tau)$ curves at a particular C, as a function of α. Within a shaded region, the shape of $W(\tau)$ ranges from a solid colored line, representing $W(\tau)$ for a system in which the pump rate is significantly higher or significantly lower than the decay rate ($\alpha \to 1$), to a dashed line, representing a system in which the two rates are equal ($\alpha = 0$). A lower collection efficiency generally leads to a closer approximation of $g^{(2)}(\tau)$. On

the other hand, adjusting the excitation power so that the pump rate approaches the emission rate causes $W(\tau)$ to diverge from $g^{(2)}(\tau)$. The difficulty in determining the experimental quantities of C and α make it challenging to assess the validity of approximating $g^{(2)}(\tau)$ with $W(\tau)$ in practical situations. Further, the dependence of $W(\tau)$ on these three independent variables make it difficult to decouple collection efficiency from transition rates when measuring an unknown system. For this reason, it is almost always preferable to acquire $g^{(2)}(\tau)$ for quantitative analysis. Therefore, the remainder of this text will focus on the use of $g^{(2)}(\tau)$.

3.2.7. Single-photon emission

PECS is an ideal measurement to characterize single-photon emission. An ideal SPE can only emit one photon at a time, and hence the probability to observe two photons with zero delay, and correspondingly $g^{(2)}(0)$, must equal zero. This fact is typically justified by quantum optics arguments. For a photon number state $|n\rangle$ with exactly n photons,

$$g^{(2)}(0) = \frac{\langle \hat{n}(\hat{n}-1)\rangle}{\langle \hat{n}\rangle^2} = \frac{(n-1)}{n}. \tag{3.25}$$

Using this relationship, it is apparent that $g^{(2)}(0) = 0$ for $n = 1$ and that $g^{(2)}(0) \geq 0.5$ for $n \geq 2$. Hence, it has become common practice to check whether an emitter's measured $g^{(2)}(0)$ is less than 0.5.

However, the use of the so-called "0.5 criterion" is questionable, since it does not accurately reflect the situation encountered in most experiments with quantum emitters. As derived, Eq. 3.25 applies to photon number states, which only occur if photons are emitted by identical, two-level emitters into the same spatial and temporal modes [86]. In typical experiments, however, uncorrelated emission from n independent, nonidentical emitters does not create photon number states. Hence, the criteria for establishing single-photon emission needs to be re-evaluated.

Generalizing Eq. 3.5, the autocorrelation function measured from n emitters is proportional to the sum of a correlated probability that two photons are received from the same emitter and an uncorrelated probability that two photons are received from different emitters. In the case where

emitter i has brightness I_i this gives

$$g^{(2)}(\tau; n) = \sum_{i=1}^{n} \frac{I_i}{\sum_{k=1}^{n} I_k} \left(\frac{(P_e^i(t_2|P_g^i(t_1) = 1)}{P_e^{i,\infty}} + \sum_{j \neq i}^{n} \frac{I_j}{\sum_{k=1}^{n} I_k} \right). \tag{3.26}$$

As τ approaches 0 (as t_2 approaches t_1), the first term goes to zero, giving the normalized expression for $g^{(2)}(0)$ from multiple emitters:

$$g^{(2)}(0; n) = \frac{\sum_{i=1}^{n} \sum_{j \neq i}^{n} I_i I_j}{(\sum_{k=1}^{n} I_k)^2} = \frac{(\sum_{k=1}^{n} I_k)^2 - \sum_{k=1}^{n} I_k^2}{(\sum_{k=1}^{n} I_k)^2}. \tag{3.27}$$

For n emitters with identical brightness, $I_j = I \forall j$, this derivation returns Eq. 3.25. However, Eq. 3.25 *only holds* in the case of emitters with identical brightness. For example, in the case where n=2, Eq. 3.27 reduces to

$$g^{(2)}(0; 2) = \frac{2 I_1 I_2}{(I_1 + I_2)^2}. \tag{3.28}$$

If $I_2 > I_1$ such that $I_2 = I_1 + \delta$, we find

$$g^{(2)}(0; 2) = \frac{1}{2 + \frac{\delta^2}{2 I_1 (I_1 + \delta)}}. \tag{3.29}$$

The second term in the denominator is always positive, and hence $g^{(2)}(0) < 0.5$.

Quantum emitters are typically not identical. Even when they are the same species, a variety of factors, including proximity to surfaces and alignment of the excitation or emission dipoles, can influence their observed brightness. Hence, the $g^{(2)}(0) < 0.5$ criterion is insufficient to identify single-photon emitters. It can be erroneously satisfied even when multiple emitters are present.

In contrast, a measurement of the ideal relationship $g^{(2)}(0) = 0$ would confirm single-photon emission. In order to apply this stricter criterion to experiments, it is necessary to account for systematic and stochastic errors that can lead to measurements of $g^{(2)}(0) > 0$ even for a SPE. The next section shows how to account for these effects, in order to achieve values of $g^{(2)}(0) = 0$ within quantified

uncertainties for a SPE.

3.3. Experimental considerations

Experimental acquisition and analysis of photon emission statistics present a number of challenges that must be considered in conjunction with the idealized theory from the previous section. A proper experiment involves processing significant amounts of data, and one must account for the timing resolution of detectors and correct for systematic experimental artifacts. Here we discuss the experimental setup for the collection of photon emission statistics, highlight an efficient algorithm to aid in calculating $g^{(2)}(\tau)$ from photon arrival times, and describe how to correct for the dominant sources of experimental error, *i.e.*, background photons that did not come from the emitter and detector timing jitter.

3.3.1. Acquisition

Photon emission statistics measurements of quantum emitters are typically acquired using a confocal microscope. In contrast to a wide-field microscope, a confocal arrangement rejects background emission from regions of the sample outside a diffraction-limited volume around the emitter of interest, and it directs the collected photons to a single detector channel that can be optimized for detection efficiency and timing resolution. Most detectors suffer from dead time, which is a period following each photon detection event during which the detector is blind to subsequent photons. In order to measure dynamics within the detector dead time, a beamsplitter is introduced in the emission path, directing the photon stream into two different, but nearly identical, detectors (see Fig. 3.2(a)). In this way, the autocorrelation function of the original photon stream is directly related to the cross-correlation function calculated across the two detectors, each corresponding to a channel. While $W(\tau)$ can be acquired by measuring only relative times through start-stop collection, $g^{(2)}(\tau)$ requires time tagging each photon detection event and subsequently calculating the photon correlations across the two channels.

3.3.2. Data processing

A brute-force calculation of the cross correlation function for large set of time-tagged data is extremely time consuming even for modern computers. Fortunately, Laurence *et al.* described a more

efficient algorithm [83]. Rather than individually iterating through all photon pairs between channels and binning the results into the photon correlation function, Laurence *et al.*'s algorithm uses the fact that the data are sorted in time to substantially reduce the processing time. Their method also allows for arbitrarily defined bins that are not equally sized. The algorithm offers options of both log and linear processing of the correlations with examples of the resulting outputs shown in Fig. 3.3(a) and inset respectively. Linear binning allows for resolution of features at low times and log binning allows for resolution of timescales at both short and long times. Log binning is achieved by pre-defining bins with logarithmic spacing prior to calculating correlations. In interpreting PECS data, it is often useful to utilize logarithmically-varying time bins, in order to visualize and analyze correlations occurring at widely-varying time scales.

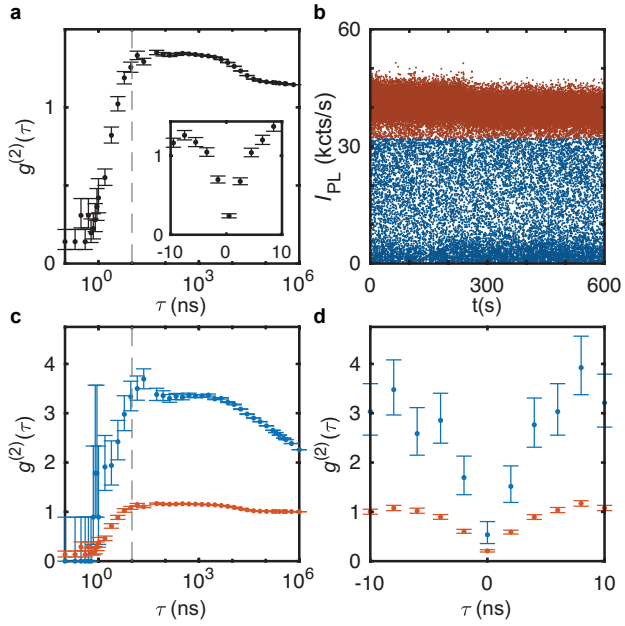

Figure 3.3: Output of time-tagged-time-resolved data processed for photon correlations shown for an example case of an emitter in h-BN with blinking. (a) Raw photon emission statistics data from an emitter in h-BN processed with logarithmic bins. Inset shows the same data processed on a linear scale. Dashed line denotes τ=10ns. (b) Intensity vs time data binned at 0.01s displaying partitioning at 32kcts/s between an on (orange) blinking state and off (blue) blinking state. (c) Photon emission statistics data from the same photon time series as (a) processed on a logarithmic scale based on intensity thresholding in (b). Bunching dynamics are mainly present in the photon emission statistics of the dark state (blue), whereas the data processed for the bright state (orange) adheres more closely to a two-level model. (d) Photon emission statistics data processed on a linear scale based on the intensity thresholding in (b).

We have incorporated the algorithm developed by Laurence *et al.* into a library of MATLAB functions for calculating and visualizing the autocorrelation function obtained from raw PECS data. In addition to $g^{(2)}(\tau)$, the library functions also calculate the time-averaged, steady-state intensity over the course of acquisition, which can be referenced to control for experimental factors such as fluctuations in emitter stability and setup drift. Blinking, in particular, is a common problem for quantum emitters. Blinking emitters stochastically switch between two or more brightness levels due to changes in their electronic state or fluctuations in their local environment. Our PECS analysis code allows for the data to be thresholded according to the time-averaged intensity, with the autocorrelation function calculated separately for different brightness levels. The specified threshold for the partitions is applied to the time-dependent intensity data as demonstrated in Fig. 3.3(b) where a threshold of 32kcts/s separates a bright state at ∼40kcts/s from a dark state at ∼3kcts/s. The correlations for each state can then be calculated separately resulting in two different autocorrelation traces shown in Fig. 3.3(c) on a logarithmic scale and Fig. 3.3(d) on a linear scale. This can enable detailed studies of optical dynamics even for stochastically blinking emitters. Setup drift can typically be reduced by implementing a tracking scheme that periodically adjusts the microscope alignment between successive autocorrelation measurements.

Our implementation of Laurence *et al.*'s algorithm also returns the statistical uncertainty of a PECS measurement. The algorithm iterates through photons in Channel A, calculating correlations to bins in Channel B. Uncertainty in PECS data are dominated by shot noise; hence, if the number of photons recorded in a given bin is M, the Poissonian uncertainty is $\sqrt{M}$. To calculate $g^{(2)}(\tau)$, each bin is normalized by its time-averaged, expected number of counts, $I_A I_B T w$, where I_A and I_B are the time-averaged count rates in each channel, T is the total acquisition time, and w is the bin width. Hence, the experimental uncertainty in $g^{(2)}(\tau)$ is

$$\Delta = \frac{\sqrt{M}}{I_{\mathrm{A}} I_{\mathrm{B}} w T}. \tag{3.30}$$

Eq.3.30 can be used to determine what acquisition times are necessary to achieve a desired uncertainty in $g^{(2)}(\tau)$ given an emitter's intensity. As an illustrative example, for the emitter in

Fig 3.4(a) with $I_A \approx I_B \approx 40$kcts/s and $w = 0.35ns$, the data was acquired for 600s in order to achieve $\Delta \approx 0.05$. For bins with close to zero counts, Poisson error (Eq. 3.30) gives inaccurate results [11]. As a result, upper and lower errors ($\Delta^{\pm}$) are calculated for each bin according to Poisson error with asymmetric errors,

$$\Delta^{\pm} = \frac{\sqrt{M + \frac{1}{4}} \pm \frac{1}{2}}{I_{\mathrm{A}} I_{\mathrm{B}} w T}. \tag{3.31}$$

Equation 3.31 reduces to Eq. 3.30 for large M.

For additional detail about the processing algorithm and a discussion of asymmetric errors, see Appendix A. A Python implementation of Laurence *et al.*'s algorithm can be found in Ref. [130].

3.3.3. Correcting for background signals

Once the correlations have been processed, the next step involves correcting the data for background. Background photons can arise from dark counts of the detection system, fluorescence of the host material, or other sources of room light. These background signals result in an inflated likelihood of observing uncorrelated light. As a result, background signals compress the $g^{(2)}(\tau)$ function toward 1, decreasing the extent of deviation above or below 1 at all delays.

The effect of a background signal with average intensity I_{bg} on $g^{(2)}(\tau)$ for an emitter of intensity I_{em} can be derived following a similar logic to the derivation of Eq. 3.26. This results in the background incorporated expression [27],

$$g^{(2)}_{\mathrm{meas}}(\tau) = 1 - \rho^2 + g^{(2)}(\tau)\rho^2, \tag{3.32}$$

where $\rho = \frac{I_{\mathrm{em}}}{I_{\mathrm{em}} + I_{\mathrm{bg}}}$. As a result, correcting for background only requires measuring ρ This can be achieved in various ways, including measuring I_{bg} at a point outside the diffraction-limited volume around the emitter, fitting the emitter's spatial profile to obtain I_{bg} and I_{em}, or fitting excitation-power-dependent photoluminescence intensity data using a known saturation function for the emitter and a linearly-scaling background component.

Figure 3.4(a) shows an example of raw $g^{(2)}(\tau)$ data acquired from an emitter in room-temperature, hexagonal boron nitride (h-BN) prior to any corrections. Figure 3.4(b) illustrates the process of

fitting an intensity line trace in order to measure ρ so that background correction can be performed. Transverse intensity line traces across x and y cross-sections (data for y cross-section are shown) of the emitter's 2D photoluminescence (PL) scan at the focal plane (inset) are fit using Gaussian functions, with the peak amplitude and offset of the fits giving the values for signal and background, respectively. The background is then corrected by solving Eq. 3.32 for $g^{(2)}(\tau)$. In Fig. 3.4(c), the orange data points and orange shaded fit show the resulting $g^{(2)}(\tau)$ data and fit following background subtraction.

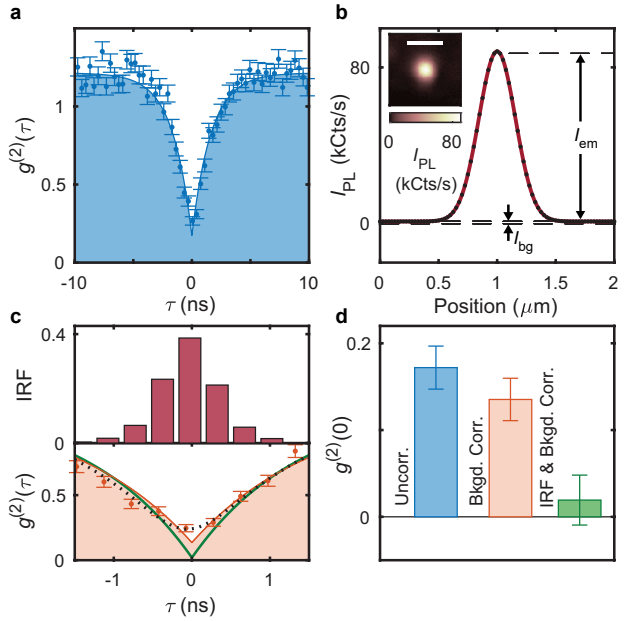

Figure 3.4: Background and timing jitter correction to verify single-photon emission in hexagonal boron nitride (h-BN). (a) Raw photon emission statistics data from an emitter in h-BN. (b) Transverse intensity trace across the y cross-section of the PL scan in inset taken at the focus plane. White scale bar in inset shows 1μm. Signal (I_{em}) and background (I_{bg}) are denoted by arrows and are extracted from fit. (c) (lower panel) Background-corrected data and fit (orange), and extracted $g^{(2)}(\tau)$ after background and timing-jitter correction (green). Convolution of the fully corrected data with the measured instrument response function (upper panel) gives the black dotted line. (d) The value of $g^{(2)}(0)$ from the fit before corrections (blue), after background correction only (orange), and after background and timing jitter correction (green). Uncertainties in $g^{(2)}(0)$ are 68% confidence intervals propagated from the corresponding best fits.

The emitter shown in Fig. 3.4 contributes 99% of the total signal, so background photons have a minimal effect on the shape of $g^{(2)}(\tau)$ and the value of $g^{(2)}(0)$ (see panels C and D). However, this is not always the case. In many situations, background photons can be a dominant source of

systematic error. This can be partially mitigated by adjusting acquisition time to account for the effect of background on error in $g^{(2)}(\tau)$, $\Delta_{bg} \approx \frac{\Delta}{\rho^2}$ [122]. In these cases, it can also be helpful to quantify the excitation power dependence of the emission rate. Since the emitter signal typically saturates with increased excitation power, whereas background signals scale linearly, one can select an excitation condition where the signal-to-background ratio is maximized. Most emitters are characterized by saturation functions that approximate the empirical form [22]

$$I(p) = \frac{I_{\text{sat}} p}{p_{\text{sat}} + p} + Bp, \tag{3.33}$$

where p is the excitation power, I_{sat} is the saturation intensity, p_{sat} is saturation power, and B is the prefactor for the contribution from the background. Often, acquiring photon emission statistics close to saturation power balances the desire for high ρ and sufficient signal to minimize shot noise. In a two-level system, saturation power corresponds to the situation when the excitation rate equals the emission rate, $\Gamma_{eg} = \Gamma_{ge}$. However, one must also consider the fact that antibunching and bunching timescales are generally a function of excitation power, as described in Section 3.2.

3.3.4. Correcting for timing jitter

Detector timing jitter, also known as the instrument response function (IRF), is the distribution of the electronic response time of the detector system to signal an event after photon arrival. Integrating the IRF over a time range gives the probability of the detector registering a photon event within that time window after the photon is received, The IRF of an ideal detector system is a delta function, but for a realistic experiment, the distribution will have a non-zero width. While timing jitter can arise from any electronics in the system that add arrival time uncertainty, the choice of detector typically has the largest contribution to the IRF [144]. Commonly-used single-photon avalanche diode detectors typically have IRF widths ranging from 100 ps to 1 ns.

The timing error manifests in the $g^{(2)}(\tau)$ trace as a convolution of the timing error distribution with the actual $g^{(2)}(\tau)$ signal from the emitter, *i.e.*,

$$g^{(2)}_{\text{meas}} = \text{IRF} * g^{(2)}. \tag{3.34}$$

The convolution changes the measured value of $g^{(2)}(0)$ and the shape of $g^{(2)}(\tau)$ at small delays comparable to the IRF width.

Correcting for the timing jitter requires measuring the IRF of the setup. The IRF can be obtained by collecting the distribution of detection times from a highly attenuated ($\sim$0.1 photons/pulse), pulsed laser source with a pulse width much less than the specified timing jitter of the detectors. When using two detectors to measure photon emission statistics, the IRF of both detectors can be acquired by measuring the autocorrelation from the pulsed source. This measurement will give a convolution of the two detectors' timing distributions and the shape of the pulsed source. However, when the optical pulse width is much less than the IRF width, it can be neglected. While some IRFs can be approximated as Gaussian, the shape of the IRF can vary depending on the detector, and the functional form may not always be obvious [129].

Once the IRF of the setup is measured, the $g^{(2)}(\tau)$ data can be compensated for its systematic effects. One method, deconvolution, involves solving Eq. 3.34 for $g^{(2)}(\tau)$. However, deconvolution amplifies noise and complicates propagation of experimental uncertainty. Therefore, it is often preferable to incorporate the measured IRF into a fitting function to be compared directly with the measured $g^{(2)}(\tau)$ data. This can be accomplished by including the numerical convolution of the measured IRF within the emprical fit function for $g^{(2)}(\tau)$. This method requires that the measured IRF and $g^{(2)}(\tau)$ be processed with the same, uniform, time bin width. The true timescales of the emitter and uncertainties can be extracted from the resulting best fit.

Figure 3.4(c) illustrates an example of IRF correction. The measured IRF data are shown in red (top) and are binned with a 350 ps bin width, as are the measured $g^{(2)}(\tau)$ data (orange, bottom), here shown after background correction but before IRF correction. The green line displays the IRF-corrected $g^{(2)}(\tau)$ empirical best fit. The black dotted curve, which is a convolution of the green line and IRF, aligns closely with the data and is used to determine best-fit parameters and uncertainties using a least-squares fitting method. Because the IRF and background corrections both reduce the value of $g^{(2)}(0)$, it is possible to extract a negative best-fit value. This is a consequence of experimental uncertainties which, if quantified properly, should be accounted for within the

confidence interval of $g^{(2)}(0)$.

3.3.5. Quantifying the effects of timing jitter

The extent of the IRF's effect on the shape of $g^{(2)}(\tau)$ hinges on how its standard deviation width, σ, compares to the internal timescales of the emitter. In the cases where $\sigma \gtrsim \tau_1$, where τ_1 denotes the shortest timescale to emit subsequent photons (typically, the antibunching timescale), the emitter's faster dynamics can be obscured by the timing jitter.

The combination of bunching and antibunching dynamics on different timescales can further complicate the effects of the detector IRF. Figure 3.5 illustrates an example of the effect of a Gaussian IRF with width σ on $g^{(2)}(\tau)$ of an emitter represented by a three-level (two-timescale) model:

$$g^{(2)}(\tau) = 1 - (1 + \beta_2)e^{\frac{-|\tau|}{\tau_1}} + \beta_2 e^{\frac{-|\tau|}{\tau_2}}, \tag{3.35}$$

with antibunching timescale τ_1, bunching timescale τ_2, and bunching amplitude β_2. The left-hand side of the figure depicts the value of $g^{(2)}(0)$ as a function of different parameters, and the right-hand side depicts the effect on the whole shape of $g^{(2)}(\tau)$ for select combinations. A dashed line shows the threshold for measuring $g^{(2)}(0) = 0.5$. The upper two panels examine the effect for different bunching amplitudes at a fixed ratio of $\frac{\tau_2}{\sigma} = 30$. Hence in these cases, the bunching timescale is much larger than the IRF width. Nonetheless, the higher the bunching amplitude, the greater effect the convolution of the IRF and $g^{(2)}(\tau)$ have on the measured $g^{(2)}(\tau)$ at low times, an effect which is amplified for low $\frac{\tau_1}{\sigma}$. The lower two panels examine the effect of the ratio $\frac{\tau_1}{\sigma}$ for fixed $\beta_2 = 1.5$. As $\tau_1 \to \sigma$ from above, the measured value of $g^{(2)}(0)$ increases and the width of the antibunching dip at short delays decreases. For systems with more than three levels, we would expect similar effects, with the IRF impacting measurements of $g^{(2)}(0)$ and the shortest timescale, τ_1, the most. These effects exemplify how IRF correction can play a critical role in extracting the actual value of $g^{(2)}(0)$ and confirming single-photon emission. An example of such a case is illustrated by the h-BN emitter in Fig. 3.4(d).

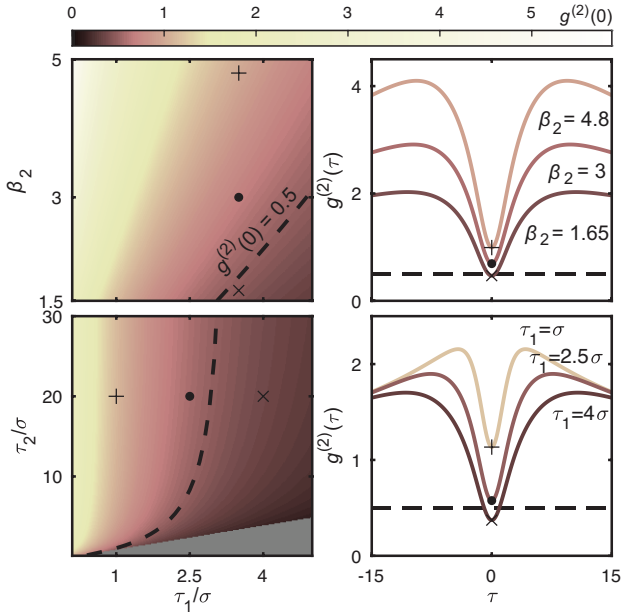

Figure 3.5: Effect of timing jitter on $g^{(2)}(0)$. (Left) The value of $g^{(2)}(0)$ is calculated as a function of the ratio of $\frac{\tau_1}{\sigma}$ and $\frac{\tau_2}{\sigma}$ or β_2 for a three-level system with timescales τ_1 and τ_2 and bunching amplitude β_2, and a gaussian IRF with standard deviation σ. (Right) Six points are selected from the parameter combinations on the left to illustrate how $g^{(2)}(\tau)$ at low delays changes for different ratios of $\frac{\tau_1}{\sigma}$ (bottom) and different values of β_2 (top).

3.4. Analysis

The ability to analyze PECS data in order to infer an emitter's internal dynamics requires an understanding of how stochastic evolution through radiative and non-radiative states in an electronic model leads to features in $g^{(2)}(\tau)$.

The rate equation governing the population dynamics, Eq. 3.17, is a first-order, linear ODE, with general solutions of the form

$$\vec{P}(t) = A_0\vec{v}_0 + \sum_{i=1}^{n-1} A_i e^{\lambda_i t}\vec{v}_i. \tag{3.36}$$

Here, λ_i are the eigenvalue rates, v_i are the eigenvectors, and A_i are constants determined by the initial condition. For an n-level system with a single excited state, the excited state probability is

$$P_e(t) = A_0(\vec{v}_0 \cdot \hat{e}) + \sum_{i=1}^{n-1} A_i(\vec{v}_i \cdot \hat{e})e^{\lambda_i t}. \tag{3.37}$$

The probability-conserving condition of $\Sigma_j G_{ij} = 0$ means that there will always be a zero eigenvalue, λ_0, and null eigenvector, v_0, corresponding to the solution of the steady-state equation,

$$0 = GP. \tag{3.38}$$

The non-zero eigenvalues λ_i can be real or complex, depending on the properties of G. If complex eigenvalues do appear, they occur in conjugate pairs due to the real, non-negative transition rates. In this way, the general solution remains real. In all cases, the real part of any non-zero eigenvalues will be negative [139]. Therefore, from the eigenvalues, we can define a set of timescales governing different processes, $\tau_i = -\frac{1}{\mathrm{Re}(\lambda_i)}$ where $\tau_i > 0$. Given an initial condition corresponding to the system configuration following the detection of a photon, we can follow Eq. 3.5 to obtain a general form of the autocorrelation function. Normalizing Eq. 3.37 to the steady state, with the assumption of no background such that any detected photon projects the system into the ground state, this

results in the following general empirical formula:

$$g^{(2)}(\tau) = 1 + \sum_{i=1}^{n-1} \beta_i e^{-\frac{\tau}{\tau_i}}, \tag{3.39}$$

where $\beta_i = \frac{A_i(\vec{v}_i \cdot \hat{e})}{P_e^{\infty}}$ are constants, $P_e^{\infty} = A_0(\vec{v}_0 \cdot \hat{e})$ is the steady-state excited state population, and n is the number of states. Equation 3.39 defines a curve that starts at 0 for $\tau = 0$ and decays to $g^{(2)} \to 1$ as $\tau \to \infty$.

Antibunching arises when emission of consecutive photons is delayed as the excited state is re-populated, leading to a decreased likelihood of photons separated by short times. Empirically, it is captured by terms in Eq. 3.39 with negative prefactors. In the case of a two-level model, antibunching occurs on the timescale of $\tau_1 = \frac{1}{\Gamma_{ge}+\Gamma_{eg}}$, representing the time to evolve from the ground state to the excited state and back to the ground state again. Bunching dynamics, on the other hand, arise from transitions to non-radiative states, which delay the emission of a photon, such as transitions between charge or spin manifolds. Such processes can result in the emitter's excited state population(s) evolving non-monotonically toward the steady state, leading to bunching in the autocorrelation trace. Note that while bunching shows an increase in correlations relative to the steady-state, it results from a decrease in overall emission. When multiple non-radiative states participate in the dynamics, with different lifetimes, the autocorrelation function features multiple, resolvable bunching timescales. In some situations, multiple radiative excited states can lead to multiple antibunching terms and complex eigenvalues associated with the antibunching dynamics [103]. However, such situations are uncommon and multiple antibunching rates are typically difficult to resolve experimentally. Therefore, it is typically appropriate to assume a single antibunching timescale, with a corresponding empirical model,

$$g^{(2)}(\tau) = 1 - \beta_1 e^{-\frac{\tau}{\tau_1}} + \sum_{i=2}^{n-1} \beta_i e^{-\frac{\tau}{\tau_i}}, \tag{3.40}$$

where all the β_i are positive. Given PECS data from an emitter with unknown level structure and dynamics, the set of models for varied n can be fit to the data, and a statistical comparison based on

the Akaiki Information Criterion, Poisson likelihood, or the chi-squared statistic can determine the most appropriate model to describe the data. A determination of n in this way places a lower limit on the number of electronic levels involved in the dynamics. Additional details on fit comparisons using the Akaike Information Criterion can be found in Appendix B. Additional discussion of Poisson likelihood in counting experiments can be found in Refs. [60] and [36]. Potential electronic models can be further narrowed down by measuring $g^{(2)}(\tau)$ at different powers and fields and comparing with simulations, as we describe in the next subsection.

3.4.1. Simulating photon emission statistics

Simulations of $g^{(2)}(\tau)$ provide a means to test potential models that explain features observed in experimental data. The time-dependent state populations of a given model, consisting of n states with transition rates designated by the $n \times n$ matrix, G, are governed by the rate equation, Eq. 3.17. In principle, the system of equations can be solved analytically according to Eq. 3.36. In practice, the dynamics can be efficiently simulated using a numerical ODE solver.

For a simulation of $g^{(2)}(\tau)$, the initial conditions are the state of the system immediately following the detection of a photon. In a model with a single, radiative transition from excited $|e\rangle$ to ground state $|g\rangle$, and assuming background photons can be neglected (this is the case if the experimental $g^{(2)}(\tau)$ have been background-corrected), the initial condition is simply $P_g(0) = 1$, with all other state populations equal to zero at time $t = 0$. The numerical solution of Eq. 3.17 yields the time-dependent state populations, $P(t)$. The steady-state populations, P^{∞} can also be found by numerically solving Eq. 3.38. Once the time-dependent and steady-state populations are found, quantities such as the PL intensity,

$$I_{\mathrm{PL}} = G_{ge} P_e, \tag{3.41}$$

and $g^{(2)}(\tau)$ (Eq. 3.5) can then be calculated. The simulation can also be adapted to account for models involving multiple radiative transitions. Details on the simulations in such cases can be found in Appendix C.0.2.

This simulation tool can be linked with various physical models to compare simulations across

changing experimental parameters such as excitation power and fields. Power-dependence can be modeled by running multiple simulations at different excitation powers in which any changes to transition rates that are dependent on excitation power are incorporated into the transition rate matrix for each simulation. For example, a pumped transition from a ground to excited state might have a linear dependence on a power parameter and can be defined to be adjusted accordingly as the power changes. In a similar manner, electric or magnetic-field dependence of photon-statistics can be simulated by defining transitions that are a function of a field parameter. For example, spin-dependent transition rates could change as a function of external magnetic field due to the system's spin Hamiltonian.

Figure 3.6 shows examples of simulated autocorrelation traces for four different models with varying excitation powers and magnetic fields. The transition rates for each model were chosen so that the black curves in Figs. 3.6(a-c) are qualitatively the same as each other and similar to the black curve in the more complex model of Fig. 3.6(d). However, the simulated $g^{(2)}$ curves for the models in Figs. 3.6(a-c) vary in qualitatively distinct ways as a function of excitation power and magnetic field. Thus, in comparison with experimental PECS data, these simulations can be varied to help narrow down potential models.

Figure 3.6(a) depicts a basic three-level system, the simplest model that can host both antibunching and bunching dynamics. The single radiative transition is denoted by the wiggly arrow. A single power-dependent transition, designated by the solid red arrow, is varied in order to simulate $g^{(2)}(\tau)$ for high (red), medium (black) and low (yellow) excitation powers.

Figure 3.6(b) shows a three-level model similar to that in Fig. 3.6(a), but in this case the transitions to and from the metastable third state also depend on the excitation power. This will be the case, for example, if the metastable state represents a different charge configuration than the ground and radiative excited state, which can be accessed through optically pumped ionization and recombination transitions. Varying the excitation power differentiates between the models in Figs. 3.6(a) and 3.6(b), as the bunching timescale τ_2 changes dramatically as a function of power in 3.6(b), in comparison to Fig. 3.6(a) where the dominant power-dependent change is the bunching

Table 3.1: **Simulation parameters for Fig 3.6**

Parameter	**3-level model (spontaneous transitions)**	**3-level model (pumped transitions)**	**5-level model**	**Nitrogen-Vacancy model**
k_{ex} (MHz)	[25,50,100]	[25,50,100]	[25,50,100]	[13.125,26.25,52.5]
k_{r} (MHz)	50	50	50	75
k_{isc0} (MHz)	5	$5k_{\mathrm{ex}}$	4.9995	5
$k_{\mathrm{isc0,out}}$ (MHz)	2.5	$2.5k_{\mathrm{ex}}$	2.5	3.11
$k_{\mathrm{isc}\pm}$ (MHz)	-	-	2.5E-4	60
$k_{\mathrm{isc,out}\pm}$ (MHz)	-	-	.025	2.75
$k_{\mathrm{ion}}/k_{\mathrm{rec}}$	-	-	-	$3k_{\mathrm{ex}}/2.25k_{\mathrm{ex}}$
B amplitude (G)	-	-	46	300
B angle (deg)	-	-	[0,30,60]	[0,15,50]

amplitude. Experimental observations of $g^{(2)}(\tau)$ as a function of excitation power can be compared with such models to determine the nature of the non-radiative transitions and extract their scaling with optical excitation power.

In Fig. 3.6(c), spin dependent transitions are introduced to the model, represented by the blue arrow. Here, varying a magnetic field angle that mixes the spin eigenstates of the metastable state can differentiate between the models in (a) and (c), whose traces exhibit similar power-dependent behavior. The magnetic-field-dependent bunching dynamics (shown in blue) arise from the spin-dependent transitions in (c). These spin-dependent transitions can sometimes be exploited to optically initialize and measure the spin state. Hence, PECS measurements showing a variation in response to external magnetic fields can indicate the presence of optically addressable spin states.

As more is known about a system and its dynamics, PECS simulations can be extended to quite complex situations. Figure 3.6(d), depicts a nine-level simulation of a nitrogen-vacancy center, including both optically-driven ionization and recombination transitions as well as magnetic-field-dependent spin transitions.

Simulation parameters used to generate Fig. 3.6 can be found in Table 3.1. Here, the excitation rate is given by k_{ex}, the emission rate is given by k_{r}, and the rates to and from the the inter-system crossing (isc) metastable state are k_{isc0} and $k_{\mathrm{isc0,out}}$ respectively. For models with spin states in the

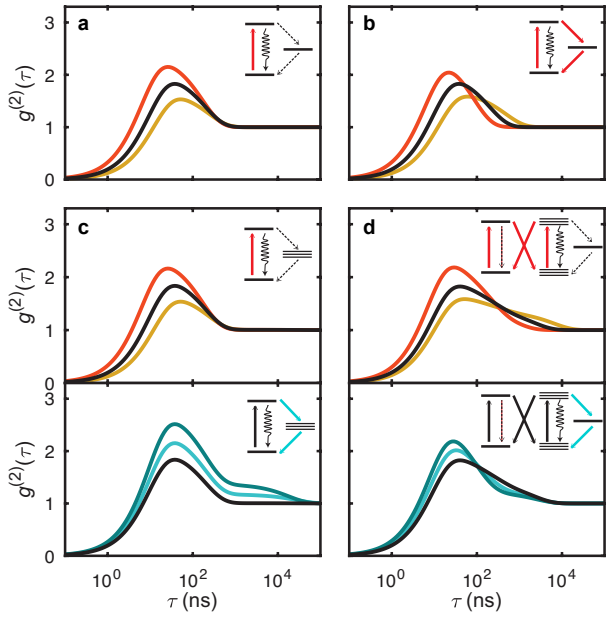

Figure 3.6: Simulated $g^{(2)}$ traces for four different physical models. The effects of increasing (red) or decreasing (yellow) excitation power and a lower (light blue) or higher (dark blue) angle of magnetic field on $g^{(2)}(\tau)$ vary depending on the model. (a) Three-level model with a pumped transition (solid red arrow) to the excited state and fixed, non-radiative transition rates (dashed arrows) to a metastable state. (b) Three-level model with power-dependent transitions (solid red arrows) to and from a metastable state. (c) 5-level model with a pumped transition to the singlet excited state, and spin-dependent transitions (blue arrow) to and from a metastable spin triplet. (d) 9-level model of a nitrogen-vacancy center with both spin-dependent and power-dependent transitions. Radiative transitions are shown as wiggly arrows. Subpanels in (c) and (d) show the effects of changing power (top subpanel) and magnetic field angle (bottom subpanel) separately for each model. Yellow, black, and red curves in (a-c) depict excitation pump rates respectively half, equal to, and double each model's radiative decay rate. Magnetic field parameters were chosen in order to qualitatively represent different degrees of spin mixing with black, light blue, and dark blue curves corresponding to zero, medium, and high spin mixing respectively. Black curves are identical between top and bottom subpanels, and parameters are chosen such that the black curves for each model are qualitatively the same between (a-c) and approximate the amplitude and peak position of (d). More detail on the simulation parameters can be found in Table 3.1.

metastable state, such as the 5-level model and NV model, k_{isc0} ($k_{\text{isc0,out}}$) specifies the zero-B-field transition rate to (from) the $m_S = 0$ spin-triplet sublevel, while $k_{\text{isc}\pm}$ ($k_{\text{isc,out}\pm}$) specifies the zero-B-field transition rate to (from) the $m_S = \pm 1$ spin sublevels. k_{ion} and k_{rec} are the ionization and recombination rates to and from NV^0 and NV^-. The B-field angle is given with respect to the defect axis. Power-dependent transitions are shown as a multiple of k_{ex}. For models with spin-dependence (5-level and NV), the Hamiltonian specified is for the case of a spin-1 triplet configuration with a single symmetry axis and takes the form,

$$H = g\mu_B \mathbf{B} \cdot \mathbf{S} + D(S_z^2 - \frac{1}{3}S(S+1)), \tag{3.42}$$

where g is the isotropic g-factor, μ_B is the Bohr magneton, $\mathbf{B}$ is the magnetic-field vector, D is the zero-field splitting, and $\mathbf{S}$ and S_z are spin-1 operators. For the 5-level model simulation, we assume $D = 1000$ MHz for the spin-triplet metastable state. For the NV center, the values used were $g_{\text{ES}} = 2.01$, $g_{\text{GS}} = 2.0028$, $D_{ES} = 1425$ MHz, and $D_{GS} = 2859$ MHz, where "ES" and "GS" refer to the excited and ground state respectively. When a magnetic field is applied to a model with spin states, the interaction between the spin states and the field, as defined by the Hamiltonian, results in spin mixing. In the NV model, the inner product of the excited state and ground state eigenvectors adjusts the baseline excitation (k_{ex}) and emission (k_r) rates to give the distribution of excitation and emission rates between the ground and excited spin states. Similarly, for both the NV and 5-level model, other spin-dependent transition rates such as the inter-system crossing rates (k_{isc}) specified in Table 3.1 are adjusted according to the new calculated spin projections in a magnetic field.

Transition rate matrices for each black curve in Fig. 3.6(a-d) are respectively as follows:

$$\begin{bmatrix} -50 & 50 & 2.5 \\ 50 & -55 & 0 \\ 0 & 5 & -2.5 \end{bmatrix} \tag{3.43a}$$

$$\begin{bmatrix} -50 & 50 & 2.5 \\ 50 & -55 & 0 \\ 0 & 5 & -2.5 \end{bmatrix} \tag{3.43b}$$

$$\begin{bmatrix} -50 & 50 & 2.5 & 0.025 & 0.025 \\ 50 & -55 & 0 & 0 & 0 \\ 0 & 4.9995 & -2.5 & 0 & 0 \\ 0 & 0.00025 & 0 & -0.025 & 0 \\ 0 & 0.00025 & 0 & 0 & -0.025 \end{bmatrix} \tag{3.43c}$$

$$\begin{bmatrix} -26.252 & 0.001 & .001 & 75 & 0 & 0 & 3.1087 & 0 & 0.0058 \\ 0.001 & -26.262 & 0.001 & 0 & 75 & 0 & 1.1957 & 0 & 0.0058 \\ 0.001 & 0.001 & -26.252 & 0 & 0 & 75 & 1.957 & 0 & 0.0058 \\ 26.25 & 0 & 0 & -80.0175 & 0 & 0 & 0 & 0 & 0 \\ 0 & 26.25 & 0 & 0 & -135.0175 & 0 & 0 & 0 & 0 \\ 0 & 0 & 26.25 & 0 & 0 & -135.0175 & 0 & 0 & 0 \\ 0 & 0 & 0 & 5 & 60 & 60 & -5.5 & 0 & 0 \\ 0 & 0 & 0 & 0.0175 & 0.0175 & 0.0175 & 0 & -78.75 & 49.9825 \\ 0 & 0 & 0 & 0 & 0 & 0 & 0 & 78.75 & -50 \end{bmatrix} \tag{3.43d}$$

3.5. Conclusion

PECS can be a highly informative measurement that yields valuable information about a system's optical dynamics. Understanding the various factors that come into play regarding experimental and analytical considerations can inform interpretation of results. While the in-depth, pedagogical exploration of PECS through this chapter provides a guide to the use of PECS, examples of experiments where this technique is applied can provide additional insight into the practical application

PECS.

The next two chapters will demonstrate the application of PECS to two quantum defect systems: The nitrogen-vacancy (NV) center in diamond and a quantum emitter in hexagonal boron nitride (h-BN). These case-studies will illustrate the practical considerations that come into play when analyzing different systems and the versatility of PECS for these purposes. The electronic structure and optical dynamics of the NV center are generally known. Therefore, the application of PECS to this system will involve a focus on the particular features that correspond to the charge and spin dynamics and fine-tuning the transition paths and rates from a baseline NV model. On the other hand, h-BN quantum emitters are heterogeneous in their optical properties [47] and as a more recent system their optical dynamics are less established. Therefore, for the h-BN emitter, we construct a model for its electronic structure and optical dynamics from scratch. This requires the use of PECS in conjunction with other time-domain measurements to parse the contributions of individual transitions to the observed PECS dynamics and to hypthesize various features of the electronic model.

CHAPTER 4

OPTICAL DYNAMICS OF A NITROGEN-VACANCY CENTER

4.1. Introduction

The nitrogen-vacancy (NV) center in diamond is a robust platform for quantum technologies, particularly in the areas of quantum sensing, quantum communication, and quantum networks. The NV center's photostability, sensitivity to magnetic fields, and spin-dependent PL at room temperature enable mapping of local magnetic and electric fields and temperatures [118]. Additionally, hybrid schemes involving surface engineering can facilitate sensing of chemical quantities such as pH [110, 118]. The ability to incorporate NV centers in nanodiamonds into living cells [91] and recent demonstrations of in vitro biosensing [94] make the NV center a promising platform for numerous biosensing applications [152]. The NV center also facilitates applications in quantum networks and quantum communication [35]. Demonstrations of entanglement of two spatially-separated NV centers [62, 20] and controlled coupling to local Carbon-13 nuclear spins [1, 134] form the basis for proposals of quantum networks consisting of local NV registers coupled to spatially separated nodes [114].

The implementation of NV-center-based quantum protocols requires detailed knowledge of the system's electronic structure and optical dynamics. In particular, the presence of spin-dependent transition rates enables spin-state initialization through optical pumping. The differentiated transition rates also result in spin-state-dependent photoluminescence (PL), enabling a mechanism for spin readout [111, 142, 42]. Understanding the dynamics between the NV center charge states can lead to the design of schemes that improve upon spin readout [65, 121]. Therefore, detailed exploration of the structure and dynamics underlying important spin initialization and readout mechanisms is necessary.

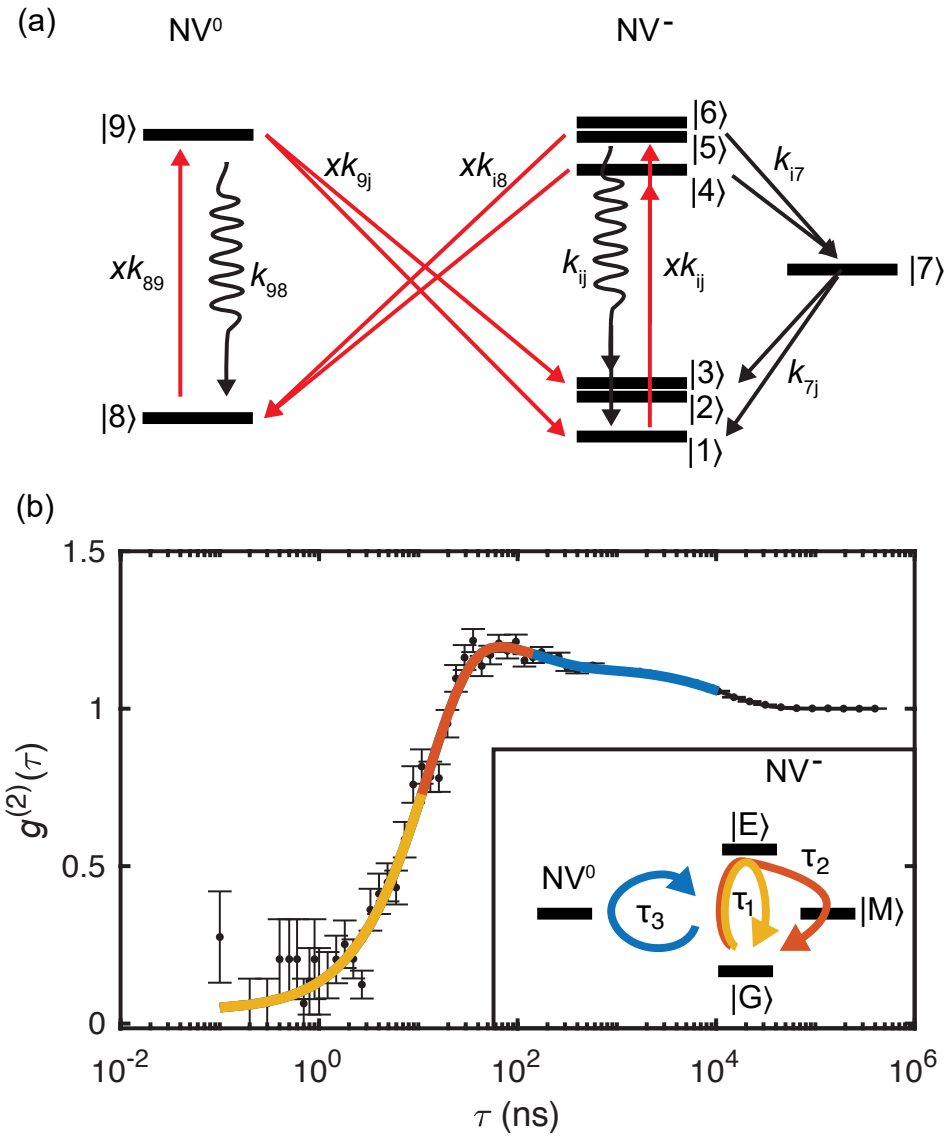

Figure 4.1: **Optical dynamics of an NV center. (a)** A model of the electronic structure and optical dynamics of an NV center. Red arrows indicate excitation-power-dependent transitions, black straight arrows indicate non-radiative transitions, and squiggly arrows denote radiative transitions. Rates k_{ij} indicate transition rates from state i to state j and x scales all the power-dependent rates with excitation power. **(b)** Example analyzed PECS data acquired from an NV center at 50 µW excitation power and no applied magnetic field. Qualitative features arising from different timescale processes are shown as different colors. Inset shows a simplified model of the NV center. Processes contributing to qualitative features in **(b)** are shown with corresponding colors.

4.2. Background

4.2.1. Electronic structure

The electronic structure of the NV center has been mapped out through numerous experimental and theoretical studies [154, 42, 109]. Figure 4.1(a) shows a basic model of the NV center electronic structure. The NV center typically exists in one of two charge configurations: the neutral configuration, NV^0, or the negatively-charged configuration, NV^-. The electronic structure of the NV^- is composed of a ground and excited state S=1 spin triplet with spin sublevels $m_s = 0$, $m_s = +1$, and $m_s = -1$ Transitions between the ground and excited state spin sublevels are generally spin-conserving and the transition from the excited to ground state is radiative with a 637 nm ZPL [42]. A non-radiative decay pathway also exists through an intersystem crossing to a metastable singlet state. While the metastable state is known to be composed of two states with an infrared radiative transition between them, the lifetime of the higher-energy state is so short (100 ps at 78 K [141]) that, here, we treat both states as a single metastable state.

Due to the spin-dependent fluorescence of NV^- and the ability to control its spin states, the NV^- spin states $m_s = \pm 1$ and $m_s = 0$ typically are chosen as the two basis states of the NV qubit. Therefore, particular focus has been directed toward the NV^- charge configuration. However, the NV center fluctuates between two common charge states, the negatively charged NV^- and the neutral NV^0. Therefore, it is also important to understand the structure and dynamics of the NV^0 charge state [13, 9]. The electronic structure of the NV^0 consists of a ground and excited doublet with a radiative decay with 575 nm ZPL [42]. Similarly to the NV^-, there is also a non-radiative decay path from the exicted state through a metastable state. However, since our optics thresholds filter out most photons from the radiative NV^0 transition, here, we simplify the NV^0 by just modelling the excited and ground state.

4.2.2. Optical dynamics

The transition rates that govern the dynamics of the NV center can be determined through a variety of experimental methods that measure state lifetimes and branching ratios. At zero magnetic field and room temperature, the $m + s = \pm 1$ ground and excited states are only separated by a small,

hyperfine splitting. Therefore, the transition rates from and to the $m_s = \pm 1$ states can be treated as equal in this condition. The introduction of an external magnetic field leads to a splitting of the $m_s = \pm 1$ states. The subsequent dynamics in response to a magnetic field are governed by the spin interactions in the excited-state and ground-state Hamiltonians. The Hamiltonian is given by,

$$H = g\mu_B \mathbf{B} \cdot \mathbf{S} + D(S_z^2 - \frac{1}{3}S(S+1)), \tag{4.1}$$

where g is the isotropic g-factor, μ_B is the Bohr magneton, $\mathbf{B}$ is the magnetic-field vector, D is the zero-field splitting, and $\mathbf{S}$ and S_z are spin-1 operators. Measurements of ODMR for both the ground and excited states give estimates for g and D in each case.

Figure 4.1(b) shows an example of how timescales that are present in PECS measurements arise from the timescales of various processes in the NV center. Three timescales, τ_1, τ_2, and τ_3 extracted from a fit to the $g^{(2)}(\tau)$ curve are shown in yellow, red, and blue respectively. In this case, the contribution of each to $g^{(2)}(\tau)$ is also qualitatively resolvable as different visible features. The inset displays a simplified model of the NV center. This model assumes that the majority of photons emitted by the NV^0 manifold are not collected due to collection filters and thus the radiative dynamics originate from the NV^-. As a result, here the dynamics of the NV^0 are collapsed into one level. Similarly, the three spin sub levels are collapsed into the excited and ground states. In this simplified model, there are three processes that have their own distinct timescales. The first and fastest is the process of excitation from the NV^- ground state to the excited state then decay back to the ground state through the radiative decay transition. This process is associated with τ_1 which is referred to as the antibunching timescale because of it corresponds to a dip in the $g^{(2)}(\tau)$ curve. The other two processes involve excitation from the NV^- ground to excited state with non-radiative decays back to the ground state. These are referred to as bunching processes because they delay the emission of a photon, resulting in values in the $g^{(2)}(\tau)$ curve that rise above 1. The first bunching process is the excitation and non-radiative decay through the metastable state. Here, this process is associated with timescale τ_2 and is referred to as the spin dynamics, as it is dependent on the spin-dependent decay rates from the excited state spin sublevels to the metastable state. The second bunching

process is the ionization and recombination of the NV center between the negative and neutral charge manifolds. Here, this process is associated with timescale τ_3 and is referred to as charge dynamics as it involves the dynamics of switching between the two charge states.

Beyond this simplified NV model, there exists additional complexity including different spin dependent decays through the metastable state and additional NV^0 dynamics. The three timescales discussed here are the dominant processes that can be distinguished from fits to PECS measurements of a room temperature NV center. However, PECS analysis can be informed by additional measurements of lifetimes and branching ratios to clarify more complex dynamics.

Further insight into the dynamics of spin-dependent and power-dependent rates can be gained through measurements of PECS as a function of different magnetic fields and powers [51]. In the NV center, applying an off-axis magnetic field leads to spin mixing, which affects the transition rates both to and from the ISC [136]. B-field-dependent PECS measurements help probe and quantify these spin dynamics. Applying different excitation powers affects any transition process that is power-dependent. In the model pictured in Fig. 4.1, the pump rates from the NV^- and NV^0 ground to excited states and the ionization and recombination rates to and from the different charge states are processes driven by the excitation power. Therefore, measurements as a function of power can give insight into the dynamics of ionization and recombination across powers.

4.3. Methods

4.3.1. Experimental setup

The sample consists of electronics grade type-IIa synthetic diamond (Element Six) that has been irradiated with 2-MeV electrons ($10^{14} cm^{-}2$) and annealed for 1 hour in forming gas. A solid immersion lens fabricated on the surface of the diamond helps couple out light emitted from the NV.

The setup is a home-built confocal microscope with a cw 532 nm excitation source (Gem 532, Laser Quantum). A $4f$ configuration directs the excitation beam onto the back of an objective (Olympus, MPLAN 100x) where a fast steering mirror (FSM, Optics in Motion) facilitates positioning of the

beam on the sample. The sample is mounted vertically on a three-axis stage (MAX300, Thorlabs) with a piezo stage for fine focus positioning. Photoluminescence (PL) excited from the NV center is filtered from the excitation with a 662 nm cutoff dichroic filter (Semrock). A fiber-splitter (Thorlabs) is used to direct the collected emission into two avalanche photo diode detectors (Excelitas and Laser Components). Due to the fiber splitter, afterflashes emitted by a detector upon receiving a photon can travel down the fiber splitter and be detected by the other detector, leading to anomalous correlations in the PECS signal. In order to filter out afterflashes, an 800nm SWP filter is introduced into the collection path between one of the legs of the fiber splitter and the detector. Due to the filter and dichroic, an estimated 70% of the NV^- spectrum and 10% of the NV^0 spectrum are collected. Photon arrival times are time-tagged for PECS measurments with a time-correlated single-photon counter (Pico Harp 300, PicoQuant).

Excitation power is adjusted through a continuously-variable neutral density wheel (NDC Thorlabs) and is calibrated just before the objective. The magnetic field is applied through a manually-adjustable goniometer that consists of an N52 neodymium magnet mounted at sample height on a pivot located below the sample. Magnetic field position and angle is manually-adjusted and confirmed through ESR measurements.

Figure 4.2(a) shows a schematic of part of the confocal setup. The excitation path is shown in green and the dichroic separating the excitation from the emitted PL (red path) is shown as a 45^o black line. The afterflash filter is pictured as a black rectangle on one of the paths of the fiber splitter. Dashed lines represent magnet positions with respect to the NV optical dipole (shown as a red arrow).

A microwave-generated-magnetic field for ESR measurements is applied through a lithographically-defined loop antenna on the surface of the diamond sample. Microwaves are generated by a continuous-wave signal generator (SG384, Stanford Research Systems) and are amplified (ZHL-16W-43-S+, Mini-Circuits) and amplitude-modulated (ZASWA-2-50DR, Mini-Circuits).

4.3.2. Experimental overview

The experiment consists of electron spin resonance (ESR), saturation, and PECS measurements taken at each of eight magnetic field conditions. Due to the the NV Hamiltonian (Eq. 4.1), we expect spin-mixing and the corresponding effect on the system's dynamics to occur due to the component of an applied magnetic field that is perpendicular to the NV-center optical dipole [46]. Therefore, the magnetic field conditions we select are a zero-field condition and seven applied field conditions where the field parallel to the NV dipole is kept constant at 115 ± 2 G and the perpendicular component of the field is varied in roughly 25 G increments ranging from 0-148 G perpendicular field. This requires the variation of both the angle and magnitude of the applied field for each condition. The magnet positions corresponding to the seven perpendicular field strengths are depicted in the schematic in Fig. 4.2(a).

In order to determine the steady-state PL response to excitation power, a saturation measurement is taken at each field condition. To measure saturation, the excitation power is varied from 10 µW to 11 mW. At each power, a focus scan is performed, identifying and selecting the sample distance from the objective that produces the maximum PL. Steady-state PL at each power is acquired from a 2D PL scan taken at the focal plane. The maximum PL is extracted from Gaussian fits to the transverse cross sections of the PL scan.

At each magnetic field condition, ESR is measured to confirm that the magnet placement gives the desired field strength and angle. Each ESR measurement consists of a microwave frequency sweep in which PL is averaged over a 0.5 s dwell time at each microwave frequency. Three sweeps are collected between which a focus scan and 2D PL tracking scan is taken to combat setup drift and remain centered on the NV.

PECS is measured at 11 excitation powers ranging from 50 µW to 6 mW for each magnetic field condition. The total PECS acquisition time for each power is selected based on the measured steady-state PL at that power, using Eq. 3.30 to target $g^{(2)}$ error of approximately $\Delta = \pm 0.05$ for a 1 ns bin. PECS measurements are paused at 2 minute increments to allow for a focus and tracking

scan to recenter the NV.

4.4. Analysis

PECS measurements yield a stream of photon arrival times that have been time-tagged by the TCSPC for each detector. The photon arrival times are processed using an algorithm based on *Laurence et al.* that calculates the normalized time correlations and Poisson errors across the two detectors [83] . More detail on the algorithm can be found in Appendix A. Once the photon arrival times are processed, the photon correlations are background corrected. This is done by measuring the background PL, which is acquired from the average y-offset of Gaussian fits to two transverse cross sections of a 2D PL scan. It is then possible to calculate ρ, the fraction of the total signal (PL intensity of the emitter and background) that is due to the emitter alone. The background incorporated expression [27],

$$g^{(2)}_{\text{meas}}(\tau) = 1 - \rho^2 + g^{(2)}(\tau)\rho^2, \tag{4.2}$$

can then be solved for $g^{(2)}(\tau)$ to give the background corrected data.

The background-corrected data is then fit to the empirical model,

$$g^{(2)}(\tau) = 1 - \beta_1 e^{-\frac{\tau}{\tau_1}} + \sum_{i=2}^{n} \beta_i e^{-\frac{\tau}{\tau_i}}, \tag{4.3}$$

where n is the number of timescales a fit can resolve from the $g^{(2)}(\tau)$ measurement. Each individual timescale, $i = 1 - n$ represents a process that is associated with a particular time τ_i and bunching amplitude, β_i. Each $g^{(2)}(\tau)$ dataset is fit to Eq. 4.3 for $n = 2$, 3, and 4 and statistical measures of fit, the AIC and reduced-chi-squared (χ^2_r), are calculated for each n to determine which model provides the best fit. While the four-timescale fit frequently gives a χ^2_r closest to 1, the AIC analysis indicates that two- or three- timescales models are the most likely to best describe the data. Broadly, the AIC analysis indicates that $g^{(2)}(\tau)$ acquired at < 1 mW excitation power is best described by a three-timescale fit, while $g^{(2)}(\tau)$ acquired at > 1 mW excitation power is best described by a two-timescale fit. In Fig. 4.1(b) an example of analyzed PECS data fit to a 3-timescale model is shown. The best fit gives values of $\tau_1 = 12.5 \pm 0.9$ ns, $\tau_2 = 160 \pm 50$ ns, and $\tau_3 = 12.3 \pm 0.6$ µs, which are

marked on the $g^{(2)}(\tau)$ curve as yellow, red, and blue lines respectively.

ESR data is normalized by the steady-state PL in the absence of microwaves. The data is analyzed by averaging the normalized PL at each microwave frequency over the three sweeps. Error is calculated as the standard error,

$$\frac{\sigma}{\sqrt{s-1}}, \tag{4.4}$$

where σ is the standard deviation and $s = 3$ is the number of sweeps. The data is fit to a double Gaussian and the two peak positions from the Gaussian fit give the location of the resonances. The resonances are used to calculate the magnitude (B) and angle (θ) of the magnetic field according to the following formulae:

$$B = \frac{\sqrt{r_1^2 + r_2^2 - r_1 r_2 - D^2}}{\sqrt{3}\gamma} \tag{4.5}$$

$$\cos^2(\theta) = \frac{(r_1 + r_2)[2(r_1^2 + r_2^2) - 5r_1 r_2] + 9D(B\gamma)^2 + 2D^3}{27D(B\gamma)^2}, \tag{4.6}$$

where r_1 and r_2 are the resonances, D is the zero-field splitting of the ground state, and γ is the electron gyromagnetic ratio [126]. Saturation measurements are analyzed at each field condition by averaging the acquired PL at each power over the three sweeps. Error is calculated as the standard error (Eq. 4.4).

At each magnetic field condition, changing the B-field magnitude and angle shifts the setup alignment, resulting in a corresponding change in setup excitation and collection efficiency. Therefore, in order to compare measurements across different magnetic field conditions, it is necessary to quantify this difference and apply a correction to the excitation powers at each B-field. PECS measurements provide a useful method for determining the effect on the collection efficiency, as the internal radiative decay rates and the excitation cross sections should remain constant while the overall excitation rates change with the power and setup alignment. These radiative dynamics are quantified in the antibunching timescale, τ_1, which is shown in Fig. 4.1(b) inset as a yellow arrow. This timescale can be approximated as $\tau_1^{-1} = k_{\mathrm{EG}} + k_{\mathrm{GE}}$ where k_{EG} is the radiative decay rate from the excited to ground state and k_{GE} is the excitation rate from the ground to excited

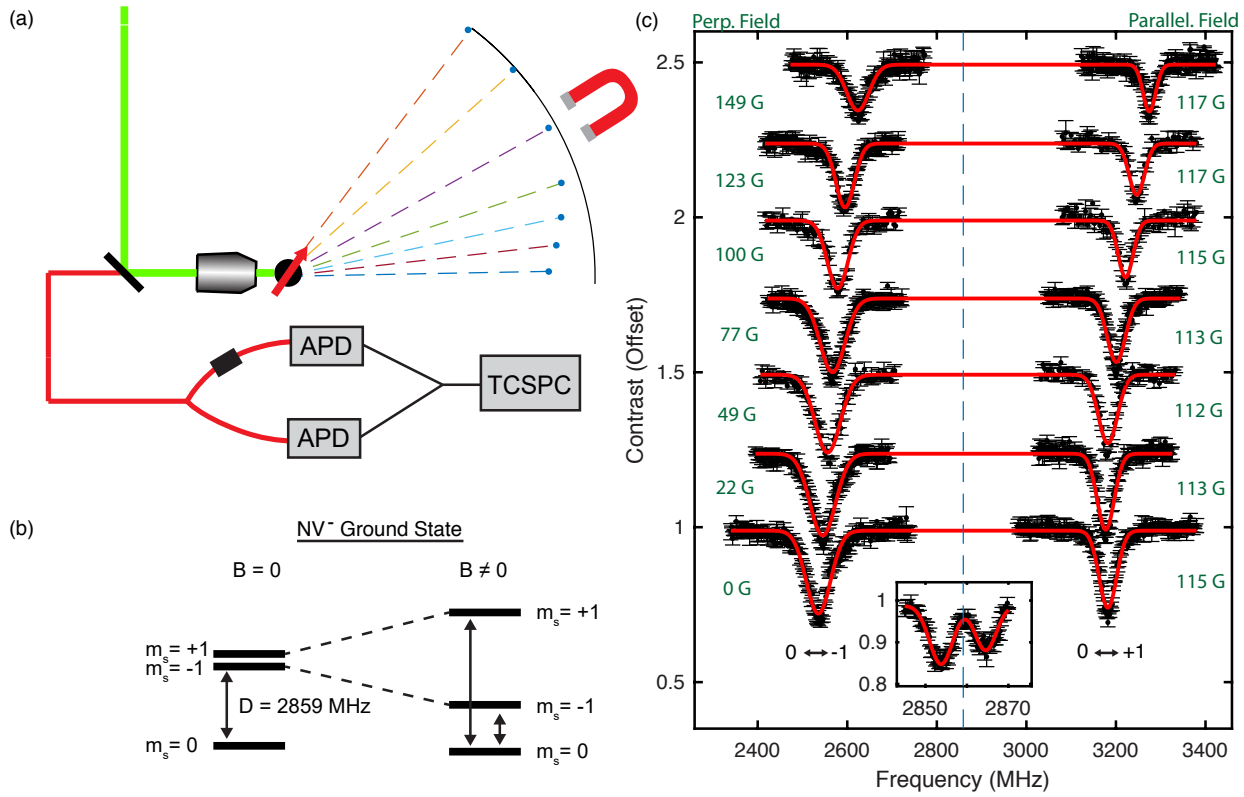

Figure 4.2: **ESR (a)** Schematic of the experimental setup. The location of the NV center is represented as a black circle with a red arrow representing the orientation of the optical dipole. Excitation path is shown in green and the collection path and fiber splitter are shown in red. The 662 nm dichroic filter is shown as a black line. The afterflash filter is shown as a rectangle. Dashed lines represent different magnetic field positions that allow the parallel field to remain constant and the perpendicular field to increase by increments of approximately 25 G. PL is collected into two APDs and photon arrival times are time-tagged by a time-correlated single photon counter (TCSPC). **(b)** Schematic of the NV^- ground state. The configuration of the $m_s = 0$ and $m_s = \pm 1$ states in zero-magnetic field is shown on the left with a zero-field-splitting of 2859 MHz separating $m_s = 0$ and the $m_s = \pm 1$ states. The configuration of the $m_s = 0$ and $m_s = \pm 1$ states in the presence of a magnetic field is shown on the right with transitions between the $m_s = 0$ and $m_s = +1$ and $m_s = 0$ and $m_s = -1$ states shown with arrows. **(c)** ESR measurements at each field condition are shown with $y-$axis offset. ESR dips on the left are from the $m_s = 0$ to $m_s = -1$ transition marked in (b) and ESR dips on the right are from the $m_s = 0$ to $m_s = +1$ transition. The magnetic field condition of each ESR trace is labelled in green with the perpendicular field component to the left of the trace and the parallel field component to the right. Inset shows ESR from the zero field condition with a vertical blue dashed line marking the zero-field splitting.

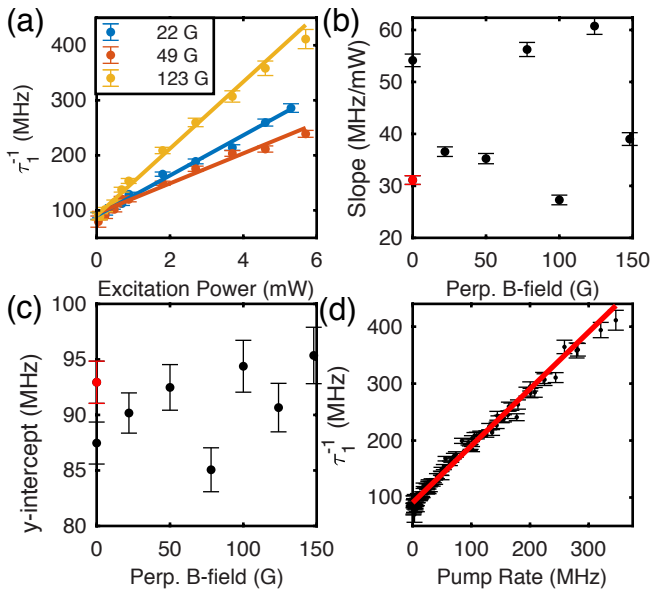

Figure 4.3: **Excitation power correction.** **(a)** Antibunching rate, τ_1^{-1}, as a function of excitation power for three different field conditions. Linear fits to each condition are plotted. **(b)** The slope and **(c)** y-intercept of the linear fits to τ_1^{-1} are plotted for each field condition. Red points in (b) and (c) represent the zero-magnetic-field condition. All errorbars are 68% confidence intervals from fits.

state. Therefore, changes in the setup collection efficiency will be present in the scaling of k_{GE} with respect to calibrated excitation power while k_{EG} is expected to remain constant through shifts in setup collection efficiency.

Figure 4.3 shows the process of correcting for setup alignment shifts across magnetic field conditions through analysis of τ_1. In Fig. 4.3(a), τ_1^{-1} is shown as a function of excitation power for three different magnetic-field conditions: 22 G, 50 G, and 125 G perpendicular fields (113 G, 112 G, and 117 G respective parallel components). The three conditions shown in Fig. 4.3(a) were selected to illustrate the wide variation in setup alignment. In a situation where setup alignment was not affected by magnetic field, we would expect the slope, which is the change in τ_1^{-1} with respect to excitation power, to be the same across all the field conditions. However, we observe that excitation around 6 mW produces roughly double τ_1^{-1} for the 125 G field condition compared to the 50 G condition. The difference in slope between the two conditions corresponds to a nearly double excitation rate k_{GE} for the 125 G field condition. This indicates that the application of the 50 G

magnetic field has shifted the setup alignment to result a decrease in collection efficiency by almost half.

Linear fits to each condition are plotted over the data. The radiative decay rate, k_{EG} is quantified in the y-intercept of the fit, and the alignment-dependence of the internal pump rate ,k_{GE} with respect to excitation power is quantified by the slope. Figures 4.3(b) and (c) show the resulting slopes and y-intercepts respectively from linear fits to τ_1^{-1} at all eight field conditions. The value extracted for the slope is used to convert excitation power into pump rate through the relation, pump rate = power * slope. The y-intercept gives the radiative decay rate, k_{EG}, and is expected to be constant across magnetic field conditions. While most extracted $y-$intercepts in Fig. 4.3(c) are consistent within error, there are a few outliers. This difference can be attributed to a possible underestimation of error. Figure 4.3(d) shows τ_1^{-1} plotted for all field conditions after each is corrected by its slope from Fig. 4.3(b). The slope of a linear fit to the combined corrected data is consistent with 1 within error as expected. The extracted y-intercept is 91 MHz. All subsequent analysis incorporates excitation-power correction and is thus done as a function of pump rate rather than laser excitation power.

4.5. Results and discussion

Figure 4.2(b) shows a schematic depicting the response of the NV^- ground state to an applied magnetic field. At zero magnetic field, the $m_s = \pm 1$ states are nearly degenerate, separated by a small hyperfine splitting. The $m_s = 0$ state and the $m_s = \pm 1$ states are separated by a zero-field splitting of 2859 MHz. The application of a magnetic field leads to a magnetic-field-dependent splitting of the $m_s = +1$ and $m_s =$ -1 states. As a result, the separation between the $m_s = 0$ state and $m_s = +1$ and $m_s =$ -1 states changes with magnetic field. Application of a resonant AC magnetic field through a microwave antenna drives transitions between the spin sublevels. While the NV center is optically polarized to favor the $ms_s = 0$ spin state, the resonant microwaves lead to spin mixing so that the population is more evenly distributed between the $ms_s = 0$ and $ms_s = +1$ or $ms_s = -1$ states. Since the $ms_s = +1$ and $ms_s = -1$ excited states have a higher likelihood to decay into the metastable state, than the $ms_s = 0$ excited state, the spin mixing leads to a decrease

in fluorescence. This is visible in an ESR measurement as a dip in normalized PL as a function of microwave frequency. Figure 4.2(c) shows the offset ESR traces at each magnetic field condition with the inset displaying the zero-field ESR. Due to hyperfine splitting, the resonant transitions between $ms_s = 0$ and $ms_s = +1$ and $ms_s = 0$ and $ms_s = -1$ occur at slightly different frequencies, so two dips are still visible at zero-field. The zero-field splitting is taken to be the average of these two resonances which results in $D = 2859$ MHz.

Figure 4.4 shows example saturation and autocorrelation data for several demonstrative magnetic fields and powers. Figure 4.4(a) depicts $g^2(\tau)$ as a function of changing excitation power for the 123 perpendicular field condition. Qualitative features of the power-dependent dynamics are visible in the low, medium, and high power conditions. As expected, the τ_1 timescale increases with power, which is a result of the increasing pump rate. At low power (50 µW), the spin and charge dynamics occur on timescale that differ by about an order of magnitude. This is because the ionization dynamics are power-dependent and the ionization-recombination process is thus less frequent at lower excitation powers. As a result, τ_3 is on the order of µs and its corresponding bunching amplitude, C_3 is very small. At this low power, the system is most frequently in the ground state configuration. Therefore, the spin-dependent transitions from the excited state to the metastable state, are infrequent. As a result, the bunching amplitude for the spin dynamics, C_2 is also small. As the power is increased, several changes to the dynamics are visible in the $g^{(2)}(\tau)$ curves. The power-dependent charge dynamics timescale shortens until it is of comparable magnitude to the spin dynamics. As a result, for the medium and high power curves, only one bunching process is visible. While a fit may be able to distinguish between the two dominant bunching processes, spin and charge dynamics, at some point around 1 mW excitation, the timescales become too similar, and the best fit model becomes a 2-timescale fit where both the spin and charge dynamics contribute to the fit values for τ_2 and C_2. As a result, tau_2 continues to shorten at higher power as visible on the blue 6 mW curve. At 6 mW excitation, the value of $g^{(2)}(\tau)$ at low τ increases. This is likely an affect of the setup instrument response function (IRF). As the power increases and tau_1 shortens, it eventually becomes comparable to the timescale of the IRF.

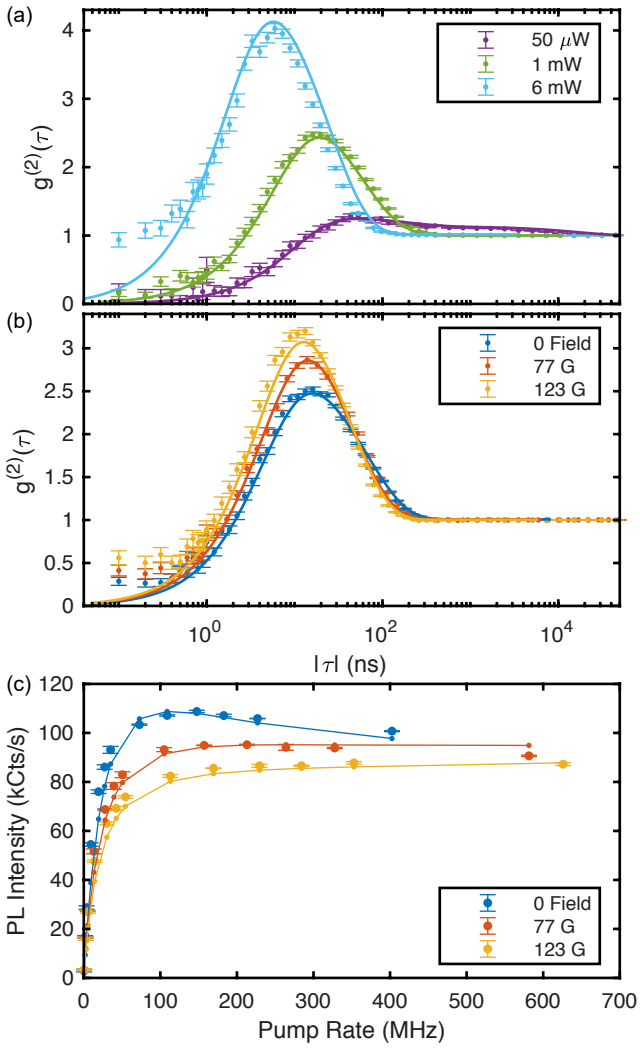

Figure 4.4: **Example $g^2(\tau)$ and saturation measurements. (a)** PECS as a function of excitation power. $g^2(\tau)$ is shown for 123 G perpendicular field at 50 µW, 1 mW, and 6 mW excitation powers. **(b)** PECS as a function of magnetic field. $g^2(\tau)$ is shown for $\approx$ 100 MHz pump rate for the 0 Field, 77 G perpendicular field (113 G parallel), and 123 G perpendicular field (117 G parallel) conditions. **(c)** Saturation curves. PL intensity as a function of pump rate for three field conditions: 0 Field, 77 G, and 123 G. Solid curves in (a-c) are lines connecting fits to simulations of the same field and power conditions as each set of data. Simulation results in (c) are normalized to align with the data.

Figure 4.4(b) depicts $g^2(\tau)$ as a function of changing changing magnetic field. The three field conditions are 0 field, 77 G perpendicular field (113 G parallel), and 123 G perpendicular field (117 G parallel). Each curve was taken with different laser excitation powers, but after calibration exhibit comparable pump rates of ≈ 100 MHz. Therefore, the effective excitation rate is constant across the three field conditions and deviations in $g^2(\tau)$ features can be attributed to magnetic-field-dependent dynamics. At this excitation-power regime, the $g^2(\tau)$ curves are best described by two-timescale fits. The most significant feature that changes with increasing perpendicular magnetic field is the bunching amplitude, C_2. The increase in C_2 is a result of the spin dynamics. The perpendicular magnetic field results in a depolarization of the system from the $m_s = 0$ spin sublevel. Therefore, a higher likelihood for the system to decay from the excited state through the metastable state resulting in an increase in bunching from this process. The timescale τ_2 appears to stay roughly the same decreasing slightly with increasing magnetic field. This is due to the greater contribution of the faster $m_s = \pm 1$ excited state dynamics to τ_2.

Figure 4.4(c) shows the result of saturation measurements taken at three field conditions: zero field, 77 G perpendicular field (113 G parallel), and 123 G perpendicular field (117 G parallel). The recorded PL intensity cannot be compared across field conditions due to the aforementioned shifts in collection efficiency. However, the pump rate is consistent across field conditions, so the shape of each curve is informative. For a two-level system, a saturation measurement reflects the ratio of the pump rate to the radiative decay rate. At low powers, as the pump rate increases, the PL intensity increases. However, as the pump rate surpasses the radiative decay rate, that decay rate becomes a limiting process in PL emission. As a result, the PL Intensity reaches a limit and saturates at that value. However, in the NV center, competing power-dependent processes result in a saturation turnover where after the maximum PL intensity is reached due to the limiting decay rate, the PL intensity then begins to decrease with increasing power. This feature is visible in the 0 Field saturation data of Fig. 4.4(c). However as a magnetic field is applied and the perpendicular component of the field is increased, the saturation turnover lessens until the power-dependent behavior more closely resembles that of a two-level system. In the 0 Field case, the PL intensity is maximized at a pump rate that is high enough to populate the excited state, but not

high enough to result in significant ionization to the dark NV^0 state. As the power increases, the ionization rate ($k_i 8$ in Fig. 4.1(a)) begins to drain population from the NV^- excited state to NV^0. This results in a slight decrease in PL intensity at higher powers. As a perpendicular magnetic field is applied, the increase in decay through the metastable state, results in a decrease in overall PL as the steady-state population of the $m_s = 0$ excited state decreases. Therefore, saturation of the excited state population occurs at a higher power, at which point, the ionization rate is high enough to compete with the decay rate into the metastable state. As a result, the saturation turnover at higher powers becomes less pronounced as the perpendicular magnetic field increases.

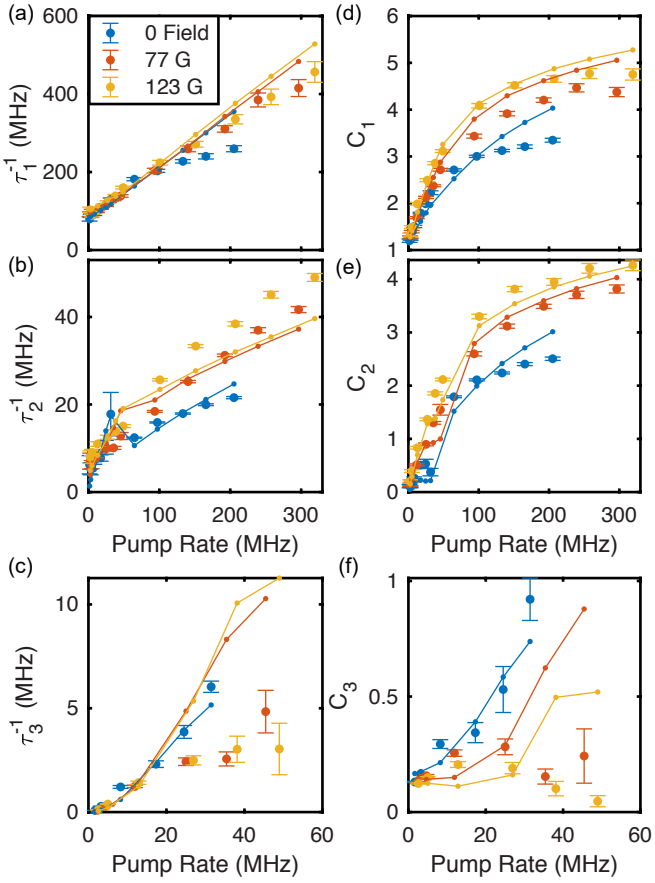

Figure 4.5: **PECS fit parameters.** The resulting fit parameters from two- and three-timescale fits to $g^{(2)}(\tau)$ curves as a function of power (pump rate) for three magnetic fields: 0 Field, 77 G perpendicular field (113 G parallel), and 123 G perpendicular field (117 G parallel). Fit values from PECS simulations at each power and magnetic field are also shown as small points connected with lines for visibility. **(a-c)** PECS timescales **(a)** τ_1^{-1}, **(b)** τ_2^{-1}, and **(c)** τ_3^{-1} and **(d-f)** their accompanying antibunching/bunching amplitudes, **(d)** C_1, **(e)** C_2, and **(f)** C_3.

Figure 4.5 shows the timescales and bunching amplitudes extracted from fits to $g^{(2)}(\tau)$ measurements as a function of excitation power for three magnetic field conditions: zero field, 77 G perpendicular field (113 G parallel), and 123 G perpendicular field (117 G parallel). Figure 4.5(a) shows the extracted values for τ_1^{-1} as a function of excitation power. In Fig. 4.3(d), the results of τ_1^{-1} for all field conditions follows the expected linear trend as a function of pump rate. However, in Fig. 4.5(a), looking at results from just a few magnetic-field conditions, it appears that the zero field data deviates from that linear trend.

The AIC analysis determined that around a 50 MHz pump rate, the model that best captures the data switches from a three timescale to a two timescale model Therefore, for low excitation power with a pump rate less than 50 MHz, we fit the $g^{(2)}(\tau)$ curves to a three timescale model. For a pump rate greater than 50 MHz, we fit the data to a two timescale model. For the three timescale fits, the spin and charge dynamics are distinguishable among the fit parameters as τ_2 and τ_3 respectively. However at higher powers, the spin and charge timescales are of a similar order and therefore are not distinguishable by the fit. As a result, in the higher power regime, τ_2 captures both charge and spin dynamics.

Figure 4.5(b) shows τ_2^{-1} as a function of excitation power. At low powers with the three timescale fit, the limiting rate in the spin dynamics is the pump rate therefore the rate describing the metastable decay is expected to increase with power until it eventually saturates when the metastable decay becomes the rate limiting step step. However at higher power, τ_2^{-1} incorporates the charge dynamics as well which are not expected to saturate at higher power, as the ionization and recombination processes consist of rates that are excitation-power driven. Therefore, the close-to-linear trend in τ_2^{-1} at higher powers reflects this. Figure 4.5(b) also shows an increase in τ_2^{-1} with increasing perpendicular magnetic field. This is expected, as the decay rate from the excited to metastable state is roughly 10 times higher for the $m_s = \pm 1$ spin sublevels than for the $m_s = \pm 0$ spin level. The increase in $m_s = \pm 1$ due to the applied perpendicular magnetic field means that that faster decay rate to the metastable state contributes more to the overall τ_2^{-1}.

Figure 4.5(c) shows τ_3^{-1} as a function of excitation power in the low power regime and Figure 4.5(f)

shows the corresponding bunching amplitude, C_3. As the pump rate approaches 50 MHz, the difficulty of the fit in resolving the independent contributions of the spin and charge dynamics is apparent in the low values of C_3 for the 73 G and 123 G field conditions. With the low bunching amplitudes, it is also more difficult for the fit to resolve the corresponding timescale, so the corresponding values for τ_3^{-1} close to 50 MHz are uncertain. However, the 0 field τ_3^{-1} data shows the expected trend for the charge dynamics which is to increase with power without saturating.

Figure 4.5(a) shows the antibunching amplitude, C_1 for the radiative decay process. The saturation behavior visible reflects the decrease in the likelihood of radiative decay as other processes, particularly charge transitions, become more likely to occur. Furthermore, the value of C_1 begins to decrease at the highest pump rate, indicating a regime where the charge dynamics begin to approach the magnitude of the radiative dynamics.

Figure 4.5(a) shows the bunching amplitude, C_1. The increase in C_2 with respect to perpendicular magnetic field is expected as the increase in magnetic field leads to an increased likelihood for the metastable decay process to occur with respect to the radiative decay process. The saturation behavior likely reflects the saturation of the excited state at which point the frequency of decay through the metastable state is limited by the corresponding decay rate. While the increased power results in an increase in transitions to the NV^0 manifold, which increases C_2 and C_3 with power, it also results in an increase in transitions back to the NV^- manifold. Therefore, this balance still allows C_2 to saturate at higher powers.

To heighten understanding of the features observed in the fits to PECS data (4.5), we simulate the dynamics of the NV center. The simulation uses a rate equation,

$$\dot{P} = GP, \tag{4.7}$$

with the initial conditions given by Eq. 3.21, to classically model the evolution of state populations over time. Here, P is a vector of state populations, and G is a generator matrix composed of all the transition rates, k_{ij} from state i to state j. $g^{(2)}(\tau)$ is then calculated from the time-dependent and

steady-state populations using the Eq. 3.22. Informed by the spectral filtering in the setup, we set the simulation collection efficiency from the NV^- radiative transitions to be 73% and the collection efficiency from the NV^0 radiative transition to be 9%. The input parameters consist of transition rates in the zero-magnetic-field condition. In the presence of a magnetic field, the transition rates are projected onto a new basis with their projection determined by the diagonalization of the state Hamiltonian in the presence of a magnetic field (Eq. 4.1). For the ground state zero-field splitting parameter, we use our measured value of 2859 MHz with a g-factor of 2.0028. For the excited state zero-field paramater, we use a reported value of D = 1425 MHz with a g-factor of 2.01 [52]. We also introduce a spin relaxation transition of 0.001 MHz (not pictured in Fig. 4.1) that is symmetric between all the NV^- ground state spin sublevels. No spin relaxation transition is specified between the excited state spin sublevels.

In order to simulate PECS, we consider the NV center model consisting of the nine states shown in Fig. 4.1(a). We establish transition rates for the model, drawing from previous experiments on this NV center and filling in gaps with other reports about NV center dynamics. Lifetime measurements in NV^- constrain the various decay rates from excited states. Prior measurements with the NV center discussed in this manuscript have yielded lifetimes of 12.50 $\pm$ 0.02 ns for the $m_s = 0$ excited state [66], 7.48 $\pm$ 0.02 ns for the $m_s = \pm 1$ excited state [66], and 182 $\pm$ 10 ns for the metastable state [65]. These measurements in conjunction with estimates of branching ratios from the literature, allow the calculation of transition rates to and from the metastable state. The branching ratio from the excited to metastable state, $(k_{67} + k_{57})/(2k_{47})$, is estimated to be 10 [55]. The branching ratio from the metastable to ground state, $(k_{72} + k_{73})/(k_{71})$ is estimated to be 1.3 [16]. The radiative decay rate in NV^0, k_{98} is determined from a reported lifetime measurement of 20.7 ns [18].The ionization and recombination rates are estimated from Wirtitsch *et al.* [147] and are adjusted to qualitatively fit the data. The NV^0 excitation rate is set to the same as that of the NV^-, although estimates have placed the NV^0 cross-section closer to half that of NV^- [147].

For each of the magnetic field and power conditions, $g^{(2)}(\tau)$ curves are simulated and fit with the same fit function used to describe the data. The number of timescales in the fit model are chosen

to match the timescales given by AIC calculations of fits to the experimental data. Bunching amplitudes and timescales are extracted from each fit and are plotted in Fig. 4.5 as small points at each power and field condition shown in the data. The simulation points are connected with lines to improve visibility. Table 4.1 shows the simulation parameters that gave the simulation fit values shown in Fig. 4.5 and the curves in Fig. 4.4. Rates with an x indicate power-dependent rates,

k_{41}, k_{52}, k_{63}	74 MHz	k_{98}	37 MHz
k_{14}, k_{25}, k_{36}	74x MHz	k_{89}	74x MHz
k_{47}	6 MHz	k_{71}	3.1 MHz
k_{57}, k_{67}	60 MHz	k_{72}, k_{73}	1.2 MHz
k_{48}, k_{58}, k_{68}	10x MHz	k_{91}, k_{92}, k_{93}	7.4x MHz
k_{13}, k_{12}, k_{31}, k_{21}, k_{23}, k_{32}	0.001 MHz	k_{46}, k_{45}, k_{64}, k_{54}, k_{65}, k_{56}	0 MHz
k_{97}	5x MHz	k_{78}	0.5x MHz

Table 4.1: **NV simulation parameters.**

where x is a scaling factor to scale all power-dependent rates with respect to the NV^- pump rate. While the starting parameters gave an approximate match to the data observed in Fig. 4.5, τ_2^{-1} was initially significantly underestimated. While increasing the ionization and recombination rates increased τ_2^{-1}, the resulting affect on the other PECS parameters caused further divergence from the experimental results. To address this, we introduce an additional ionization and recombination pathway to and from the NV^- metastable state and NV^0 with rates k_{97} and k_{78}. The values for these transition rates that give the best fit are shown in Table 4.1. The value for k_{97} is approximately half that proposed by Wirtitsch *et al.*, and the value for k_{78} is comparable to the proposed rate of excitation from the metastable state into the conduction band [147]. While the addition of this transition pathway leads to better agreement with τ_2^{-1}, the simulation still underestimates the rate and the contrast as a function of magnetic field. Further model complexity, such as spin-dependent ionization and recombination rates [154], may be needed to achieve further improvement of simulation agreement with the data.

4.6. Future directions

While the dynamics of the NV^- charge state have been well explored, charge dynamics and NV^0 are beginning to generate more interest due to their potential to enhance applications. Recent studies have looked to map out the fine structure [13] and orbital and spin dynamics [9] of the neutral NV center. In addition to enhanced state readout through spin-to-charge conversion, demonstrations have shown NV charge dynamics can also be utilized to enhance the coherence time of a nuclear memory, [89, 104] and the NV^0 itself can be used for state storage [40].

The experiment discussed in this chapter illustrates how pairing PECS with an experimental variable can isolate and reveal specific dynamics. While this chapter was focused on studying spin and charge dynamics by changing excitation power and magnetic field, PECS can also be used to gain further insight into the dynamics of NV^0. Future PECS experiments in which the collection efficiency from the NV^0 radiative decay is varied can be paired with PECS simulations to probe the dynamics of the NV^0 metastable transition and provide further clarity on the NV center charge dynamics.

The general approach to studying spin and charge dynamics through varying magnetic field and excitation power can provide more detailed information about a known system such as the NV center. However, it can also be applied to systems that are less well understood to explore the presence of unknown spin and charge states. In such a case, it is necessary to supplement PECS measurements with other experiments to construct a model for electronic structure and constrain transition rates. An example of this will be explored in the next chapter.

CHAPTER 5

OPTICAL DYNAMICS OF A SINGLE SPIN IN HEXAGONAL BORON NITRIDE

This chapter is adapted from a manuscript currently under review. The experiments and analysis of this chapter were completed with the help of Dr. Raj Patel, Dr. Tzu-Yung Huang, Jordan Gusdorff, and David Fehr.

A series of recent observations have confirmed the potential of h-BN as a host for quantum defects. Room-temperature optical emitters in h-BN have shown single-photon emission [103]. Select emitters further exhibit magnetic-field-dependent photoluminescence, optically detected magnetic resonance (ODMR), and quantum-coherent spin oscillations [58, 48, 56, 33, 127], all of which are prerequisites to establishing optically addressable spin qubits in h-BN.

Despite this progress, paramagnetic single-photon emitters are a minority of those reported on in h-BN, with recent observations noting a yield of $\sim$5% [127]. Emitters in h-BN exhibit heterogeneous optical and spin properties that vary dramatically even within the same sample [47]. Many questions therefore remain about the nature of these emitters. Ultimately, the informed design of spin control protocols that are optimized for applications requires a detailed understanding of their optical and spin dynamics.

In this chapter, we investigate an emitter in h-BN that exhibits single-photon emission and ODMR at room temperature. We probe the emitter's optical and spin dynamics using photon emission correlation spectroscopy (PECS) [51] and time-domain optical and microwave control. Guided by these experiments, we develop a model for the emitter's energy-level structure, and we determine the rates that govern its optical and spin dynamics using quantitative simulations. We design a readout protocol for the spin state that optimizes the signal-to-noise ratio (SNR).

5.1. Experimental Characterization

We characterize the emitter's optical dynamics under ambient conditions using a custom-built confocal microscope [103, 51]. The emitter is illuminated with either of two continuous-wave (cw)

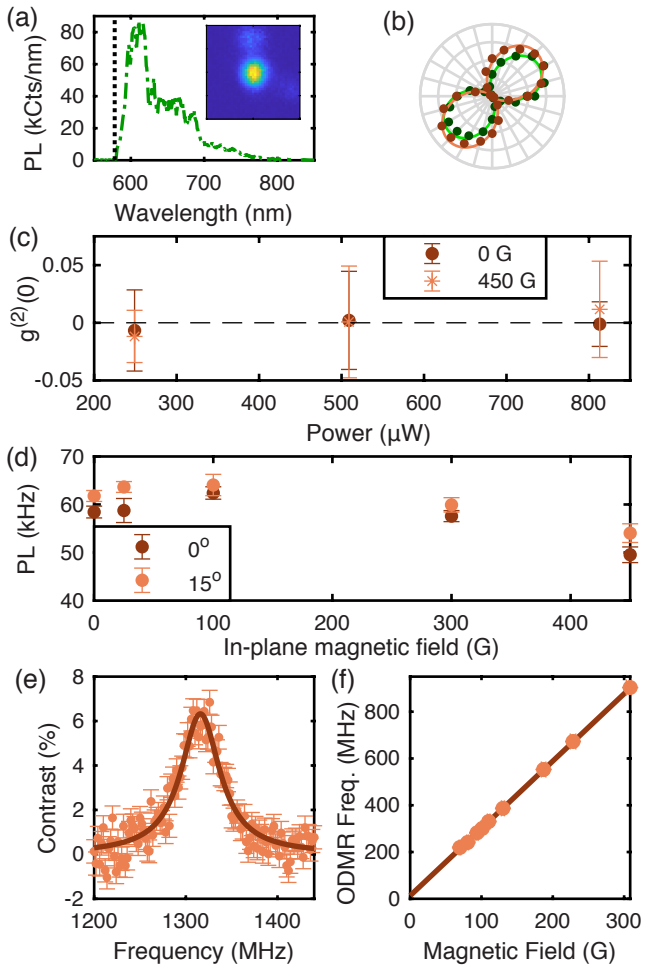

Figure 5.1: **Optical characterization and ODMR. (a)** PL emission spectra with black dotted line representing cut-on wavelength of long-pass dichroic filter in the collection path. Inset: μ-PL image (2×2 μm^2) of the single spin. **(b)** PL intensity as a function of linear excitation polarization angle for 532 nm (green circles) and 592 nm (orange circles) excitation. Solid curves are fits to the data. **(c)** Photon autocorrelation function at zero-delay as a function of optical power for two different in-plane magnetic fields at 0° dipole orientation. **(d)** The time-average PL emission as a function of an in-plane magnetic field for 0° and 15° dipole orientation. **(e)** Cw ODMR spectrum (circles) at 470 G applied magnetic field and 0° dipole orientation. A Lorentzian fit (solid line) gives a resonance frequency of 1315.9 ± 0.8 MHz and a full-width half-maximum of 52 ± 2 MHz. **(f)** Resonance frequency measured using pulsed ODMR as a function of in-plane magnetic field. The solid line is a linear fit to the data. The x- and y-axis error bars are the same size as the data points. Error bars for (**e**) are propagated from Poisson error. All other error bars represent 68% confidence intervals.

lasers operating at 532 nm and 592 nm wavelengths, where excitation power and polarization are controlled. The samples are from bulk, single crystals purchased from HQ Graphene. They are

mechanically exfoliated in thin (≤100 nm) and large area (∼10 µm) flakes using a dry transfer process [70] and transferred to a SiO_2/Si substrate patterned with circular trenches [47]. The samples are annealed in a tube furnace at 850 °C in low flow Ar atmosphere for 2 hours. We have found this annealing condition to create stable emitters. We find the single spin to be extremely stable in ambient conditions with optical pumping up to 500 µW and microwave pulses with RF power up to 4 W for over hundreds of hours. The resulting sample consists of a mechanically exfoliated h-BN flake (≤ 100 nm) suspended on a patterned SiO_2/Si substrate [47, 103].

We raster a fast steering mirror to acquire µ-PL images of the h-BN flake and isolated emitters by recording the counts at each pixel. In an area of $\approx 25 \times 25$ µm^2, one emitter exhibited magnetic-field-dependent photoluminescence (PL), amongst ≈ 20 nonmagnetic emitters. Data recorded under 592 nm (532 nm) excitation are plotted in orange (green) in the relevant figures. All PECS, ODMR, time-domain, and spin dynamics measurements were performed under 592 nm illumination.

Figure 5.1(a) shows the emitter's PL spectrum under 532 nm excitation. The excited state lifetime is found to be 7.8 ± 0.1 ns through PECS analysis (discussed later). The polarization scans shown in Fig. 5.1(a) and Fig 5.2 are acquired to measure the linear excitation and emission polarization properties. The measurements are acquired by varying the linear polarization of the excitation laser or by passing the PL through a linear polarizer placed in the collection path. The polarization dependent PL signal is determined by recording the steady-state PL of the SPE at each polarization angle and subtracting the background PL measured at a spatial location offset ∼1 µm from the SPE. A randomized order of the polarization angles minimizes effects of drift and hysteresis. For excitation polarization measurements, the linear polarizer in the collection path is removed. For emission polarization measurement, the excitation polarization is set to maximize the PL. The emitter's optical excitation is highly polarized (visibility 93 ± 3%) and aligned for both 532 nm and 592 nm excitation (Fig. 5.1(b)). The emitted PL is polarized along the same axis (Fig. 5.2). While previous observations have noted heterogeneous polarization responses for h-BN's emitters [75, 47, 77, 153, 103], indicating the presence of multiple electronic excited states, the aligned excitation and emission dipoles observed for this emitter are consistent with a single radiative

excited state. Figure 5.1(c) shows the second-order photon autocorrelation function, $g^{(2)}(\tau)$, at zero-delay ($\tau = 0$), in the presence and absence of an applied magnetic field. After accounting for experimental uncertainties, in both cases we observe noise-limited photon antibunching, $g^{(2)}(0) = 0$, independent of optical excitation power.

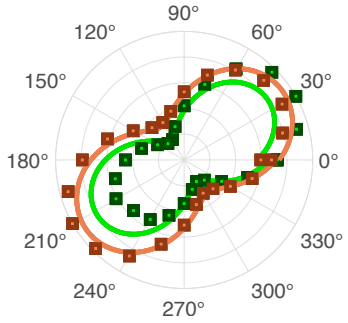

Figure 5.2: **Emission Polarization** Polar plot showing polarization dependence of emission for 532 nm (shown in green) and 592 nm (shown in orange) excitation.

This emitter's PL intensity is modulated by applied dc and ac magnetic fields. Magnetic fields affect a paramagnetic defect's PL intensity due to spin-selective transition rates that govern its optical dynamics, although this can occur in different ways [42, 48, 51, 46]. We apply a dc magnetic field parallel to the h-BN surface and rotate the sample about the optical axis to vary the relative orientation of the optical excitation dipole to the field axis (referred hereafter as dipole orientation). As observed in Fig. 5.1(d), the steady-state PL varies by 15% on increasing the magnetic field strength from 0 G to 470 G for both 0° and 15° dipole orientations. Accompanying variations in PECS measurements (Fig. 5.3) confirm that the PL changes result from magnetic modulation of the emitter's optical dynamics. Figure 5.1(e) shows an example of an ODMR spectrum acquired as a function of applied microwave frequency. The microwaves are amplitude modulated at 12.5 kHz, and the ODMR spectrum is normalized by dividing the signal PL (microwaves on) by the reference PL (microwaves off).

Figure 5.1(f) shows a linear fit to the best-fit ODMR center frequency as a function of applied magnetic field at 1.8° dipole orientation. We repeat this measurement for 34.2°, 66.6° and 90° dipole orientation (Fig. 5.4) and find an isotropic $g \approx 2$, consistent with the free-electron g-factor, and

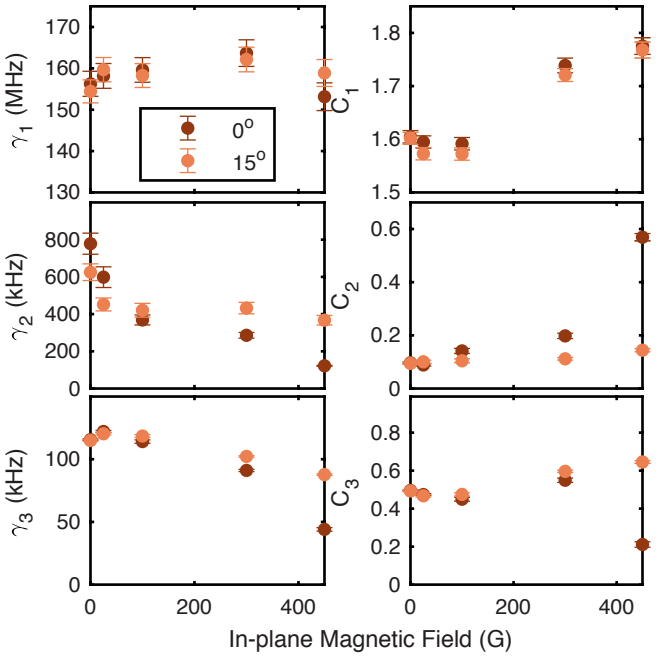

Figure 5.3: **Magnetic-Field-Dependent Optical Dynamics.** Result of PECS measurements as a function of an in-plane magnetic field for 0° and 15° dipole orientation. All error bars represent 68% confidence intervals.

an average zero-field-splitting (ZFS) of 9 ± 10 MHz (Fig. 5.5). Given the order of magnitude of the ZFS and that it is consistent with zero within experimental uncertainty, we interpret this as an absence of ZFS. The scale of the ZFS is consistent with prior reports, although interpretations of its significance have varied and will be discussed in Sec. 5.6 [33, 127]. We observe no additional resonances at higher frequencies up to 4.2 GHz. Based on these observations, we postulate a doublet ($S = \frac{1}{2}$) spin state. However, we acknowledge higher-level spin configurations, while less likely, are possible.

5.2. Spin Structure

Figure 5.8(a) shows the proposed model explaining the observed optical dynamics. The model features a metastable spin ($|M_{1,2}\rangle$), which we propose to be a spin-1/2 doublet, coupled to a spin-less manifold of ground ($|G\rangle$) and optically excited ($|E\rangle$) states. We further identify a stochastic modulation of the optical decay pathway, fluctuating between a raditative and non-radiative transition. Arrows denote transitions with corresponding rates, k_{ij}, between states i and j, with the

spin relaxation rate labelled T_1^{-1}. The number and arrangement of levels are determined by a series of experiments and corresponding simulations. PECS measurements (discussed later), show clear

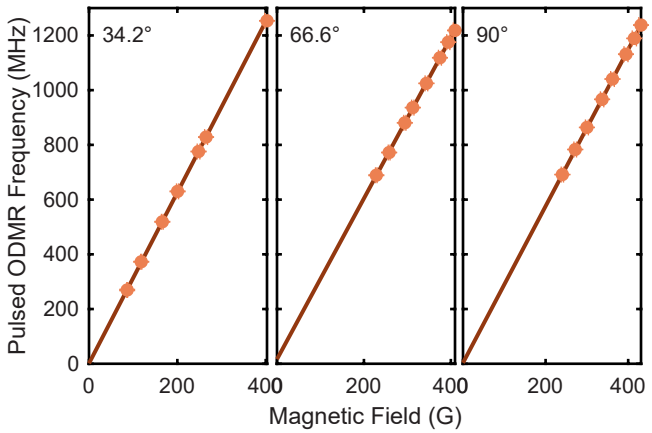

Figure 5.4: **Resonance frequency at various dipole orientations.** The circles represent resonance frequency for a given dipole orientation at an in-plane magnetic field, determined using a Lorentzian function. The data were acquired at 350 µW optical power and 28 dBm microwave power for 34.2° orientation and 1 W for 66° and 90° orientation. The solid line is a fit to the data using a linear function. The error bars are same as the size of the data points and represent 68% confidence intervals.

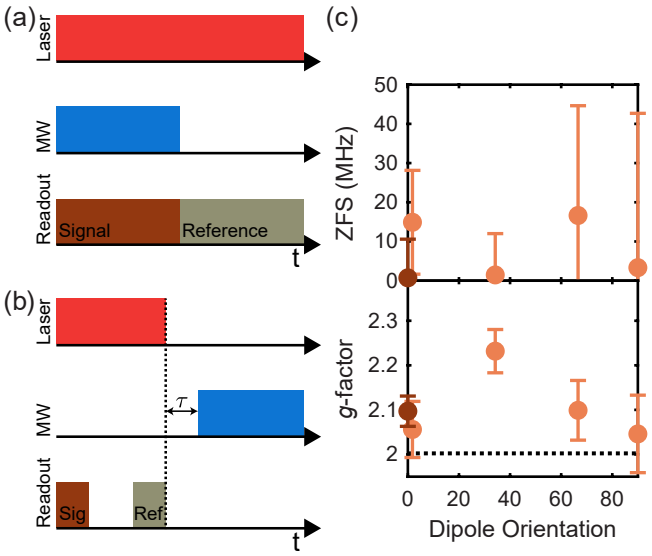

Figure 5.5: **B-field-dependent optically detected magnetic resonance. (a)** Pulse protocol for cw ODMR. **(b)** Pulse protocol for pulsed ODMR. **(c)** The zero-field splitting (ZFS) and g-factor as a function of dipole orientation. The light (dark) orange data are obtained from pulsed (cw) ODMR. All error bars represent 68% confidence intervals.

evidence of photon bunching associated with metastable dark configurations.

PECS experiments also reveal the nature of the transition mechanisms between these configurations [51]. Signatures of these transition mechanisms are contained within the power-dependent behavior of γ_3 (Fig. 5.8(f)) and its associated bunching amplitude, C_3 5.12(c). As a first pass, a 3-level model can give preliminary insight into the power dependence of metastable rates. In a 3-level model where γ_3 describes the metastable decay process, approximations for k_{EM} and k_{MG} can be given by,

$$k_{\mathrm{EM}} = \frac{\gamma_1\gamma_3(C_{\mathrm{T}}-1)}{C_{\mathrm{T}}k_{\mathrm{GE}}} \tag{S1}$$

$$k_{\mathrm{MG}} = \frac{\gamma_3}{C_{\mathrm{T}}}, \tag{S2}$$

where C_{T} is the total bunching [21]. Substituting our PECS data into this approximation with $C_{\mathrm{T}} = 1+C_2+C_3$, predicts a power-independent k_{EM} and a power-dependent k_{MG} shown in Fig. 5.6. Notably, the y-intercept of k_{MG}, though small, is nonzero, implying a spontaneous component to the rate in addition to a pumped, power-dependent component.

PECS simulations of our full model (Fig. 5.8(a)) confirm these predictions as shown in Fig. 5.7. Adding in a power dependent k_{MG} significantly improves the shape matching for the bunching amplitude and timescale of the metastable decay process. With a power-dependent k_{MG}, the bunching amplitude, C_3, exhibits saturation and turnover consistent with the data. Without a power-dependent k_{MG}, C_3 increases monotonically, diverging from the data. The power-dependent k_{MG} also decreases the y-intercept of γ_3 and increases its slope, leading to better agreement with the data. Therefore, we model the rates $k_{\mathrm{M_1G}}$ and $k_{\mathrm{M_2G}}$ each with a power-dependent component in addition to a spontaneous (power-independent) component.

We propose that the spin doublet state observed in ODMR exists in a metastable configuration. This arrangement cannot be determined by ODMR alone. Rather, it is confirmed by an optical spin contrast experiment, shown in Fig. 5.8(b-c), which distinguishes between configurations where the spin states exist in the optical excitation/emission manifold compared to the metastable configuration. As shown in Fig. 5.8(b), the laser is modulated on and off, with a dark time of duration τ_{D},

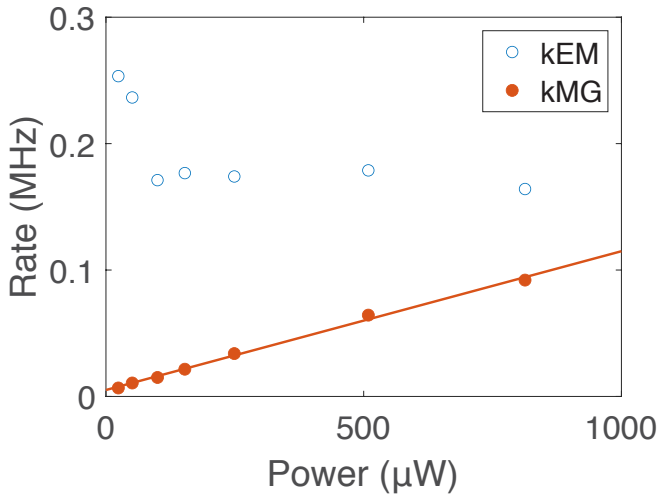

Figure 5.6: **Calculated metastable rates from 3-level approximation.** k_{EM} and k_{MG} calculated from Eqs. S 5.1 and S 5.2. A linear fit to k_{MG} is shown.

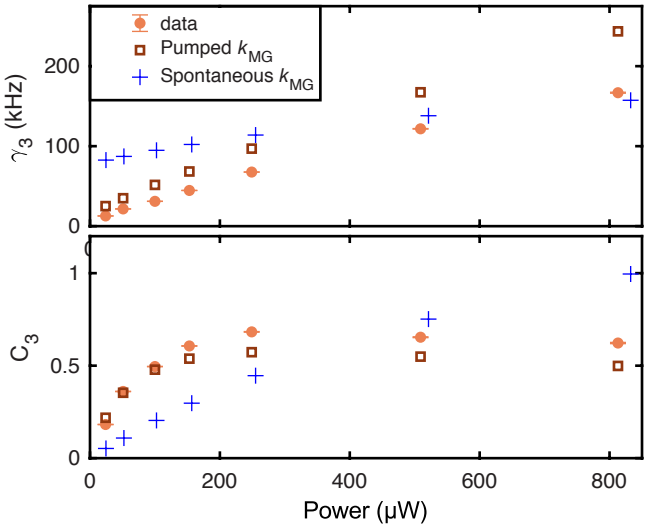

Figure 5.7: **Simulation of PECS parameters for pumped and spontaneous k_{MG}.** A comparison between simulated γ_3 (top panel) and C_3 in the case of a model with a pumped (power-dependent) k_{MG} shown as brown boxes contrasted with a spontaneous (power-independent) k_{MG} shown as blue crosses. Data is shown as orange points.

and a microwave pulse can be applied during the dark time following a wait time, τ_{w}. Figure 5.8(c) shows the PL as a function of time during the laser pulse in situations when the microwaves are applied (signal) or not (reference).

We consider in turn the expected dynamics for configurations with spin doublets in the optical

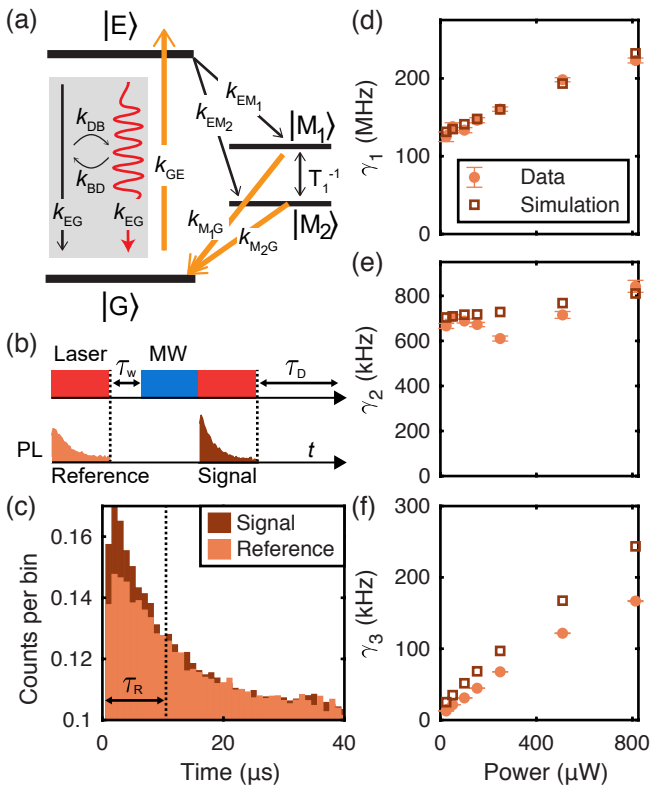

Figure 5.8: **Energy-level model and optical dynamics.** **(a)** Energy-level model made up of a singlet ground and excited state, and a metastable doublet. The gray box highlights fluctuations between a nonradiative decay path (black arrow) and radiative decay (red, wavy arrow). Orange arrows depict excitation-power-dependent transitions. **(b)** Pulse protocol for optical spin contrast measurement. "Reference" and "Signal" denote timing windows during which photons are counted. **(c)** PL counts for 1 μs time bins corresponding to signal (dark orange circles) and reference (light orange circles) readout, at 350 μW optical power, 470 G magnetic field, 20 μs wait time, and 40 μs microwave pulse. Dashed line indicates approximate time where contrast disappears with τ_R denoting a readout window. **(d)-(f)** PECS measurements. **(d)** The antibunching rate, γ_1, and the bunching rates, **(e)** γ_2 and **(f)** γ_3, as a function of optical excitation power at 0 G magnetic field.

ground and excited states compared to the configuration shown, with a metastable doublet. First we note the positive ODMR contrast observed (Fig. 5.1(e)). For the configuration with spin doublets in the optical manifold, positive ODMR contrast implies that the laser polarizes the spin to favor the spin state with higher probability of decay into the metastable state. A resonant microwave field depolarizes the spin, decreasing the probability of decaying through the metastable state, increasing the PL intensity. In a spin contrast measurement, this lower non-radiative decay probability manifests as a slower decay in the signal PL from its peak to its steady state, compared

to that of the reference. Meanwhile, the microwave does not affect the metastable state's decay rate to the optical ground state, so the initial PL intensity remains unchanged. We would therefore expect to see a nonzero initial contrast that decays as the system returns to the steady state.

On the other hand, for the metastable spin doublet configuration, positive ODMR contrast implies that optical excitation polarizes the spin to favor the slower-decaying metastable spin state. The microwave pulse increases the probability of decay from the metastable state to the ground state. We therefore expect to observe initial spin contrast when the laser is turned on, with a contrast evolving during the pulse due to spin-dependent decay rates. Our results in Fig. 5.8(c) show significant spin contrast within the first 10 µs of readout, followed by a similar decay time for both the signal and reference, consistent with the metastable doublet configuration. This finding, in conjunction with the power-dependent transitions from the metastable state, could be indicative of a transition between charge manifolds, similar to that observed in the NV-center between NV^- (S = 1) and NV^0 (S = 1/2). Informed by classical rate equation simulations of a spin contrast experiment for the model shown in Fig. 5.8(a), we estimate an upper limit on the spin relaxation rate of $T_1^{-1} \sim$ 0.01 MHz to achieve a similar initial contrast (7%) in simulations.

5.3. Optical dynamics

After establishing the main features of the electronic level structure, we next consider the rates that govern its optical dynamics. Using PECS, we acquire $g^{(2)}(\tau)$ at various optical excitation powers. To analyze the data, we follow the procedure from previous works (see Ref. [103], Appendix, Sec. 6c), evaluating the Akaike information criterion and reduced chi-squared statistics for n-timescale models. This analysis determines the best-fit empirical function to be a three-timescale model,

$$g^{(2)}(\tau) = 1 - C_1 e^{-\gamma_1|\tau|} + C_2 e^{-\gamma_2|\tau|} + C_3 e^{-\gamma_3|\tau|}, \tag{5.3}$$

where τ is the delay time, γ_1 and C_1 are the antibunching rate and amplitude, γ_2 and γ_3 are the bunching rates, and C_2, C_3 are the associated bunching amplitudes. Both γ_1 and γ_3 increase monotonically as a function of optical excitation power (Figs. 5.8(d) and 5.8(f)), as expected for processes involving optical pumping to the excited state. In contrast, γ_2 shows no clear trend with

respect to power (Fig. 5.8(e)).

Each PECS rate originates from transition pathways between multiple electronic states that define a distinct process. In this model, γ_1 corresponds to optical excitation at rate k_{GE} followed by relaxation back to $|\mathrm{G}\rangle$ at rate k_{EG}. For a direct optical transition between two electronic states, as in this model, the antibunching rate is given by $\gamma_1 \approx k_{\mathrm{GE}} + k_{\mathrm{EG}}$ [21, 51]. Since k_{GE} is proportional to the optical excitation power, p, whereas k_{EG} is power-independent, we expect a linear variation, $\gamma_1 = k_{\mathrm{EG}} + \beta p$, where β is a proportionality constant. The observations in Fig. 5.8(d) are consistent with this expectation, and a linear fit (Fig. 5.9) yields $k_{\mathrm{EG}} = 128 \pm 2$ MHz (7.8 ± 0.1 ns lifetime) and $\beta = (0.125 \pm 0.005$ MHz/μW).

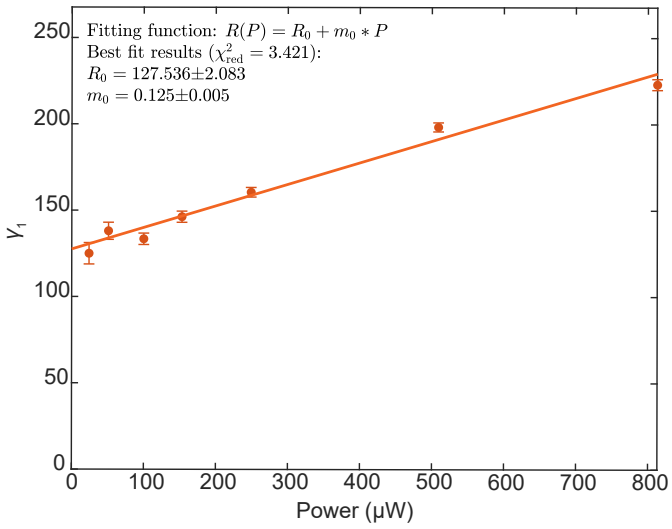

Figure 5.9: **Antibunching Dynamics** Linear fit of γ_1 from Fig. 5.8(d) as a function of optical excitation power . Error bars represent one standard deviation.

The bunching rates γ_2 and γ_3 represent processes through which the system enters nonradiative configurations. The process of optical excitation to $|\mathrm{E}\rangle$ followed by nonradiative decay through $|\mathrm{M}_{1,2}\rangle$ back to $|\mathrm{G}\rangle$ depends on p through the first step at rate k_{GE} and through the last step at rates $k_{\mathrm{M}\pm\mathrm{G}}$; hence the corresponding bunching rate should increase with p. Based on our observations, γ_3 is consistent with this process. In contrast, γ_2 does not vary significantly with p. To account

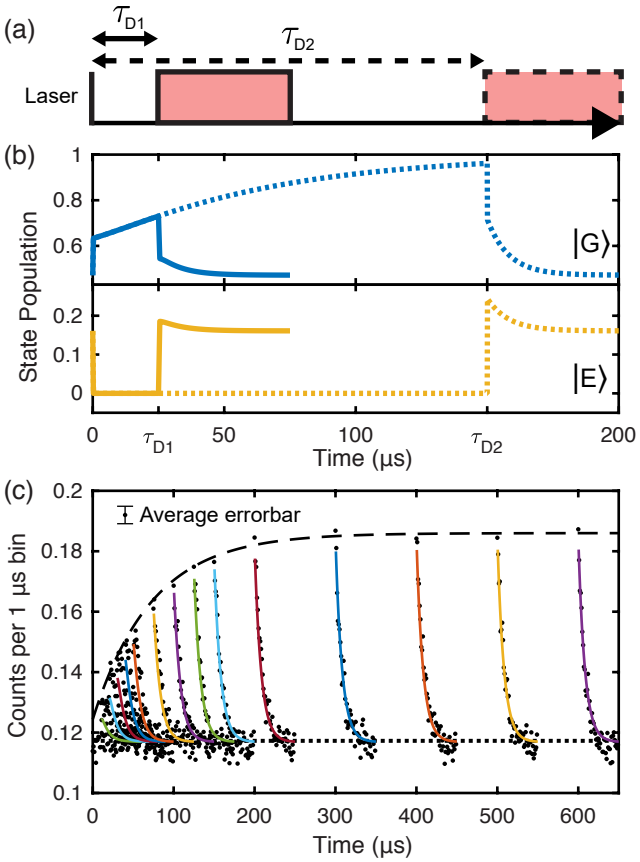

Figure 5.10: **Fluorescence recovery.** **(a)** Pulse protocol for time-domain fluorescence recovery measurement. **(b)** Example of time-domain ground (blue lines) and excited (yellow lines) state populations during a fluorescence recovery experiment for short (τ_{D1}) and long (τ_{D2}) dark times between laser pulses, shown as solid and dashed lines respectively. **(c)** Time-domain PL as a function of dark time between optical pulses, τ_D, acquired at 91 G in-plane magnetic field and 34.2° dipole orientation, using 1 μs time bins. Black dots are data and colored lines are simulation. The average uncertainty of each data point is ± 0.003 counts per bin.

for this unusual observation, we propose a fluctuating relaxation mechanism from $|E\rangle$ to $|G\rangle$ that stochastically switches between radiative and non-radiative configurations at rates k_{DB} and k_{BD} through a process independent of p. This is potentially due to fluctuations in the state of a nearby coupled defect that modulates the emission process. As shown by the simulations in Fig. 5.8(e), this process leads to bunching in $g^{(2)}(\tau)$ at a nearly constant rate $\gamma_2 \sim k_{DB} + k_{BD}$, which closely matches the experimental observations.

While γ_3 as derived from PECS yields estimates for the overall rates connecting $|E\rangle$, $|M_{1,2}\rangle$, and $|G\rangle$,

unlike γ_1 and γ_2, an approximate expression for γ_3 in terms of transition rates is not straightforward to derive. Therefore, additional measurements are required to resolve the contributions of each individual rate. The fluorescence recovery protocol (Fig. 5.10(a)) involves varying the dark time, τ_{D}, between laser pulses and recording the time-domain PL emission during each pulse. Figure 5.10(b) illustrates the evolution of populations in $|\mathrm{G}\rangle$ and $|\mathrm{E}\rangle$ during a fluorescence recovery experiment for two different values of τ_{D}. The measured PL (shown in Fig. 5.10(c) for 15 different values of τ_{D}) is proportional to the population in $|\mathrm{E}\rangle$, which depends in turn on the population in $|\mathrm{G}\rangle$ at the beginning of the laser pulse. The PL at the start of the laser pulse (dashed line in Fig. 5.10(c)) increases as a function of τ_{D}, with an extracted time constant of 73 ± 5 µs. This time constant directly reflects the p-independent components of $k_{\mathrm{M-G}}$ and $k_{\mathrm{M_1G}}$. During the laser pulse, the PL decays to a steady-state value with a decay constant of 7.9 ± 0.4 µs. The decay constant reflects the p-dependent $k_{\mathrm{M-G}}$ and $k_{\mathrm{M_1G}}$ in addition to $k_{\mathrm{EM_2}}$, $k_{\mathrm{EM_1}}$, k_{BD}, and k_{DB}. The maximum contrast from the initial to the steady-state PL, measured to be $62.2 \pm 0.2\%$, constrains the ratio $(k_{\mathrm{M_1G}} + k_{\mathrm{M_2G}})/(k_{\mathrm{EM_2}} + k_{\mathrm{EM_1}})$.

5.4. Simulations

We use a rate equation model for the level configuration shown in Fig. 5.8(a) to numerically simulate the state populations for PECS and the fluorescence recovery pulse protocol. The PECS simulations follow the framework outlined in Sec. 3.4.1 with the initial condition as the state of the system immediately following the release of a photon, $P_{|G\rangle}(0) = 1$. For the fluorescence recovery and spin contrast experiments, the simulations use a similar framework as the PECS simulations. However, the initial condition is the steady-state, which is calculated by numerically solving the steady-state equation,

$$0 = GP. \tag{5.4}$$

For the fluorescence recovery and spin contrast experiments, we simulate optical and microwave pulses by modifying the corresponding affected rates in the transition rate matrix, G. For pulse sequences that involve turning the laser off, we set the optical excitation rate to zero, $k_{GE} = 0$ and we set the pumped metastable decay rate, k_{MG} to be equal to its spontaneous component only.

When the laser is turned on, those rates are returned to their original values. For protocols that involve turning microwaves on, we set the rate between the two metastable spin states based on the Rabi frequency, and restore that rate to T_1^{-1} when microwaves are turned off. In order to simulate experiments with multiple pulses, we start the population distribution at the experiment's initial condition (specified above), and solve Eq. S3.17 according to the length of the first part of the sequence. We record the interim population distributions at the end of each pulse to be carried over as the initial conditions for the start of the next part of the sequence. For each simulation, we track the time-dependent excited state population to capture relative changes in time-dependent PL.

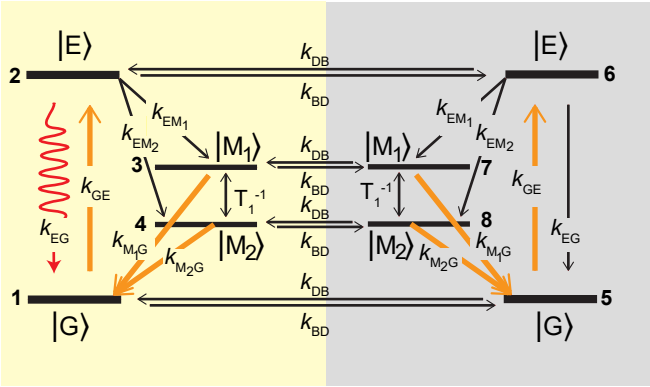

Figure 5.11: **Optical Dynamics Model for Simulation.** Eight-level model used in simulations to capture modulation of the emission mechanism between a radiative (yellow box) and non-radiative (grey box) configuration. Each configuration contains a singlet ground and excited state, and a metastable doublet. Black arrows depict non-radiative power-independent transitions, orange arrows depict excitation-power-dependent transitions, and the red wiggly arrow depicts the radiative transition.

Our model shown in Fig. 5.8(a) contains four energy levels and an emission modulation mechanism. In order to simulate this model, we index the energy levels by $i = 1$, 2, 3, or 4, and we index the emission mechanism by $j = 1$ or 2. We represent these eight unique state combinations using an eight-level model shown in Fig. 5.11 with each state labeled 1-8. The model features two manifolds, one with a radiative emission mechanism ($j = 1$) and the other with a non-radiative emission mechanism ($j = 2$). The emission modulation dynamics are captured in the simulation by the ability to switch between the two manifolds at any time at rates k_{DB} and k_{BD}. Each manifold has identical electronic states ($i = 1 - 4$) and optical dynamics to ensure that the state evolution is independent of the emission modulation. Time-dependent PL is assumed to be proportional to

the time-dependent excited-state population in the radiative manifold. Therefore, the fluorescence recovery simulation is normalized by the simulated steady-state excited state population in the j=1 manifold and by the experimentally observed steady-state PL.

In order to separate the system's overall optical dynamics from its features that determine spin polarization, we parameterize the metastable transition rates as overall rates and spin branching ratios. The transition rates from the excited to metastable states ($k_{\mathrm{EM}_\pm}$) are parameterized as the total excited-to-metastable transition rate, $k_{\mathrm{EM}} \equiv k_{\mathrm{EM}_2} + k_{\mathrm{EM}_1}$, with branching ratio $k_{\mathrm{EM}_1}/k_{\mathrm{EM}_2}$. The transition rates from the metastable states to the ground state ($k_{\mathrm{M}_\pm\mathrm{G}}$) are parameterized as the average metastable-to-ground transition rate, $k_{\mathrm{MG}} \equiv (k_{\mathrm{M}_1\mathrm{G}} + k_{\mathrm{M}_2\mathrm{G}})/2$, with branching ratio $k_{\mathrm{M}_1\mathrm{G}}/k_{\mathrm{M}_2\mathrm{G}}$.

The parameters k_{EG} and k_{GE} are known based on earlier considerations, as is the sum $k_{\mathrm{DB}} + k_{\mathrm{BD}}$. To quantify the remaining transition rates between each electronic state in our model, Fig. 5.11, we empirically match simulations of PECS rates and bunching coefficients, spin contrast, and fluorescence recovery PL to the data, starting with the fluorescence recovery. When simulating the fluorescence recovery experiment,(Fig. 5.10(a)), we consider three features observed in Fig. 5.10(c). The first feature we consider is the time constant that describes the increase in maximum PL at the start of the laser pulse as a function of τ_{D} (dashed line in Fig. 5.10(c)). This time constant is determined by the branching ratio $k_{\mathrm{M}_1\mathrm{G}}/k_{\mathrm{M}_2\mathrm{G}}$ and the p-independent component of k_{MG}. We simulate and fit fluorescence recovery, varying those two parameters to find combinations of $k_{\mathrm{M}_1\mathrm{G}}/k_{\mathrm{M}_2\mathrm{G}}$ and k_{MG} that give the correct time constant. Next, we consider the maximum contrast from the initial to the steady-state PL, which depends on the ratio, $k_{\mathrm{MG}}/k_{\mathrm{EM}}$. We simulate fluorescence recovery, varying k_{MG} and k_{EM} to find which ratio gives the correct contrast. Finally, we consider the decay time from maximum to steady-state PL during the laser pulse. This decay time is dependent on many rates. However, taking into account the constraints generated by the first two simulation steps, we can simulate this decay to steady-state in the regime that gives the correct maximum contrast and time constant to empirically determine a value for k_{EM}. We draw upon constraints from PECS data (as described prevoiusly) and make use of PECS and spin contrast simulations to

gain further clarity on any remaining parameters such as fluorescence modulation rates (k_{BD} and k_{DB}) and the branching ratio $k_{\mathrm{EM}_1}/k_{\mathrm{EM}_2}$.

Simulations of the resulting transition rates that were found to provide the best emipircal match to the data are shown as squares in Fig. 5.8(c-e)) and Fig. 5.12 for the PECS rates and bunching amplitudes respectively. Slight discrepancies between the PECS simulations and data are attributed to variations of the spin-dependent rates through $|\mathrm{M}_{1,2}\rangle$ due to different applied magnetic fields for the PECS (no field) and fluorescence recovery (91 G) experiments. The results of the fluorescence PL recovery simulations using these same transition rates are shown as colored lines in Fig. 5.10(c). The simulated fluorescence recovery time constants match those extracted from the data within fit errors, and the maximum contrast matches within 5%. The optimized rates are as follows: $k_{\mathrm{EM}} \equiv k_{\mathrm{EM}_2} + k_{\mathrm{EM}_1} = 0.19$ MHz, $k_{\mathrm{EM}_1}/k_{\mathrm{EM}_2} = 0.1$, $k_{\mathrm{MG}} \equiv (k_{\mathrm{M}_1\mathrm{G}} + k_{\mathrm{M}_2\mathrm{G}})/2 = 0.034$ MHz + $(0.8\ \frac{\mathrm{MHz}}{\mathrm{mW}})p$, $k_{\mathrm{M}_1\mathrm{G}}/k_{\mathrm{M}_2\mathrm{G}} = 8$, $k_{\mathrm{BD}} = 0.15$ MHz, and $k_{\mathrm{DB}} = 0.55$ MHz. The power-independent k_{MG} component sets an upper limit of ∼30 µs on the useful lifetime of the metastable spin.

In order to model the ODMR experiments, we use the Lindblad framework to capture coherent evolution of the spin states along with semiclassical optical dynamics [26]. Our experiments indicate a variation of the ODMR contrast and linewidth as a function of microwave power, p_{MW} (Fig. 5.13(a)). We fit Lindblad simulations to these data, using the optimized optical-dynamics rates as fixed parameters. Free parameters include the microwave coupling efficiency, η, which determines the power-dependent Rabi frequency according to $\Omega_{\mathrm{R}}/(2\pi) = \eta\sqrt{p_{\mathrm{MW}}}$, as well as the spin dephasing time, T_2^*. The fits are plotted along with the data in Fig. 5.13(a), and Fig. 5.13(b) compares the ODMR linewidth extracted from the data to the best-fit simulation. Accounting for uncertainties in the fit and in T_1, we find $\eta = 0.0189 \pm 0.0007$ MHz/$\sqrt{\mathrm{W}}$ and $T_2^* = 6.3 \pm 0.1$ ns.

5.5. Spin readout

Using the quantitative understanding of the emitter's optical dynamics that we have gained, we can design optimized protocols for spin initialization and readout. Spin polarization develops under optical illumination due to the spin-dependent branching ratios $k_{\mathrm{EM}_1}/k_{\mathrm{EM}_2}$ and $k_{\mathrm{M}_1\mathrm{G}}/k_{\mathrm{M}_2\mathrm{G}}$. Our model implies a steady-state population ratio $|\mathrm{M}_2\rangle$:$|\mathrm{M}_1\rangle \sim 30$:1 at $p = 350$ µW. The corresponding

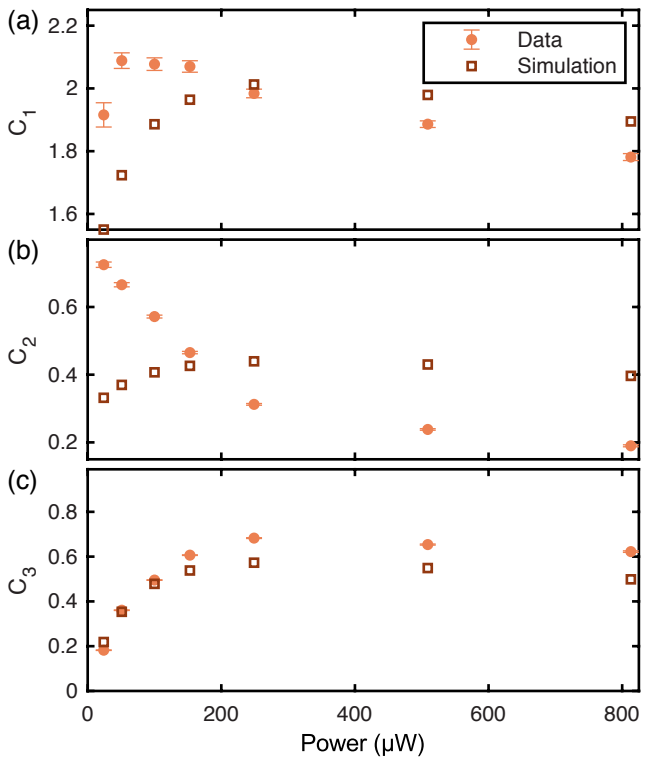

Figure 5.12: **Excitation-power-dependent bunching amplitudes with simulation results.** PECS bunching amplitudes as a function of excitation power for 0° dipole orientation and 0 G magnetic field. Bunching amplitudes and simulation results for the associated rates in Fig. 5.8(d-f) are shown here. (a) C_1, (b) C_2, and (c) C_3 are the bunching amplitudes for γ_1, γ_2, and γ_3 respectively. Error bars represent 68% confidence intervals. The fit gives a y-intercept of 128 ± 2 MHz and a slope of $0.125 \pm .005$ MHz/μW.

spin polarization $\sim$ 97 % significantly exceeds the steady-state polarization for other spin defects such as the diamond nitrogen-vacancy (NV) center. However, the population develops over $\sim$ 10 μs, which is an order of magnitude longer than typical NV-center initialization times [68].

In order to optimize spin readout, we record optical spin contrast using the pulse protocol shown in Fig. 5.8(b) at resonance frequency of 1308.5 MHz, $\sim$0° dipole orientation, and 592 nm excitation. The delay between signal and reference readout, τ_{D}, is the same as τ_{w} plus microwave pulse duration. For the data in Fig. 5.8(c), we set the initialization optical pulse to be 40 μs at 350 μW, setting wait time τ_{w} to be 20 μs and microwave pulse length to be 40 μs. Figure 5.8(c) shows a representative optical spin contrast obtained from measurement using this pulse protocol. The green highlighted region corresponds to an example of a readout window, τ_{R}, from which α_1 and α_0 are determined.

We record optical spin contrast curves, varying the optical power, the wait time, and the microwave pulse duration. From each optical spin contrast curve, we calculate SNR for τ_R in the range of 2 µs to 20 µs. Figure 5.14 presents the SNR for various readout times and all the optical powers, microwave pulse durations and wait times probed.

The single-shot SNR is given by [68]

$$\mathrm{SNR} = \frac{\alpha_1 - \alpha_0}{\sqrt{\alpha_1 + \alpha_0}}. \tag{5.5}$$

Here α_1 and α_0 are, respectively, the mean number of detected photons for the signal (microwave on) and reference (microwave off) recorded in a given readout window, τ_R (Fig. 5.8(c)). Figure 5.13(c) shows the SNR for 5 µs readout as a function of microwave pulse duration, for various settings of p. We find an optimum SNR ≈ 0.07 for $p = 350$ µW and $\tau_R = 5$ µs. Since the spin contrast experiment

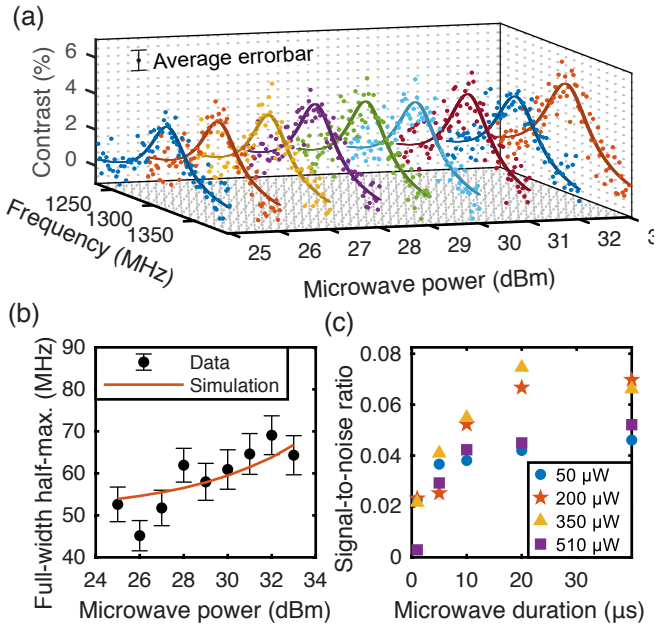

Figure 5.13: **Spin properties. (a)** ODMR contrast data with simulation fits (lines) as a function of microwave frequency and power. The average uncertainty of each data point is ±0.5% ODMR contrast. **(b)** Full-width half-maximum as a function of microwave power from Lorentzian fits of simulation and data. **(c)** Signal-to-noise ratio as a function of microwave pulse duration for readout time, $\tau_R = 5$ µs, at varying optical powers. All data are acquired at 592 nm excitation and 470 G magnetic field.

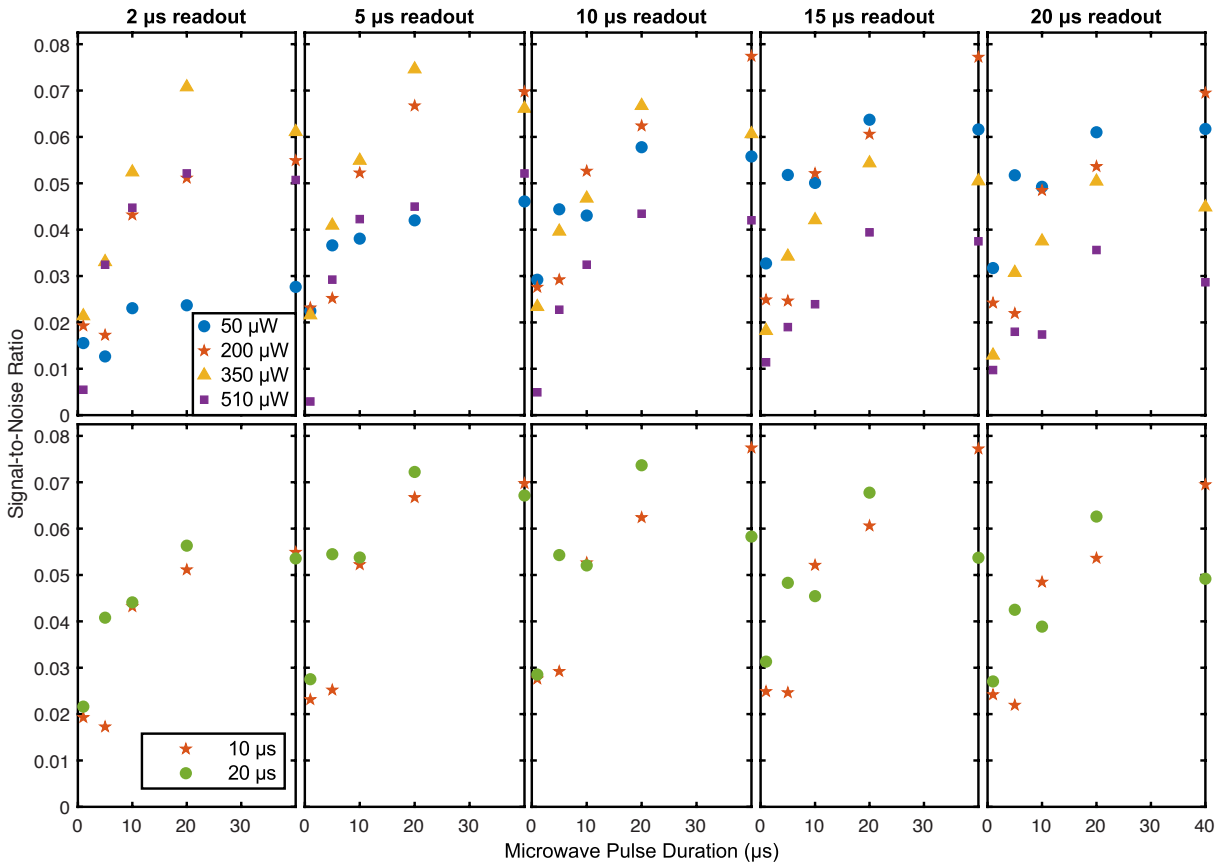

Figure 5.14: **Signal-to-Noise Ratio.** SNR determined from optical spin contrast measurements as a function of microwave pulse duration for different readout times for **(top row)** varying optical power (with $\tau_w = 10$ µs fixed) and **(bottom row)** varying wait time (with $p = 200$ µW fixed). Data was acquired at 592 nm optical excitation and 34 dBm microwave power.

in Fig. 5.8(b) compares the polarized spin configuration with a fully mixed state, the observed SNR is approximately half of what would be expected for a full spin inversion. For comparison, the optimized spin-readout SNR for a diamond NV-center with similar photon count rate is only ~ 0.03 [68]. The superior SNR is attributed to spin contrast persisting over an order of magnitude longer than in the NV-center, resulting in an SNR that is more than a factor of $\sqrt{10}$ greater for a full spin inversion.

5.6. Previous reports of single spins in h-BN

5.6.1. Similarities between reported works

Three significant reports have emerged in recent years on single spins in h-BN: Chejanovsky *et al.* [33], Stern *et al.* [127], and Guo *et al.* [58]. In all reports, ODMR was observed from multiple single-photon emitters in h-BN, and analysis focused on identifying chemical structures that could be consistent with observations. Thus far, similar features observed across all reports (as well as this one) include measured g-factors $\sim$2, a similar magnitude of zero-field splitting, and similar magnitudes of linewidths from ODMR measurements (See: Table 5.1).

	g-factor	ZFS	ODMR FWHM
Chejanovsky *et al.* [33]	$\sim$2	$<$10 MHz	25-36 MHz
Stern *et al.* [127]	$\sim$2	$<$25 MHz	$\sim$35 MHz
Guo *et al.* [58]	2.01 $\pm$ 0.01	-	22-52 MHz
Results in this work	$\sim$2	9$\pm$10 MHz	45-69 MHz

Table 5.1: **Consistent findings in recent works.**

However, some differences have emerged between this report and previous ones with regard to the presence of zero-field splitting (ZFS), spin structure of proposed models, and reported spin relaxation times. In the following sections, we discuss these differences. We find that some can be attributed to different interpretations of consistent data whereas others are due to differences in experimental approaches. Ultimately, we determine that the findings and model proposed in this text can be found to be consistent with previous reports.

5.6.2. Interpretation of zero-field splitting

The largest statistical report of single spins in h-BN comes from Stern *et al.* who have reported on the results of measurements from 27 ODMR-active defects. The authors fit ODMR curves to both single and double Lorentzians and observe a sub-linewidth ODMR doublet structure in 80% of the spin defects studied [127]. They propose that this splitting can be due to hyperfine coupling or zero-field splitting and determine zero-field splitting to be the more likely of the two. Through this analysis, they propose zero-field splitting on the order of 25 MHz as a part of an S = 1 system [127]. In contrast, in this report, we propose that our findings are consistent with an absence of zero-field splitting and an S = 1/2 system.

In order to determine whether these differences arise from the data or its interpretation, we fit our ODMR data from Fig. 5.1(e) to a double Gaussian,

$$y(x) = ae^{-(x-R_1)^2/\sigma^2} + be^{-(x-R_2)^2/\sigma^2} + c, \tag{S6}$$

and look for sub-linewidth structure. The results are shown in Fig. 5.15 and Table 5.2. We find that the reduced chi-squared statistic and AIC analysis favor the single Gaussian model,

$$y(x) = ae^{-(x-R_1)^2/\sigma^2} + c, \tag{S7}$$

as the more likely model to describe the ODMR data. However, the double Gaussian fit, though less likely, is still a possible fit. The double Gaussian fit shows a separation of 23 ± 2 MHz between the two resonances. This is consistent with reports from Stern *et al.* who find sub-linewidth splittings from 19 - 50 MHz [127].

Model	R_1 (MHz)	R_2 (MHz)	σ (MHz)	χ^2_{R}	AIC
Eq. S5.7	1316.3 ± 0.7	-	33 ± 1	1.037	-437
Eq. S5.6	1303 ± 1	1326.4 ± 0.9	27 ± 1	1.051	-433

Table 5.2: **Parameters from Gaussian fit to ODMR data.**

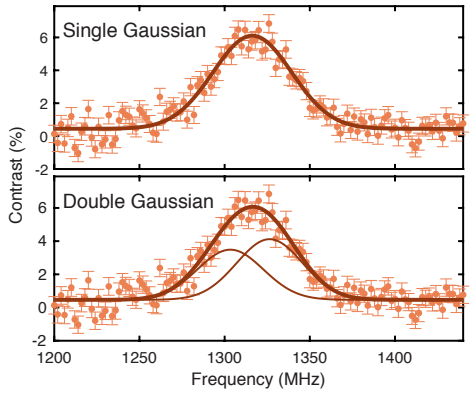

Figure 5.15: **Gaussian fits to ODMR data.** Top panel shows single Gaussian fit of ODMR peak and lower panel shows double Gaussian fit of ODMR peak with component peaks also shown as thinner lines.

Therefore, the difference in proposed models arises from the interpretation of these findings. The possible mechansims behind the sub-linewidth structure, hyperfine coupling and zero-field splitting, each present their own problems. While hyperfine coupling provides splittings of the correct order of magnitude, Stern *et al.* explored several models and did not find one which produced results consistent with the observed hyperfine coupling. On the other hand, zero-field splitting is typically observed on the order of GHz. As Stern *et al.* acknowledge, a zero-field splitting of 25 MHz, requires a 10 lattice site separation between electron clouds [127, 48]. This separation would only increase for the smaller zero-field splittings observed in Chejanovsky *et al.* and this report (Table 5.1). While such a separation is possible, it is unlikely, especially given that the chemical structure of these spin defects in h-BN have yet to be conclusively identified. Therefore, given that we measure zero-field splitting consistent with zero within uncertainties, our proposed interpretation of no zero-field splitting with the ODMR splitting attributed to hyperfine coupling can be still be found consistent with past reports.

5.6.3. Proposed spin structure

Another difference between reports are the proposed spin configurations that give rise to the observed ODMR. While Stern *et al.* propose an S = 1 model with S = 3/2 as an alternative possibility [127], Chejanovsky *et al.* and Guo *et al.* consider S = 1/2 models [33, 58], with Chejanovsky *et al.* noting that their data could indicate a non-integer-spin ground state [33]. Notably, our proposed model and

its ability to capture the observed optical dynamics is not inconsistent with higher spin levels. In the case of an S = 1 model, it would be straightforward to label M_1 and M_2 in Fig. 5.8 as $m_s = \pm 1$ and $m_s = 0$, and the resulting optical dynamics would still be consistent with those observed in Figs. 5.8 and 5.10. However, in such a case, we would expect to also observe zero-field splitting. Similarly is is possible replicate the observed optical dynamics with an S = 3/2 state, though this would require a more complex model with additional energy levels. Importantly, a configuration with an S = 1/2 to S = 3/2 transition, would not give rise to spin polarization from spin-orbit coupling in a low-symmetry defect like h-BN [48], so another mechanism would be required to observe ODMR if this were the case. Therefore, we conclude that while our optical dynamics can be explained by other, higher-level models, an S = 1/2 model remains the simplest and most likely explanation in this case.

5.6.4. Spin timescales

Finally, we discuss the difference stated values of T_1, the spin relaxation time, between this report and previous reports. Chejanovsky *et al.* and Guo *et al.* state similar values for T_1, ranging from 13 - 17 µs [33, 58]. This is in contrast to our proposed lower-limit on T_1 of $\sim$ 100 µs, which is an order of magnitude greater. While the differences in spin relaxation times could be explained by different defects, some insight into the discrepancy can also be gained by examining the different approaches each work takes to determine T1.

The T_1 pulse protocol presented by Guo *et al* shows an initialization and readout laser pulse separated by a microwave pi pulse and a variable wait time (τ) [58]. The authors extract their value of T_1 from the resulting PL as a function of τ. While spin relaxation is one of the processes that occurs during the wait time, the overall population decay to the ground state is another significant process that results in an increase in the readout PL as a function of τ (See: Fig. 5.10). Without accounting for this fluorescence recovery, for example by normalizing the results by a similar experiment in the absence of the microwave pulse, it is difficult to separate the contribution of spin relaxation from that of metastable state decay. Therefore the increase in PL cannot be attributed to spin relaxation alone. The quoted T_1 time of 16 µs in Guo *et al.* is likely a combination of the spin relaxation time

and the metastable state relaxation and only sets a lower limit on the spin relaxation time.

In this work, we use simulations to determine T_1 must be longer than the metastable state relaxation time in order to achieve the contrast we observe in time domain microwave experiments. Our effective spin relaxation time of 30 µs that comes from the metastable decay is not too far off from 16 µs, and this difference could be due to local coupled defects. A difference in T_1 times can also be indicative of the spin state configuration. In this work, we propose a spin doublet in the metastable manifold, which could lead to more isolation from the environment and thus longer T_1 times than a case where spin states are in the ground state. In the case of Chejanovsky *et al.*, who measured T_1 at low temperature, the differing T_1 values could be attributed to temperature-dependence of T_1, which the authors note may be significant [33].

5.7. Conclusion

The quantitative model presented in this work will directly facilitate the use of single spins in h-BN for quantum technologies. The inferred spin polarization of $\sim 97\%$ and spin-readout SNR of ~ 0.15 are superior to the performance of well-established room-temperature spin qubits, including NV centers. More sophisticated initialization and readout protocols could offer further improvements [68]. The spin relaxation time, $T_1 \approx 100$ µs, is comparable to the spin lifetimes of NV centers in nanodiamonds. The effective spin lifetime of ~ 30 µs offers opportunities for relaxometry imaging and chemical sensing, and the metastable spin can potentially be used as an ancilla to a nuclear spin. In contrast to most spin qubits, which feature spin levels in the ground and optically excited states, the spinless ground state configuration of this system can be beneficial to protect the coherence of nuclear spin states [84]. The relatively short dephasing time, $T_2^* = 6.3 \pm 0.1$ ns, likely reflects substantial hyperfine coupling to nearby nuclear spins. Hence, with the design of optimized microwave antennas to drive faster spin rotations, it will be possible to use dynamical decoupling protocols to substantially extend the electron-spin coherence time, and to address the states of coupled nuclear spins.

The chemical structure of h-BN's visible emitters remains a mystery. Conclusive identification is needed to enable the further optimization of materials, devices, and quantum control protocols. The

detailed empirical understanding of their energy-level structure and dynamics developed through this work will inform and constrain future theoretical models. More generally, the framework followed in this chapter can be used to characterize and control the optical and spin dynamics of single spins in any solid-state host material.

CHAPTER 6

CONCLUSION

Quantum technologies rely on the operation of systems that are inherently sensitive and challenging to work with. As a result, it is imperative to understand the wide range of properties that can affect a quantum emitter's suitability for applications. In particular, a quantum emitter's optical dynamics play an important role in harnessing the control of quantum states for specific applications. In this thesis, I explore the considerations for qubit candidates through the case of three systems: zinc sulfide, quantum emitters in hexagonal boron nitride, and diamond nitrogen-vacancy centers. I present a guide for the specific application of photon emission correlation spectroscopy (PECS) to study the optical dynamics of quantum defects, discussing considerations and tools for acquisition, analysis, simulation, and interpretation of PECS. Through studies of an NV center in diamond and a single spin in h-BN, I demonstrate the application of PECS paired with simulations to gain insights into each system's optical dynamics. This thesis includes material adapted from a manuscript published in *PRX Quantum* [51], a manuscript in review [102], and work currently in preparation.

It is important to recognize and the advantages and disadvantages that the material properties, defect properties, and material morphology of a quantum defect system provide. While ZnS is a promising material host for quantum emitters due to its medium spin-orbit coupling and low istopic concentration, exploration of its emitter's optical properties have not yet yielded a system whose quantum state can be manipulated and read out. On the opposite end of the spectrum, a multitude of studies have focused on the NV center. Its optical properties enable spin initialization and readout, yet other optical properties such as its broad emission linewidth present limitations. Somewhere in the middle is h-BN, whose morphology provides opportunities for fabrication and engineering and whose defects can host optically-addressable single spins, but their chemical structure and origin remain unknown.

Progress continues to be made toward a greater understanding of all three of these systems. While

ZnS remains in the early stages of materials exploration, efforts toward synthesis and isolation of ZnS nanoparticles are underway [138]. A focus on quantum defect creation and stabilization in 0D and 3D ZnS systems provides a way forward toward the discovery and study of quantum defects in ZnS. After decades of focus on the NV center's negatively-charged manifold, further exploration of NV^0 promises enhanced quantum control protocols that harness an understanding of the interplay between spin and charge dynamics. Studies of the NV^+ charge manifold, a less common charge-configuration for the NV center, can also yield advantages [104]. Finally, research on h-BN emitters is at an exciting point with the pivotal recent demonstrations of quantum control and readout of single spins in h-BN [102, 33, 127, 58]. As with the NV center, a emerging understanding of the optical dynamics and structure of these h-BN spin defects will enable the implementation of quantum control protocols in h-BN.

As the application of PECS to study solid-state quantum emitters expands beyond confirmation of single-photon emission, understanding the range of its use can play an important role in materials exploration. While PECS is an easy-to-implement experimental technique, it remains under-utilized for solid-state quantum emitters. Although standard optical characterization techniques provide information about radiative transitions, the non-radiative transitions, which PECS is particularly suited to resolve, are often those whose properties are leveraged for various quantum technologies. With proper attention to acquisition, analysis, and interpretation, PECS can provide detailed information about a quantum emitter's electronic structure and dynamics that allows for the design of efficient quantum control protocols.

Proposals for a more efficient approach to materials exploration [15] combined with an informed application of PECS will expand the set of available quantum emitters and host materials - each with specific advantages - and lead to the development of improved quantum control protocols for systems that are already established. Intentional application of PECS supplemented with other experimental and theoretical techniques will paint a more complete picture of a quantum emitter. Classic spectroscopic techniques can provide information on the electronic structure, while *ab inito* energy calculations and molecular orbital theory can inform and confirm it. PECS and time-domain

experiments can probe the dynamics of particular processes and isolated transition rates. While PECS simulation and *ab initio* transition rate calculations can confirm consistency of hypothesized models. As a tool that has accompanied so many breakthroughs in quantum science, it is only fitting that the adaptation of PECS for solid-state emitters will enable advances in quantum protocols and the exploration of new platforms for technologies, continuing to progress the quantum revolution.

APPENDIX A

ALGORITHM FOR PROCESSING PHOTON CORRELATIONS

The time-tagged data acquired by two detectors and a time correlated single-photon counter (TCSPC) consists of two separate time series detailing the arrival times of all photons detected by each detector during acquisition. Photon statistics processing code and example can be found at https://github.com/penn-qel/photon-emission-correlation-spectroscopy. The processing algorithm `TTTR_cross_correlation(parsedData,options)` based on *Laurence et al.* [83], uses the input of two time series along with various processing parameters to calculate the normalized correlations and their uncertainties. The algorithm uses binary search functions defined within it to bin and count correlations thus avoiding the need to iterate through all individual events and significantly reducing processing time. Additional features include processing of average count rates to track stability during measurement and an option for partitions to process correlations between different blinking states separately.

A.0.1. Preparing the data

Certain TCSPCs store photon time series in particular file formats, which must be parsed before running the processing algorithm. The function `TTTR_import_PTU(filenames)` takes time series stored in a .ptu file format and stores the data and metadata as a MATLAB structure, `TTTRData`, which is then fed to the function `TTTR_extract_channel_times(TTTRData,options)` to convert the .ptu data into a MATLAB array of times. These are output into the `parsedData` structure containing the times and total number of counts for each channel, global resolution, and total acquisition time.

A.0.2. Defining processing parameters

The `options` structure allows the user to define processing parameters. These set the range (`tauLimits`) and resolution (`tauRes`) over which the correlations will be calculated. Resolution should be chosen such that it is smaller than the fastest timescale desired for measurement. Since decreasing resolution also increases uncertainties, which are Poissonian and depend on the number

of counts per bin, scans that require lower resolution may require greater acquisition time. The choice of resolution and limits also affect the processing time, so a balance must be struck between resolution, magnitude of uncertainties, and processing time.

Additional parameters in the options structure include `tRes` to specify the resolution for count rates calculations, `tauAxis` to choose specific axis over which cross-correlation will be calculated, `countRateRanges` to partition blinking data based on intensity, `tFlag` to partition the time axis for counts rate calculation, and `verbose` and `statusbar` to enable command window and pop-up updates.

A.0.3. Algorithm Detail

The algorithm first constructs two time axes, `tauAxis` and `tAxis`, defining the bins over which the correlations and average counts rates will be calculated respectively. The delay time axis, `tauAxis`, is constructed from the processing parameters defined in the options structure. `tAxis` is constructed based on the total acquisition time and resolution, `tRes`. Count rates in each channel are calculated by counting the number of events in each bin that `tAxis` defines and dividing by bin width. The overall count rate for each channel, `avgRate`, is calculated from the channel's total counts and total measurement time in order to compute the normalization factor for $g^{(2)}(\tau)$. (See Sec. 3.3.2).

To process the cross correlations between the two channels, the algorithm iterates through each time-tagged photon event in the channel with fewer events, referred to as Channel 1. With each iteration, the zero-delay reference point for the bins defined by `tauAxis` is updated according to the time of the current photon event, t_0. Then, events in Channel 2 are binned according to `tauAxis`, with $\tau = 0$ corresponding to t_0, and the number of photons that fall within each bin in Channel 2 are counted as the correlations.

A.0.4. Outputs

The processing algorithm outputs a structure, `T2data`, that contains the axis of delay times, raw correlated data, normalized $g^{(2)}(\tau)$, and errors. If count rates are calculated, the output structure will also include the time axis for count rates, the average count rates over acquisition time, and flags

for partitioning the time axis. Figure 3.3 contains examples of processing code outputs along with a demonstration of several features of the code including log and linear binning options, calculation of count rates, and separate processing of different blinking states.

APPENDIX B

AKAIKE INFORMATION CRITERION

When analyzing experimental data for newer or unknown emitters, the electronic level structure and dynamics of the emitter are often unknown. As a result, a fitting routine often must be implemented to determine which empirical model best fits the data and its features. The Aikaike Information Criterion (AIC) can be used as a measure of relative quality to identify a model that captures the dynamics comparatively best. In order to implement it, the data is fit to several models of Eq. 3.39, varying n, the number of electronic levels. The AIC is given by

$$\mathrm{AIC} = 2p - 2\ln(L). \tag{B.1}$$

For a nonlinear fit with normally distributed errors,

$$\ln(L) = 0.5\left(-N\left(\ln(2\pi) + 1 - \ln(N)\ln\left(\sum_{i=1}^{n} x_i^2\right)\right)\right), \tag{B.2}$$

where N is the total number of data points and x_i^2 are the residuals.

In order to compare models, the AIC for each model is calculated and compared. The model with the lowest AIC representing the model most likely to be correct, while the relative likelihood for the other models can be calculated as

$$\exp\left(\frac{\mathrm{AIC}_{\min} - \mathrm{AIC}_i}{2}\right). \tag{B.3}$$

AIC can be supplemented with other measures of fit such as reduced chi-squared to empirically determine the best choice of n.

APPENDIX C

OPTICAL-DYNAMICS SIMULATION

The optical dynamics simulation `simulate_autocorrelation(ModelPars,SimPars,Opts)`, takes the input of an electronic model defined by states, the transition rates between them, and the photon collection efficiencies of the transitions and returns the populations of each state given an initial condition. Optical dynamics such as the photon statistics and photoluminescence are also calculated. The simulation is executed through MATLAB's ODE solver `ode15s`. Simulation code and example can be found at https://github.com/penn-qel/photon-emission-correlation-spectroscopy.

C.0.1. Defining the model

The electronic model is defined through three inputs: The number of levels (`nLevels`), the transition rates between levels (G), and the collection efficiency matrix (C) all of which are passed to the function through the `ModelPars` or `SimPars` structure. The transition rate matrix, G, defines the transition rates between levels for a single experimental condition at a fixed excitation power and a fixed magnetic field. G takes the form of an nLevels x nLevels matrix with off-diagonal elements G_{ij} giving the transition rates from state $|j\rangle$ to state $|i\rangle$, and diagonal elements G_{ii} giving the negative sum of all rates leaving state $|i\rangle$. The columns of G all sum to 0. The collection efficiency matrix, C, is an nLevels x nLevels matrix with elements $0 \leq C_{ij} \leq 1$ denoting the fractional probability of collecting photons from the transition from state $|j\rangle$ to state $|i\rangle$. A non-radiative transition would be denoted by $C_{ij} = 0$ while a radiative transition would have $C_{ij} = \epsilon$ where ϵ is the collection efficiency from that transition.

C.0.2. Simulation Detail

The steady-state populations are calculated from G using MATLAB's `null()` function and normalized such that the sum of all steady-state populations is 1. PL is calculated from the steady-state populations and C matrix (see Eq. 3.41). The eigenrates of G are calculated through the MATLAB function `eig()` and ordered and identified as real or imaginary rates. The min and max eigenrates are used to determine a range of the time values (t) to input to the ODE solver. The initial con-

ditions are set according to Eq. 3.21. The ODE solver `ode15s` is run using the inputs of the rate equation, transition rate matrix, and initial conditions. A comparison between the steady-state populations calculated through the null vector and through the ODE solver can be used as an estimate of simulation error, p_{err}.

C.0.3. Simulation Outputs

The steady-state populations, steady-state PL, eigenvalues of G, time-dependent populations of states, and vectors of $g^{(2)}$ and t are all returned in the `SimPars` structure.

C.0.4. Additional complexity

Multiple simulations can be executed by feeding multiple pairs of G and C matrices defining different models or model conditions to the `SimPars` structure. The number of elements in `SimPars` determines the number of simulations that will be run. Transition rates dependent on physical interactions with fields such as spin or charge phenomena can be defined prior to execution of the simulation such that the model incorporates additional phenomena. The transition rates between states can be defined as spin states that are dependent on an applied magnetic field, B. This takes the form of defining the spin-field interaction through the Hamiltonian, and calculating how an applied field leads to a change of basis, represented by a change transition rates from spin-dependent states.

APPENDIX D

QUANTUM EMITTER SEARCH THROUGH ANALYSIS OF PHOTOLUMINESCENCE IMAGES

The method presented in this appendix provides a general, flexible framework for efficiently screening new materials for SPE. Compared to manual searching, the ability to detect and classify individual fluorescent emitters through quick image processing greatly improves the speed of exploratory experiments.

Image Analysis

The method we describe is related to established spectroscopic techniques such as single particle tracking [88] and super-resolution microscopy [115], which fit emitters with a Gaussian function. To start, 2D photoluminescence images are converted into binary images using an adaptive background threshold. The binary image is constructed by setting all pixels above or equal to the threshold to 1, while all pixels that are less than the threshold are set to 0. As opposed to a universal threshold, an adaptive threshold accounts for spatial variation in background intensity by calculating the local mean intensity for each pixel of the PL image [25]. Using the binary image, interconnected foreground pixels that share at least an edge or corner are identified as individual objects. Overlapping emitters are separated by local maximum detection using the PL image, and any objects smaller than the diffraction-limited spot-size are discarded. Using object center positions from the binary image, each object is cropped from the full PL image into at least 15 by 15 pixel regions of interest (ROI). For larger objects, the ROI is the smallest rectangular box that fully contains the emitter in the binary image. Each detected object within the ROI is assigned a 2D Gaussian function within a simultaneous fit for all emitters plus a constant background. The minimum ROI area of 15x15 pixels ensures sufficient degrees of freedom in the 2D Gaussian fit for calculation of the goodness-of-fit

parameter (introduced in the detection criteria section). The 2D symmetric Gaussian function is given by

$$I(x, y) = A \cdot \exp\left(-\frac{(x - x_0)^2 + (y - y_0)^2}{2\sigma^2}\right), \tag{D.1}$$

where A is the peak intensity of the emitter, (x_0, y_0) are the emitter coordinates, and σ is the emitter width, corresponding to the Gaussian standard deviation. The Gaussian fit provides the width, signal-to-noise ratio, and goodness-of-fit for each emitter, which serve as the primary detection criteria.

Detection Criteria

Width

Objects are filtered based on their best-fit Gaussian width. For a diffraction-limited point source, the expected width is

$$\sigma_{\text{diff}} = 0.21\frac{\lambda}{\text{NA}}, \tag{D.2}$$

where λ is the defect's emission wavelength and NA is the numerical aperture of the microscope objective [151]. If the emission wavelength is unknown, a width range can be estimated by substituting the microscope's detection range for λ. Typically, the detection range will be bound by the laser excitation wavelength and the the upper limit of the photon detector's range. In practice, optical aberrations or nonideal confocal conditions may distort the microscope's point spread function, increasing the apparent width. This adjustment can often be calibrated using a multiplicative factor determined by comparison between the Gaussian function and the microscope's point spread function, measured using a known sample with a bright, stable point source. We constrain the best-fit width to a range, $\sigma \in [\sigma_{\text{min}}, \sigma_{\text{max}}]$, where σ_{min} and σ_{max} are set based on estimates for the expected Gaussian width corresponding to the wavelength range of interest and adjustments based on the microscope's point spread function.

2D Gaussian Fit

The symmetric 2D Gaussian fit filters the detected objects according to their shape, selecting for Gaussian point sources over misshapen and extended objects. The width constraint from the

previous section is applied in this step as the range of allowed width for each peak in the fit. The emitter position is also tightly constrained to within 2 pixels of the weighted center of the detected object to ensure partially overlapping emitters are fit separately. We perform a least-squares regression fit where the free parameters include the position, width, and amplitude of each emitter plus a constant background. The goodness-of-fit parameter is defined as reduced chi-squared (χ_R^2), given by

$$\chi_R^2 = \frac{1}{\mathrm{DoF}} \sum_{i=1}^{N} \frac{(O_i - M_i)^2}{\sigma_i^2}, \tag{D.3}$$

in which M_i is the fitted counts, O_i is the measured counts, $\sigma_i = \sqrt{O_i}$ is the Poisson noise of the measured counts, and DoF is the number of degrees of freedom in the fit.

For an ideal fit with many degrees of freedom, χ_R^2 equal to one means the model fits the data within the expected variance, χ_R^2 less than one indicates the data is over-fitted by the model, and χ_R^2 greater than one indicates a poor fit or a model that does not fully capture the data. The statistical expectation for a good fit depends on DoF, with bounds at $\chi_R^2 = 1 \pm \sqrt{\frac{2}{\mathrm{DoF}}}$. For ROIs containing 15×15 pixels and one emitter, the expected χ_R^2 range based only on the degrees of freedom in the fit is 0.9 to 1.1. However, it is also necessary to account for sources of error in the confocal setup when setting the limits for χ_R^2. We have found that extending the allowed χ_R^2 values on an empirical basis to 0.8 and 1.5 ensures the Gaussian fit is robust against error in our confocal setup. The upper limit of 1.5 accounts for slight under-fitting due to the systematic error between our microscope's point spread function and the 2D Gaussian function. The lower limit of 0.8 reflects over-fitted emitters with low signal-to-noise ratio, which occurs when dim SPE are close to the background level. A χ_R^2 value less than 0.8 indicates objects that are usually background fluctuations and should be discarded. However, we find that a χ_R^2 value much greater than 1.5 is possible for bright SPE affected by blinking and uneven PL image background. These emitters appear Gaussian and symmetric by eye except for a small number of dark pixels. An uneven background or bright background object can also produce a large χ_R^2 value. Dim emitters are less affected by these factors due to their lower contrast with the background.

Without an alternative measure, these bright, blinking emitters would be excluded on the basis of their high χ_R^2 value. For materials with emitters frequently affected by these issues, we find that emitter shape — specifically, elliptical eccentricity — is an effective means to filter point sources from extended objects. The elliptical 2D Gaussian function is defined as

$$I(x,y) = A \cdot \exp\left(-\left(\frac{\cos^2\theta}{2\sigma_1^2} + \frac{\sin^2\theta}{2\sigma_2^2}\right)\tilde{x}^2 + 2\left(\frac{\sin^2 2\theta}{4\sigma_1^2} - \frac{\sin^2 2\theta}{4\sigma_2^2}\right)\tilde{x}\tilde{y} - \left(\frac{\sin^2\theta}{2\sigma_1^2} + \frac{\cos^2\theta}{2\sigma_2^2}\right)\tilde{y}^2\right), \tag{D.4}$$

where A is the peak intensity, $(\tilde{x}, \tilde{y}) = (x - x_0, y - y_0)$ are relative coordinates, σ_1 and σ_2 are the Gaussian widths of the elliptical axes, and θ is the rotation angle. The emitter eccentricity is defined as

$$e = \sqrt{1 - \left(\frac{\min[\sigma_1, \sigma_2]}{\max[\sigma_1, \sigma_2]}\right)^2}. \tag{D.5}$$

Possible eccentricity values range from 0 for a circle to 1 for a line. We set the allowed range of eccentricity for SPE detection to any value between 0 and 0.66, corresponding to at least a 3:4 ratio between the minor and major widths. For bright emitters in materials known to have uneven background and frequent blinking, eccentricity overrides χ_R^2 in classifying SPE. Because the elliptical Gaussian fit must be used in addition to the symmetric Gaussian fit, it doubles the computation time of the method and thus should be reserved only for materials with bright and unstable emitters.

Signal-to-Noise Ratio

The signal-to-noise ratio (SNR) is incorporated into the detection criteria to avoid the selection of dim, under-fitted emitters that are likely to be fluctuations in the background. The SNR is given by

$$\text{SNR} = \frac{A}{\sqrt{B}} \tag{D.6}$$

where A is the best-fit emitter intensity and B is the best-fit background value. The SNR depends on both the emitter brightness and the acquisition settings (particularly the dwell time per pixel). An alternative approach could use the signal-to-background ratio, which is less dependent on the acquisition settings, however we find that SNR is more robust in identifying SPE by incorporating both the emitter intensity and its statistical significance as an emitter defined above the background

Group A	Group B	Group C	Group D
SNR > 10 $0.8 < \chi^2_R < 1.5$ Width within limits	$2 <$ SNR < 10 $0.8 < \chi^2_R < 1.5$ Width within limits	$2 <$ SNR < 10 $0.8 < \chi^2_R < 1.5$ Width at limits	SNR > 10 $0 <$ e < 0.66 Width within limits
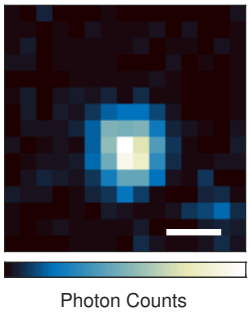	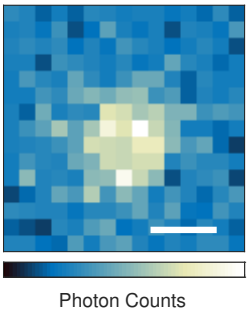	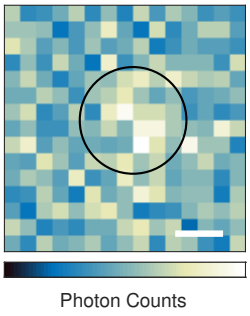	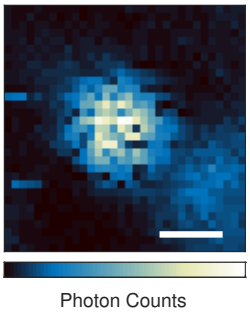
bright, stable	dim, stable	dim, blinking	bright, blinking

Table D.1: Emitter groups and representative SPE observed in PL images of nanodiamond and h-BN. Signal-to-noise ratio (SNR) describes the brightness of the emitter with respect to the noise of the background. Reduced chi squared (χ^2_R) is the goodness-of-fit parameter for the 2D Gaussian fit. The width refers to the Gaussian width calculated in the 2D Gaussian fit, while the limits are set according to the detection range of the confocal setup and the expected emission wavelength (if known). Eccentricity (e) is derived from the 2D elliptical Gaussian fit and replaces χ^2_R as a measure of symmetry for bright and blinking emitters. The PL image examples shown for A and D are SPE in h-BN, while those shown for C and B are SPE from the nanodiamond array. PL counts are normalized to the maximum intensity of each image. Scale bars are 0.5 µm.

level. We set a lower limit of SNR > 2 for emitter detection, and a threshold of SNR $= 10$ to divide bright (SNR > 10) and dim (SNR < 10) emitters.

Emitter Classification

The detection criteria described in the previous section define four groups of emitters exhibiting qualitatively different characteristics. **Table D.1** lists the SNR, χ^2_R, and width criteria corresponding to each emitter group, along with representative example images. All emitters classified in groups A-D are consistent with Gaussian point sources. The groups are designed to capture similar emitters, reflecting common factors that affect PL images of SPE like emitter instability and uneven background. Group A describes well-isolated, stable, bright objects, representing the ideal case for SPE discovery. Group B emitters are identical to group A, except they are dim. Group C describes emitters with a good Gaussian fit but unexpectedly large or small width, which often occurs for dim and blinking emitters. Group D captures well-sized and shaped emitters for which background

conditions or high frequency blinking significantly affect χ^2_R. By categorizing potential emitters in this manner, basic knowledge of the sample can direct further investigation into the most promising group.

Practical Use Considerations

When applying the method to a particular sample, the objective is to determine which group will be the best to prioritize for SPE search. Systems with stable, isolated, and high intensity emitters, including color centers in diamond and quantum dots, will tend to exhibit SPE in the stable and bright group A. For ion-implanted samples or fabricated nanoparticle arrays, defects are naturally clustered within diffraction-limited areas. Thus, SPE are more likely to be found in the dim C and B groups than the bright A and D groups. Samples of this type include the nanodiamond arrays, etched arrays of nanopillars [90] and nanopyramids [74], and ion-implanted arrays. A high occurrence of emitter blinking should guides user to implement the group D categorization based on shape, especially if there are very few emitters categorized as the bright and stable group A. H-BN is a prominent example of blinking emitters, but other examples include nanocrystals [23, 100] and certain quantum dots [38].

For lesser-known or entirely new samples, it is more difficult to predict the expected characteristics of SPE. However, basic knowledge of the sample can provide some guidance to prioritize autocorrelation measurements for certain groups. First, the user should determine the applicability of group D, as the elliptical Gaussian fit approximately doubles the time to apply the method. Group D should be used only if initial large-area PL images show a high frequency of blinking, or if the method discards most emitters with only groups A-C. Even if group D is engaged, group A emitters should probably take precedence for measurements because their stability and high signal-to-noise will enable shorter acquisition times. Group D emitters could be investigated next, since these emitters also exhibit high signal-to-noise ratios. However, if the user expects emitter overlap within the diffraction limit, the dim and stable group B should be prioritized for potential SPE instead of groups A or D. Group C should likely be investigated last, as dim and blinking emitters do not generally possess favorable properties for SPE. If many emitters are classified as group C, it may

be helpful to adjust the PL image dwell time, resolution, or laser power to improve the imaging of dim emitters. For samples with no expectation of overlapping emitters, the dim groups B and C will contain emitters that are close to the background and require long autocorrelation acquisition times.

APPENDIX E

DESIGN OF AN ULTRA-HIGH VACUUM CONFOCAL SETUP WITH A TUNABLE EXCITATION SOURCE

This appendix describes the design considerations for a confocal setup with a tunable excitation source where a sample is mounted in a ultra-high vacuum (UHV) cryostat. It includes special details regarding the design, construction, and operation of the customized system.

The system consists of a widely-tunable, continuous wave, narrow-linewidth, visible and near-infrared optical parametric oscillator for coherent photoexcitation spectroscopy and coherent quantum control and a closed-cycle optical cryostat providing an ultrahigh vacuum (UHV) sample environment, temperature control between 6 and 450 K, and a short optical working distance to facilitate diffraction-limited confocal fluorescence microscopy with sub-micron resolution.

This spectroscopy system is designed to probe quantum effects of individual defects in semiconductor nanomaterials under carefully controlled environments. The UHV environment is important for measurements of 2D materials like hBN because it limits surface adsorption that often degrades the quality of optical measurements at high vacuum. The cryostat also features a heating stage (up to 450K) that will allow for high temperature surface cleaning.

E.1. OPO laser

The optical parametric oscillator (OPO) laser system acquired is the tunable, continuous-wave C-WAVE model from Hübner Photonics (Fig. E.1). The C-WAVE uses OPO and second harmonic generation (SHG) technology to achieve tunable single-frequency output through automatic optimization of cavity temperature and length. The C-WAVE can output single-frequency laser light from 450 - 650nm within 1nm accuracy in the visible and 900-1300nm within 2nm in the infrared with a narrow spectral linewidth below 1MHz. The internal 1.5W pump laser provides power for up to >200mW output in the visible and >400mW in the IR. Once optimized for a specific wavelength, fine adjustments between 0.1-0.5nm can be achieved without the need for further optimization

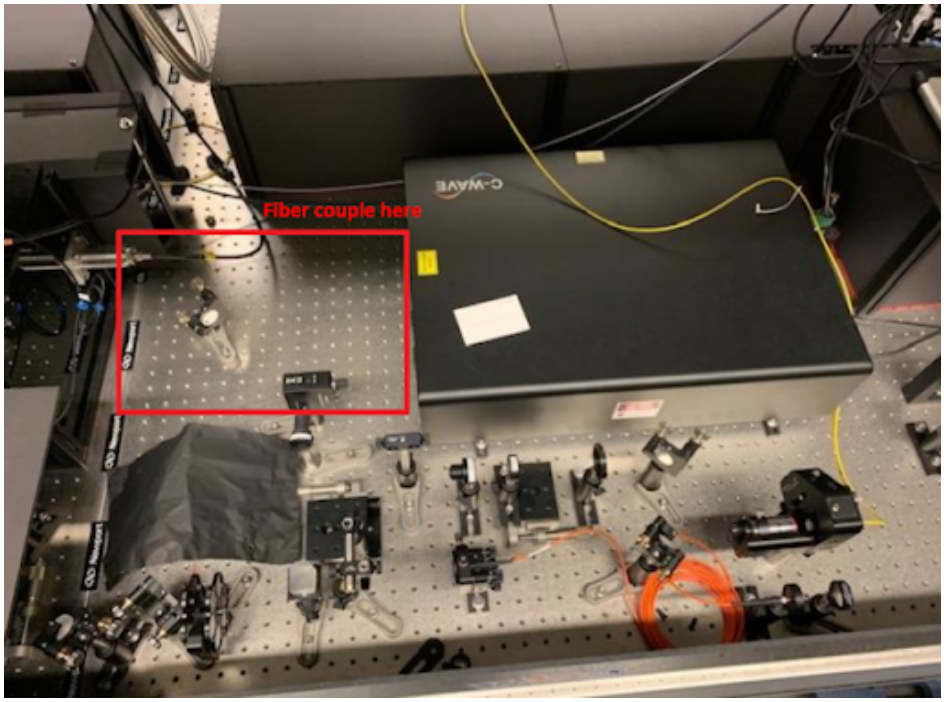

Figure E.1: **C-WAVE laser system on optics table in Bassett lab.** Future plans involve fiber coupling C-WAVE emission to the optical setup on the cryostat table.

allowing for fine photoluminescence excitation measurements.

E.2. Cryostat design

The cryostat design shown in Fig. E.2 incorporates a load lock for sample loading to allow the UHV chamber to remain shielded from contaminants during operation. Sample loading involves mounting the sample in atmosphere and loading it into the UHV chamber through a series of gate valves. The sample is mounted vertically on an adjustable sample holder, which allows for positioning of the sample within 1mm of the window surface. A turbo station from Edwards located on a pump cart (Fig. E.3) is used to pump down the load lock and UHV chamber to high vacuum ($\sim 10^{-6}$ torr). A gamma ion pump from Leybold and a non evaporable getter from SAES are then used to pump down the UHV chamber to UHV pressures ($\sim 10^{-10}$ torr). The getter assists with absorption of residual gases, such as hydrogen, which are less efficiently evacuated by the ion pump. A heating stage at the sample can reach temperatures of 450°C, allowing for in situ sample surface cleaning.

Samples are imaged through an all glass, hand blown optical cell. The optical cell is custom made

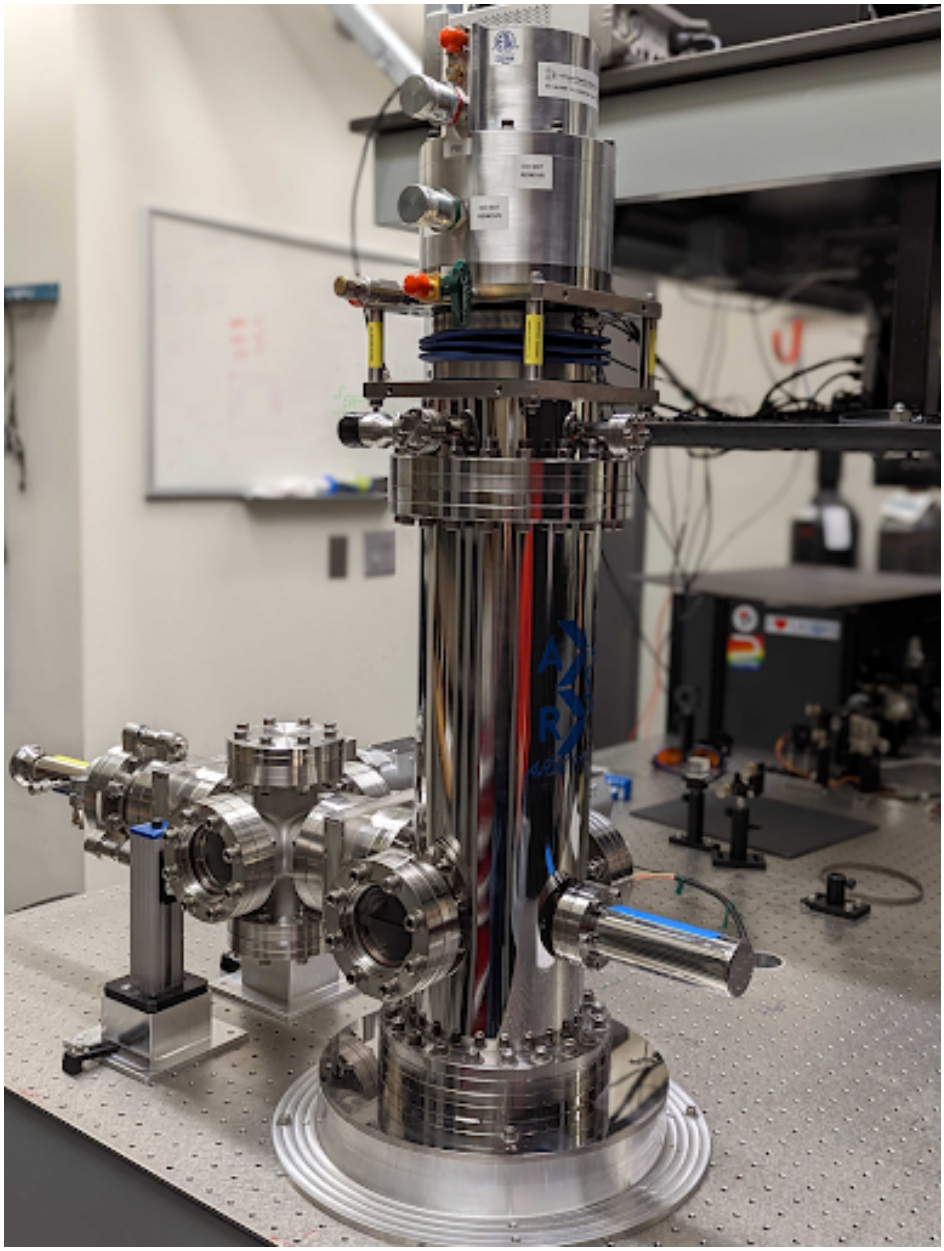

Figure E.2: **ARS cryostat on optical table in Bassett lab.** UHV chamber is vertical tower. Load lock is shown extending to the left from UHV chamber, and glass optical cell (not pictured) will be attached in the place of shipping blank shown extending to the right from the UHV chamber. Turbo pump roughing lines will be attached to 6 way cross on load lock, and gamma pump and getter will be attached to flange on far side of UHV chamber.

Figure E.3: **Edwards turbo pump and pump cart with wide range gauge attached.**

by Precision Glassmaking from quartz and UV grade silica. The cell has a 1mm thick fused silica window to allow for short-working distance, high NA confocal imaging with an external objective. The window is etched with a broadband nano-textured AR coating to minimize surface reflections. The cell's diameter of 1.5in with a 0.75in taper (see image) allows magnet access to the sample, making it possible for low temperature spin resonance experiments.

In order to achieve ultra-high vacuum, the UHV chamber must be baked out, and kept free of contaminants. The bakeout procedure involves covering the cryostat in heating tape and heating the UHV chamber to 200°C for >24 hours to allow for desorption of water from the steel. Once the chamber has been baked out, the load lock reduces exposure of the chamber to atmosphere during sample loading to decrease the need for repeated bakeouts and increase the chance of reaching UHV pressures. To use the load lock, the sample is mounted on the sample mount outside the cryostat, while the UHV chamber is pumped down to high vacuum through the load lock. A gate valve separating the load lock and UHV chamber is closed to isolate the UHV chamber, and the sample is loaded through into the load lock chamber at atmosphere. The load lock is then pumped back

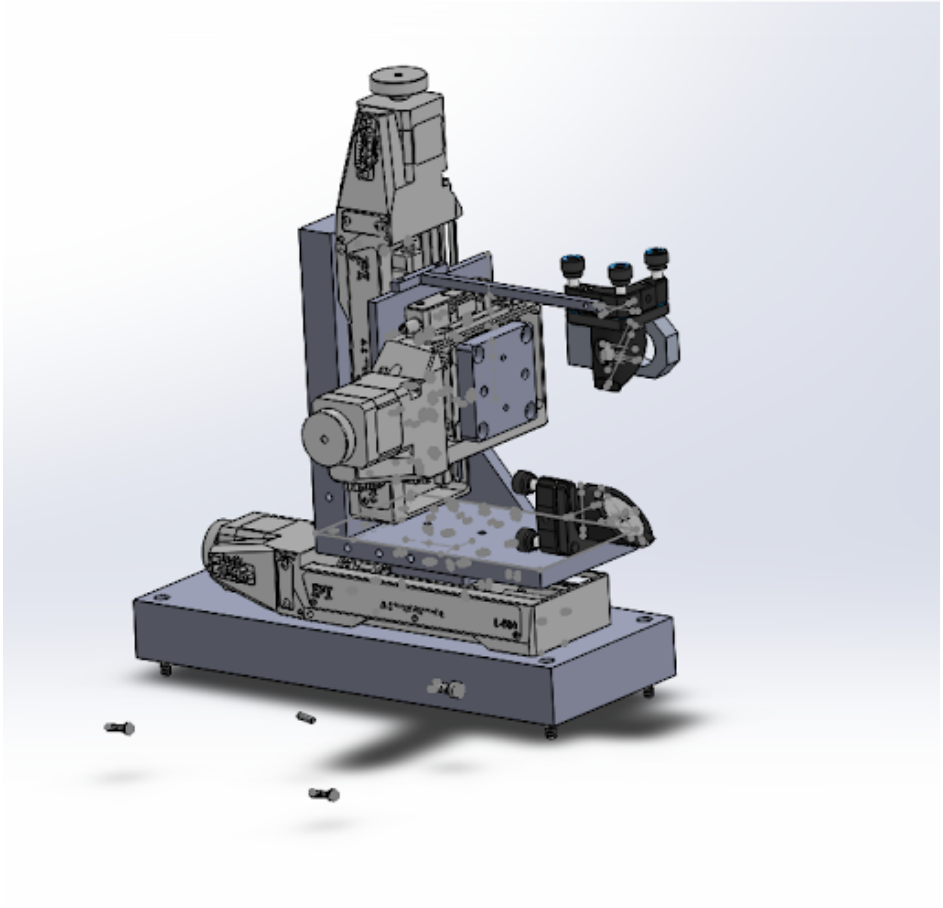

Figure E.4: **Periscope design.** The periscope is composed of of two elliptical mirrors and an objective (not pictured) mounted on x, y and z stages respectively. The excitation beam is incident to the lower elliptical mirror from the right and is translated onto the back of the objective.

to HV and the sample is loaded into the UHV chamber, where the load lock rod is disconnected and removed. Finally, the UHV chamber is pumped down to UHV with the gamma ion pump and getter that are attached to the UHV chamber.

E.3. Optical design

The confocal microscope is designed with a fixed sample and a moving objective outside the cryostat. The objective is mounted on a periscope (Fig. E.4) consisting of three linear stages from PI (Physik Instrumente), which translate the excitation beam in x, y, and z onto the back of the objective as it moves. A fast steering mirror from Optics in Motion modifies the angle of excitation incident on the back of the objective, allowing for acquisition of photoluminescence scans across tens of

microns. To shield the excitation source's stability from vibrations of the cryostat, the C-WAVE OPO laser is kept on a separate optical table and will be fiber-coupled to the cryostat table using a high power, polarization maintaining single mode fiber. A noise eater and feedback loop will be used to monitor and control the power post-fiber and attenuate high frequency noise. A variable optical-density wheel and a wide band half-wave plate will provide power and polarization control respectively. Linearly variable dichroic and long pass filters can accommodate the wide excitation range of 450-650nm. The all glass optical cell contributes aberrations that require correction due to the window thickness, tilt, and deformation when under vacuum. An objective correction collar can compensate for the 1mm thick window, which causes the most significant aberrations. However, to further correct for the window's tilt and deformation, in the future, we may incorporate adaptive optics through a deformable mirror and feedback loop.

E.4. Future directions

The tunable laser will enable broader and more in-depth exploration of new materials and defect species, facilitating the discovery and study of emitters with a larger range of excitation spectra. In conjunction with the cryostat, the C-WAVE will enable high-resolution photoluminescence excitation spectroscopy measurements for excited state fine structure mapping and the study of surface states. Future plans include incorporating microwave capabilities into the cryostat to perform spin spectroscopy and different atmospheres for various surface science studies.

BIBLIOGRAPHY

[1] M. Abobeih, Y. Wang, J. Randall, S. Loenen, C. Bradley, M. Markham, D. Twitchen, B. Terhal, and T. Taminiau. Fault-tolerant operation of a logical qubit in a diamond quantum processor. *Nature*, 606:884–889, 2022.

[2] I. Aharonovich, D. Englund, and M. Toth. Solid-state single-photon emitters. *Nat. Photonics*, 10, 2016.

[3] A. Alkauskas, Q. Yan, and C. G. Van de Walle. First-principles theory of nonradiative carrier capture via multiphonon emission. *Phys. Rev. B*, 90:075202, Aug 2014.

[4] D. Amgar, G. Yang, R. Tenne, and D. Oron. Higher-order photon correlation as a tool to study exciton dynamics in quasi-2d nanoplatelets. *Nano Letters*, 19(12):8741–8748, 2019.

[5] M. Anderson, T. Müller, J. Huwer, J. Skiba-Szymanska, A. B. Krysa, R. M. Stevenson, J. Heffernan, D. A. Ritchie, and A. J. Shields. Quantum teleportation using highly coherent emission from telecom c-band quantum dots. *npj Quantum Inf.*, 6, 2020.

[6] M. Atatüre, D. Englund, N. Vamivakas, S. Y. Lee, and J. Wrachtrup. Material platforms for spin-based photonic quantum technologies. *Nat. Rev. Mater.*, 3, 2018.

[7] P. Auburger and A. Gali. Towards ab initio identification of paramagnetic substitutional carbon defects in hexagonal boron nitride acting as quantum bits. *Physical Review B*, 104(7), 8 2021.

[8] D. D. Awschalom, L. C. Bassett, A. S. Dzurak, E. L. Hu, and J. R. Petta. Quantum spintronics: Engineering and manipulating atom-like spins in semiconductors. *Science*, 339(6124):1174–1179, 2013.

[9] S. Baier, C. E. Bradley, T. Middelburg, V. V. Dobrovitski, T. H. Taminiau, and R. Hanson. Orbital and Spin Dynamics of Single Neutrally-Charged Nitrogen-Vacancy Centers in Diamond. *Physical Review Letters*, 125(6):193601–193602, 2020.

[10] P. G. Baranov, A. P. Bundakova, A. A. Soltamova, S. B. Orlinskii, I. V. Borovykh, R. Zondervan, R. Verberk, and J. Schmidt. Silicon vacancy in sic as a promising quantum system for single-defect and single-photon spectroscopy. *Phys. Rev. B*, 83:125203, 2011.

[11] R. Barlow. A note on Delta ln L = -1/2 Errors. *arXiv e-prints*, page arXiv:physics/0403046, 2004.

[12] C. J. Barrelet, Y. Wu, D. C. Bell, and C. M. Lieber. Synthesis of cds and zns nanowires using single-source molecular precursors. *Journal of the American Chemical Society*, 125(38):11498–11499, 2003. PMID: 13129343.

[13] M. S. Barson, E. Krausz, N. B. Manson, and M. W. Doherty. The fine structure of the neutral nitrogen-vacancy center in diamond. *Nanophotonics*, 8(11):1985–1991, 2019.

[14] T. Basché, W. E. Moerner, M. Orrit, and U. P. Wild. *Single-Molecule Optical Detection, Imaging and Spectroscopy*. VCH Verlagsgesellschaft mbH, 1997.

[15] L. C. Bassett, A. Alkauskas, A. L. Exarhos, and K.-M. C. Fu. Quantum defects by design. *Nanophotonics*, 8(11):1867–1888, 2019.

[16] L. C. Bassett, F. J. Heremans, D. J. Christle, C. G. Yale, G. Burkard, B. B. Buckley, and D. D. Awschalom. Ultrafast optical control of orbital and spin dynamics in a solid-state defect. *Science*, 345(6202):1333–1337, 2014.

[17] S. L. Bayliss, D. W. Laorenza, P. J. Mintun, B. D. Kovos, D. E. Freedman, and D. D. Awschalom. Optically addressable molecular spins for quantum information processing. *Science*, 370(6522):1309–1312, 2020.

[18] K. Beha, A. Batalov, N. B. Manson, R. Bratschitsch, and A. Leitenstorfer. Optimum photoluminescence excitation and recharging cycle of single nitrogen-vacancy centers in ultrapure diamond. *Phys. Rev. Lett.*, 109:097404, Aug 2012.

[19] J. C. Bergquist, R. G. Hulet, W. M. Itano, and D. J. Wineland. Observation of quantum jumps in a single atom. *Phys. Rev. Lett.*, 57:1699–1702, Oct 1986.

[20] H. Bernien, B. Hensen, W. Pfaff, G. Koolstra, M. S. Blok, L. Robledo, T. H. Taminiau, M. Markham, D. J. Twitchen, L. Childress, et al. Heralded entanglement between solid-state qubits separated by three metres. *Nature*, 497(7447):86–90, 2013.

[21] M. Berthel, O. Mollet, G. Dantelle, T. Gacoin, S. Huant, and A. Drezet. Photophysics of single nitrogen-vacancy centers in diamond nanocrystals. *Physical Review B*, 91(3):035308, 1 2015.

[22] A. Bommer and C. Becher. New insights into nonclassical light emission from defects in multi-layer hexagonal boron nitride. *Nanophotonics*, 8(11):2041–2048, 2019.

[23] C. Bradac, T. Gaebel, N. Naidoo, M. J. Sellars, J. Twamley, L. J. Brown, A. S. Barnard, T. Plakhotnik, A. V. Zvyagin, and J. R. Rabeau. Observation and control of blinking nitrogen-vacancy centres in discrete nanodiamonds. *Nature Nanotechnology*, 5(5):345–349, 2010.

[24] C. E. Bradley, J. Randall, M. H. Abobeih, R. C. Berrevoets, M. J. Degen, M. A. Bakker, M. Markham, D. J. Twitchen, and T. H. Taminiau. A ten-qubit solid-state spin register with quantum memory up to one minute. *Phys. Rev. X*, 9:031045, 2019.

[25] D. Bradley and G. Roth. Adaptive Thresholding using the Integral Image. *Journal of Graphics Tools*, 12(2):13–21, 2007.

[26] H.-P. Breuer and F. Petruccione. *The Theory of Open Quantum Systems*. Oxford University Press, 01 2007.

[27] R. Brouri, A. Beveratos, J.-P. Poizat, and P. Grangier. Photon antibunching in the fluorescence of individual color centers in diamond. *Opt. Lett.*, 25, 2000.

[28] C. Cohen-Tannoudji and D. Guéry-Odelin. *Advances in Atomic Physics: An Overview*. World Scientific Publishing Co. Pte. Ltd., 2011.

[29] E. Z. Casalengua, J. C. L. Carreño, F. P. Laussy, and E. del Valle. Conventional and unconventional photon statistics. *Laser Photon. Rev.*, 14:014707, Jun 2020.

[30] G. Cassabois, P. Valvin, and B. Gil. Hexagonal boron nitride is an indirect bandgap semiconductor. *Nature Photonics*, 10:262–267, 2016.

[31] S. Castelletto, B. C. Johnson, V. Ivády, N. Stavrias, T. Umeda, A. Gali, and T. Ohshima. A silicon carbide room-temperature single-photon source. *Nat. Mater.*, 13, 2014.

[32] A. Chatterjee, P. Stevenson, S. D. Franceschi, A. Morello, N. P. de Leon, and F. Kuemmeth. Semiconductor qubits in practice. *Nat. Rev. Phys.*, 3, 2021.

[33] N. Chejanovsky, A. Mukherjee, J. Geng, Y.-C. Chen, Y. Kim, A. Denisenko, A. Finkler, T. Taniguchi, K. Watanabe, D. Bhaktavatsala Rao Dasari, P. Auburger, A. Gali, J. H. Smet, and J. Wrachtrup. Single-spin resonance in a van der Waals embedded paramagnetic defect. *Nature Materials*, 20:1079–1084, 2021.

[34] L. Childress, M. V. G. Dutt, J. M. Taylor, A. S. Zibrov, F. Jelezko, J. Wrachtrup, P. R. Hemmer, and M. D. Lukin. Coherent dynamics of coupled electron and nuclear spin qubits in diamond. *Science*, 314, 2006.

[35] L. Childress and R. Hanson. Diamond nv centers for quantum computing and quantum networks. *MRS Bulletin*, 38(2):134–138, 2013.

[36] C. L. Cortes, S. Adhikari, X. Ma, and S. K. Gray. Accelerating quantum optics experiments with statistical learning. *Applied Physics Letters*, 116(18):184003, 2020.

[37] J. Cramer, N. Kalb, M. Rol, B. Hensen, M. Blok, M. Markham, D. Twitchen, R. Hanson, and T. Taminiau. Repeated quantum error correction on a continuously encoded qubit by real-time feedback. *Nat. Commun.*, 7(11526), 2016.

[38] M. Davanço, C. S. Hellberg, S. Ates, A. Badolato, and K. Srinivasan. Multiple time scale blinking in InAs quantum dot single-photon sources. *Phys. Rev. B*, 89(16):161303–161308, 2014.

[39] C. L. Degen, F. Reinhard, and P. Cappellaro. Quantum sensing. *Rev. Mod. Phys.*, 89:035002,

Jul 2017.

[40] S. Dhomkar, J. Henshaw, H. Jayakumar, and C. A. Meriles. Long-term data storage in diamond. *Sci. Adv.*, 2, 2016.

[41] D. P. DiVincenzo. The physical implementation of quantum computation. *Fortschritte der Physik*, 48(9-11):771–783, 2000.

[42] M. W. Doherty, N. B. Manson, P. Delaney, F. Jelezko, J. Wrachtrup, and L. C. L. Hollenberg. The nitrogen-vacancy colour centre in diamond. *Physics Reports*, 528:1–45, 2013.

[43] P. D'Amico, A. Calzolari, A. Ruini, and A. Catellani. New energy with zns: novel applications for a standard transparent compound. *Scientific reports*, 7(1):1–9, 2017.

[44] S. E. Economou, N. Lindner, and T. Rudolph. Optically generated 2-dimensional photonic cluster state from coupled quantum dots. *Phys. Rev. Lett.*, 105:093601, Aug 2010.

[45] E. L. Elson. Fluorescence correlation spectroscopy: Past, present, future. *Biophys. J.*, 101, 2011.

[46] R. J. Epstein, F. M. Mendoza, Y. K. Kato, and D. D. Awschalom. Anisotropic interactions of a single spin and dark-spin spectroscopy in diamond. *Nature Physics*, 1:94–98, 2005.

[47] A. L. Exarhos, D. A. Hopper, R. R. Grote, A. Alkauskas, and L. C. Bassett. Optical Signatures of Quantum Emitters in Suspended Hexagonal Boron Nitride. *ACS Nano*, 11:3328–3336, 2017.

[48] A. L. Exarhos, D. A. Hopper, R. N. Patel, M. W. Doherty, and L. C. Bassett. Magnetic-field-dependent quantum emission in hexagonal boron nitride at room temperature. *Nature Communications*, 10(1):222, 12 2019.

[49] F. Diedrich and H. Walther. Nonclassical radiation of a single stored ion. *Phys. Rev. Lett.*, 58:203–206, Jan 1987.

[50] A. M. Ferrenti, N. P. de Leon, J. D. Thompson, and R. J. Cava. Identifying candidate hosts for quantum defects via data mining. *npj Comput. Mater.*, 6, 2020.

[51] R. E. Fishman, R. N. Patel, D. A. Hopper, T.-Y. Huang, and L. C. Bassett. Photon-emission-correlation spectroscopy as an analytical tool for solid-state quantum defects. *PRX Quantum*, 4:010202, Mar 2023.

[52] G. D. Fuchs, V. V. Dobrovitski, R. Hanson, A. Batra, C. D. Weis, T. Schenkel, and D. D. Awschalom. Excited-state spectroscopy using single spin manipulation in diamond. *Phys. Rev. Lett.*, 101:117601, Sep 2008.

[53] R. J. Glauber. The quantum theory of optical coherence. *Phys. Rev.*, 130, 1963.

[54] R. J. Glauber. Nobel lecture: One hundred years of light quanta. *Rev. Mod. Phys.*, 78:1267–1278, Nov 2006.

[55] M. L. Goldman, M. W. Doherty, A. Sipahigil, N. Y. Yao, S. D. Bennett, N. B. Manson, A. Kubanek, and M. D. Lukin. State-selective intersystem crossing in nitrogen-vacancy centers. *Phys. Rev. B*, 91:165201, Apr 2015.

[56] A. Gottscholl, M. Kianinia, V. Soltamov, S. Orlinskii, G. Mamin, C. Bradac, C. Kasper, K. Krambrock, A. Sperlich, M. Toth, I. Aharonovich, and V. Dyakonov. Initialization and read-out of intrinsic spin defects in a van der Waals crystal at room temperature. *Nature Materials*, 19:540–545, 2 2020.

[57] Gruber, A. Dräbenstedt, C. Tietz, L. Fleury, J. Wrachtrup, and C. V. Borczyskowski. A. scanning confocal optical microscopy and magnetic resonance on single defect centers. *Science*, 276, 1997.

[58] N.-J. Guo, S. Li, W. Liu, Y.-Z. Yang, X.-D. Zeng, S. Yu, Y. Meng, Z.-P. Li, Z.-A. Wang, L.-K. Xie, R.-C. Ge, J.-F. Wang, Q. Li, J.-S. Xu, Y.-T. Wang, J.-S. Tang, A. Gali, C.-F. Li, and G.-C. Guo. Coherent control of an ultrabright single spin in hexagonal boron nitride at room temperature. *Nature Communications*, 14(2893), 05 2023.

[59] X. Guo, Y. Ying, and L. Tong. Photonic nanowires: From subwavelength waveguides to optical sensors. *Accounts of Chemical Research*, 47(2):656–666, 2014. PMID: 24377258.

[60] M. Hauschild, T. Jentschel. Comparison of maximum likelihood estimation and chi-square statistics applied to counting experiments. *Nucl. Instrum. Methods Phys. Res. A*, 457(1):384–401, 2001.

[61] Y. M. He, Y. He, Y. J. Wei, D. Wu, M. Atatüre, C. Schneider, S. Höfling, M. Kamp, C. Y. Lu, and J. W. Pan. On-demand semiconductor single-photon source with near-unity indistinguishability. *Nat. Nanotechnol.*, 8, 2013.

[62] B. Hensen, H. Bernien, A. E. Dréau, A. Reiserer, N. Kalb, M. S. Blok, J. Ruitenberg, R. F. L. Vermeulen, R. N. Schouten, C. Abellán, W. Amaya, V. Pruneri, M. W. Mitchell, M. Markham, D. J. Twitchen, D. Elkouss, S. Wehner, T. H. Taminiau, and . R. Hanson. Loophole-free Bell inequality violation using electron spins separated by 1.3 kilometres. *Nature*, 526:682–686, 2015.

[63] S. Hepp, M. Jetter, S. L. Portalupi, and P. Michler. Semiconductor quantum dots for integrated quantum photonics. *Adv. Quantum Technol.*, 2, 2019.

[64] K. Heshami, D. G. England, P. C. Humphreys, P. J. Bustard, V. M. Acosta, J. Nunn, and B. J. Sussman. Quantum memories: emerging applications and recent advances. *J. Mod. Opt.*, 63, 2016.

[65] D. A. Hopper, R. R. Grote, A. L. Exarhos, and L. C. Bassett. Near-infrared-assisted charge control and spin readout of the nitrogen-vacancy center in diamond. *Phys. Rev. B*, 94:241201, Dec 2016.

[66] D. A. Hopper, J. D. Lauigan, T.-Y. Huang, and L. C. Bassett. Real-time charge initialization of diamond nitrogen-vacancy centers for enhanced spin readout. *Phys. Rev. Applied*, 13:024016, Feb 2020.

[67] D. A. Hopper, H. J. Shulevitz, and L. C. Bassett. Spin readout techniques of the nitrogen-vacancy center in diamond. *Micromachines*, 9, 2018.

[68] D. A. Hopper, H. J. Shulevitz, and L. C. Bassett. Spin readout techniques of the nitrogen-vacancy center in diamond. *Micromachines*, 9(9), 2018.

[69] T.-Y. Huang, R. R. Grote, S. A. Mann, D. A. Hopper, A. L. Exarhos, G. G. Lopez, A. R. Klein, E. C. Garnett, and L. C. Bassett. A monolithic immersion metalens for imaging solid-state quantum emitters. *Nature communications*, 10(1):2392, 2019.

[70] Y. Huang, E. Sutter, N. N. Shi, J. Zheng, T. Yang, D. Englund, H.-J. Gao, and P. Sutter. Reliable Exfoliation of Large-Area High-Quality Flakes of Graphene and Other Two-Dimensional Materials. *ACS Nano*, 9(11):10612–10620, 2015.

[71] D. Huber, M. Reindl, Y. Huo, H. Huang, J. S. Wildmann, O. G. Schmidt, A. Rastelli, and R. Trotta. Highly indistinguishable and strongly entangled photons from symmetric gaas quantum dots. *Nat. Commun.*, 8, 2017.

[72] I. Gopich and A. Szabo. Theory of photon statistics in single-molecule förster resonance energy transfer. *J. Chem. Phys.*, 122:014707, Dec 2005.

[73] V. Ivády, G. Barcza, G. Thiering, S. Li, H. Hamdi, J.-P. Chou, Ö. Legeza, and A. Gali. Ab initio theory of the negatively charged boron vacancy qubit in hexagonal boron nitride. *npj Computational Materials*, 6(1):1–6, 2020.

[74] T. Jaffe, N. Felgen, L. Gal, L. Kornblum, J. P. Reithmaier, C. Popov, and M. Orenstein. Deterministic Arrays of Epitaxially Grown Diamond Nanopyramids with Embedded Silicon-Vacancy Centers. *Advanced Optical Materials*, 7(2):1800715–1800722, 2019.

[75] N. R. Jungwirth, B. Calderon, Y. Ji, M. G. Spencer, M. E. Flatte, and G. D. Fuchs. Temperature Dependence of Wavelength Selectable Zero-Phonon Emission from Single Defects in Hexagonal Boron Nitride. *Nano Letters*, 16:6052–6057, 2016.

[76] N. R. Jungwirth, H.-S. Chang, M. Jiang, and G. D. Fuchs. Polarization spectroscopy of defect-based single photon sources in zno. *ACS Nano*, 10(1):1210–1215, 2016.

[77] N. R. Jungwirth and G. D. Fuchs. Optical Absorption and Emission Mechanisms of Single

Defects in Hexagonal Boron Nitride. *Physical Review Letters*, 119(5):057401, 2017.

[78] H. J. Kimble, M. Dagenais, and L. Mandel. Photon antibunching in resonance fluorescence. *Phys. Rev. Lett.*, 39:691–695, Sep 1977.

[79] E. Knill, R. Laflamme, and G. J. Milburn. A scheme for efficient quantum computation with linear optics. *Nature*, 409, 2001.

[80] H. S. Knowles, D. M. Kara, and M. Atatüre. Controlling a nuclear spin in a nanodiamond. *Phys. Rev. B*, 96:115206, Sep 2017.

[81] M. Koperski, K. Nogajewski, A. Arora, V. Cherkez, P. Mallet, J. Y. Veuillen, J. Marcus, P. Kossacki, and M. Potemski. Single photon emitters in exfoliated wse2 structures. *Nat. Nanotechnol.*, 10, 2015.

[82] C. Kurtsiefer, S. Mayer, P. Zarda, and H. Weinfurter. Stable solid-state source of single photons. *Phys. Rev. Lett.*, 85:290–293, Jul 2000.

[83] T. A. Laurence, S. Fore, and T. Huser. Fast, flexible algorithm for calculating photon correlations. *Opt. Lett.*, 31, 2006.

[84] S.-Y. Lee, M. Widmann, T. Rendler, M. W. Doherty, T. M. Babinec, S. Yang, M. Eyer, P. Siyushev, B. J. M. Hausmann, M. Loncar, M. Loncar, A. Gali, N. B. Manson, H. Fedder, and J. Wrachtrup. Readout and control of a single nuclear spin with a metastable electron spin ancilla. *Nature Nanotechnology*, 8:487–492, July 2013.

[85] M. Leifgen, T. Schröder, F. Gädeke, R. Riemann, V. Métillon, E. Neu, C. Hepp, C. Arend, C. Becher, K. Lauritsen, and O. Benson. Evaluation of nitrogen- and silicon-vacancy defect centres as single photon sources in quantum key distribution. *New J. Phys.*, 16, 2014.

[86] R. Loudon. *The Quantum Theory of Light*. Oxford University Press, 1973.

[87] M. Toth and I. Aharonovich. Single photon sources in atomically thin materials. *Annu. Rev. Phys. Chem.*, 70, 2019.

[88] C. Manzo and M. F. Garcia-Parajo. A review of progress in single particle tracking: From methods to biophysical insights. *Reports on Progress in Physics*, 78(12):124601–124629, 2015.

[89] P. C. Maurer, G. Kucsko, C. Latta, L. Jiang, N. Y. Yao, S. D. Bennett, F. Pastawski, D. Hunger, N. Chisholm, M. Markham, D. J. Twitchen, J. I. Cirac, and M. D. Lukin. Room-temperature quantum bit memory exceeding one second. *Science*, 336(6086):1283–1286, 2012.

[90] D. J. McCloskey, N. Dontschuk, D. A. Broadway, A. Nadarajah, A. Stacey, J. P. Tetienne, L. C. Hollenberg, S. Prawer, and D. A. Simpson. Enhanced Widefield Quantum Sensing with Nitrogen-Vacancy Ensembles Using Diamond Nanopillar Arrays. *ACS Applied Materials and*

Interfaces, 12(11):13421–13427, 2020.

[91] L. P. McGuinness, Y. Yan, A. Stacey, D. A. Simpson, L. T. Hall, D. Maclaurin, S. Prawer, P. Mulvaney, J. Wrachtrup, F. Caruso, et al. Quantum measurement and orientation tracking of fluorescent nanodiamonds inside living cells. *Nature nanotechnology*, 6(6):358–363, 2011.

[92] X. Michalet, R. A. Colyer, G. Scalia, S. Weiss, O. H. W. Siegmund, A. S. Tremsin, J. V. Vallerga, F. Villa, F. Guerrieri, I. Rech, A. Gulinatti, S. Tisa, F. Zappa, M. Ghioni, and S. Cova. New photon-counting detectors for single-molecule fluorescence spectroscopy and imaging. In *Advanced Photon Counting Techniques V*, volume 8033, 2011.

[93] P. Michler, A. Kiraz, C. Becher, W. V. Schoenfeld, P. M. Petroff, L. Zhang, E. Hu, and A. Imamoğlu. A quantum dot single-photon turnstile device. *Science*, 290, 2000.

[94] B. S. Miller, L. Bezinge, H. D. Gliddon, D. Huang, G. Dold, E. R. Gray, J. Heaney, P. J. Dobson, E. Nastouli, J. J. Morton, et al. Spin-enhanced nanodiamond biosensing for ultrasensitive diagnostics. *Nature*, 587(7835):588–593, 2020.

[95] B. S. Miller, L. Bezinge, H. D. Gliddon, D. Huang, G. Dold, E. R. Gray, J. Heaney, P. J. Dobson, E. Nastouli, J. J. Morton, and R. A. McKendry. Spin-enhanced nanodiamond biosensing for ultrasensitive diagnostics. *Nature*, 587, 2020.

[96] N. Morioka, C. Babin, R. Nagy, I. Gediz, E. Hesselmeier, D. Liu, M. Joliffe, M. Niethammer, D. Dasari, V. Vorobyov, R. Kolesov, R. Stöhr, J. Ul-Hassan, N. T. Son, T. Ohshima, P. Udvarhelyi, G. Thiering, A. Gali, J. Wrachtrup, and F. Kaiser. Spin-controlled generation of indistinguishable and distinguishable photons from silicon vacancy centres in silicon carbide. *Nat. Commun.*, 11, 2020.

[97] L. R. Narun, R. E. K. Fishman, H. J. Shulevitz, R. N. Patel, and L. C. Bassett. Efficient analysis of photoluminescence images for the classification of single-photon emitters. *ACS Photonics*, 9(11):3540–3549, 2022.

[98] E. Neu, M. Agio, and C. Becher. Photophysics of single silicon vacancy centers in diamond: implications for single photon emission. *Opt. Express*, 20(18):19956–19971, Aug 2012.

[99] E. Neu, M. Fischer, S. Gsell, M. Schreck, and C. Becher. Fluorescence and polarization spectroscopy of single silicon vacancy centers in heteroepitaxial nanodiamonds on iridium. *Phys. Rev. B*, 84:205211, Nov 2011.

[100] M. Nirmal, B. O. Dabbousi, M. G. Bawendi, J. J. Macklin, J. K. Trautman, T. D. Harris, and L. E. Brus. Fluorescence intermittency in single cadmium selenide nanocrystals. *Nature*, 383(6603):802–804, 1996.

[101] C. Palacios-Berraquero. *Atomically-Thin Quantum Light Emitting Diodes*, pages 71–89. Springer International Publishing, Cham, 2018.

[102] R. N. Patel, R. E. K. Fishman, T.-Y. Huang, J. A. Gusdorff, D. A. Fehr, D. A. Hopper, S. A. Breitweiser, B. Porat, M. E. Flatté, and L. C. Bassett. Room temperature dynamics of an optically addressable single spin in hexagonal boron nitride, 2023.

[103] R. N. Patel, D. A. Hopper, J. A. Gusdorff, M. E. Turiansky, T.-Y. Huang, R. E. K. Fishman, B. Porat, C. G. Van de Walle, and L. C. Bassett. Probing the optical dynamics of quantum emitters in hexagonal boron nitride. *PRX Quantum*, 3:030331, Sep 2022.

[104] M. Pfender, N. Aslam, P. Simon, D. Antonov, G. Thiering, S. Burk, F. Fávaro de Oliveira, A. Denisenko, H. Fedder, J. Meijer, J. A. Garrido, A. Gali, T. Teraji, J. Isoya, M. W. Doherty, A. Alkauskas, A. Gallo, A. Grüneis, P. Neumann, and J. Wrachtrup. Protecting a diamond quantum memory by charge state control. *Nano Letters*, 17(10):5931–5937, 2017. PMID: 28872881.

[105] M. Pompili, S. L. Hermans, S. Baier, H. K. Beukers, P. C. Humphreys, R. N. Schouten, R. F. Vermeulen, M. J. Tiggelman, L. dos Santos Martins, B. Dirkse, S. Wehner, and R. Hanson. Realization of a multinode quantum network of remote solid-state qubits. *Science*, 372, 2021.

[106] R. Hanbury Brown and R. Q. Twiss. Correlation between photons in two coherent beams of light. *Nature*, 177, 1956.

[107] M. Radtke, E. Bernardi, A. Slablab, R. Nelz, and E. Neu. Nanoscale sensing based on nitrogen vacancy centers in single crystal diamond and nanodiamonds: Achievements and challenges. *Nano Futures*, 3, 2019.

[108] M. Radulaski, M. Widmann, M. Niethammer, J. L. Zhang, S.-Y. Lee, T. Rendler, K. G. Lagoudakis, N. T. Son, E. Janzén, T. Ohshima, J. Wrachtrup, and J. Vučković. Scalable quantum photonics with single color centers in silicon carbide. *Nano Lett.*, 17(3):1782–1786, 2017.

[109] L. Razinkovas, M. W. Doherty, N. B. Manson, C. G. Van de Walle, and A. Alkauskas. Vibrational and vibronic structure of isolated point defects: The nitrogen-vacancy center in diamond. *Phys. Rev. B*, 104:045303, Jul 2021.

[110] T. Rendler, J. Neburkova, O. Zemek, J. Kotek, A. Zappe, Z. Chu, P. Cigler, and J. Wrachtrup. Optical imaging of localized chemical events using programmable diamond quantum nanosensors. *Nature communications*, 8(1):14701, 2017.

[111] L. Robledo, L. Childress, H. Bernien, B. Hensen, P. F. Alkemade, and R. Hanson. High-fidelity projective read-out of a solid-state spin quantum register. *Nature*, 477, 2011.

[112] L. V. H. Rodgers, L. B. Hughes, M. Xie, P. C. Maurer, S. Kolkowitz, A. C. B. Jayich, and N. P. de Leon. Materials challenges for quantum technologies based on color centers in diamond. *MRS Bull.*, 46:623–633, 2021.

[113] L. J. Rogers, K. D. Jahnke, M. W. Doherty, A. Dietrich, L. P. McGuinness, C. Müller, T. Teraji, H. Sumiya, J. Isoya, N. B. Manson, and F. Jelezko. Electronic structure of the negatively charged silicon-vacancy center in diamond. *Phys. Rev. B*, 89:235101, Jun 2014.

[114] M. Ruf, N. H. Wan, H. Choi, D. Englund, and R. Hanson. Quantum networks based on color centers in diamond. *Journal of Applied Physics*, 130(7):070901, 08 2021.

[115] L. Schermelleh, A. Ferrand, T. Huser, C. Eggeling, M. Sauer, O. Biehlmaier, and G. P. Drummen. Super-resolution microscopy demystified. *Nature Cell Biology*, 21(1):72–84, 2019.

[116] M. Scholz, T. Aichele, S. Ramelow, and O. Benson. Deutsch-jozsa algorithm using triggered single photons from a single quantum dot. *Phys. Rev. Lett.*, 96:180501, May 2006.

[117] B. Schuler, K. A. Cochrane, C. Kastl, E. S. Barnard, E. Wong, N. J. Borys, A. M. Schwartzberg, D. F. Ogletree, F. J. G. D. Abajo, and A. Weber-Bargioni. Electrically driven photon emission from individual atomic defects in monolayer ws2. *Sci. Adv.*, 6, 2020.

[118] T. F. Segawa and R. Igarashi. Nanoscale quantum sensing with nitrogen-vacancy centers in nanodiamonds – a magnetic resonance perspective. *Progress in Nuclear Magnetic Resonance Spectroscopy*, 134-135:20–38, 2023.

[119] P. Senellart, G. Solomon, and A. White. High-performance semiconductor quantum-dot single-photon sources. *Nat. Nanotechnol.*, 12, 2017.

[120] G. C. Shan, Z. Q. Yin, C. H. Shek, and W. Huang. Single photon sources with single semiconductor quantum dots. *Front. Phys.*, 9, 2014.

[121] B. J. Shields, Q. P. Unterreithmeier, N. P. de Leon, H. Park, and M. D. Lukin. Efficient readout of a single spin state in diamond via spin-to-charge conversion. *Phys. Rev. Lett.*, 114:136402, Mar 2015.

[122] H. J. Shulevitz, T.-Y. Huang, J. Xu, S. J. Neuhaus, R. N. Patel, Y. C. Choi, L. C. Bassett, and C. R. Kagan. Template-assisted self-assembly of fluorescent nanodiamonds for scalable quantum technologies. *ACS Nano*, 16(2):1847–1856, 2022.

[123] U. Sinha, S. N. Sahoo, A. Singh, K. Joarder, R. Chatterjee, and S. Chakraborti. Single-photon sources. *Opt. Photon. News*, 30(9):32–39, Sep 2019.

[124] P. Siyushev, M. Nesladek, E. Bourgeois, M. Gulka, J. Hruby, T. Yamamoto, M. Trupke, T. Teraji, J. Isoya, and F. Jelezko. Photoelectrical imaging and coherent spin-state readout of single nitrogen-vacancy centers in diamond. *Science*, 363, 2019.

[125] O. O. Soykal, P. Dev, and S. E. Economou. Silicon vacancy center in 4*h*-sic: Electronic structure and spin-photon interfaces. *Phys. Rev. B*, 93:081207(R), Feb 2016.

[126] P. L. Stanwix, L. M. Pham, J. R. Maze, D. Le Sage, T. K. Yeung, P. Cappellaro, P. R. Hemmer, A. Yacoby, M. D. Lukin, and R. L. Walsworth. Coherence of nitrogen-vacancy electronic spin ensembles in diamond. *Phys. Rev. B*, 82:201201, Nov 2010.

[127] H. L. Stern, Q. Gu, J. Jarman, S. Eizagirre Barker, N. Mendelson, D. Chugh, S. Schott, H. H. Tan, H. Sirringhaus, I. Aharonovich, and M. Atatüre. Room-temperature optically detected magnetic resonance of single defects in hexagonal boron nitride. *Nature Communications*, 13(618), 2022.

[128] M. J. Stevens, S. Glancy, S. W. Nam, and R. P. Mirin. Third-order antibunching from an imperfect single-photon source. *Opt. Express*, 22(3):3244–3260, Feb 2014.

[129] M. J. Stevens, R. H. Hadfield, R. E. Schwall, S. W. Nam, R. P. Mirin, and J. A. Gupta. Fast lifetime measurements of infrared emitters using a low-jitter superconducting single-photon detector. *Appl. Phys. Lett.*, 89, 2006.

[130] W. Sun. nanocluster/photons. https://github.com/nanocluster/photons, 2019.

[131] T. Zhong and P. Goldner. Emerging rare-earth doped material platforms for quantum nanophotonics. *Nanophotonics*, 2019.

[132] H. Takashima, H. Maruya, K. Ishihara, T. Tashima, K. Shimazaki, A. W. Schell, T. T. Tran, I. Aharonovich, and S. Takeuchi. Determination of the dipole orientation of single defects in hexagonal boron nitride. *ACS Photonics*, 7(8):2056–2063, 2020.

[133] K. Takemoto, Y. Nambu, T. Miyazawa, Y. Sakuma, T. Yamamoto, S. Yorozu, and Y. Arakawa. Quantum key distribution over 120km using ultrahigh purity single-photon source and superconducting single-photon detectors. *Sci. Rep.*, 5, 2015.

[134] T. H. Taminiau, J. J. T. Wagenaar, T. van der Sar, F. Jelezko, V. V. Dobrovitski, and R. Hanson. Detection and control of individual nuclear spins using a weakly coupled electron spin. *Phys. Rev. Lett.*, 109:137602, Sep 2012.

[135] J. M. Taylor, P. Cappellaro, L. Childress, L. Jiang, D. Budker, P. R. Hemmer, A. Yacoby, R. Walsworth, and M. D. Lukin. High-sensitivity diamond magnetometer with nanoscale resolution. *Nat. Phys.*, 4, 2008.

[136] J. Tetienne, L. Rondin, P. Spinicelli, M. Chipaux, T. Debuisschert, J. Roch, and V. Jacques. Magnetic-field-dependent photodynamics of single nv defects in diamond: an application to qualitative all-optical magnetic imaging. *New Journal of Physics*, 14(10):103033, 2012.

[137] S. E. Thomas, M. Billard, N. Coste, S. C. Wein, Priya, H. Ollivier, O. Krebs, L. Tazaïrt, A. Harouri, A. Lemaitre, I. Sagnes, C. Anton, L. Lanco, N. Somaschi, J. C. Loredo, and P. Senellart. Bright polarized single-photon source based on a linear dipole. *Phys. Rev. Lett.*, 126:233601, Jun 2021.

[138] S. M. Thompson, C. Şahin, S. Yang, M. E. Flatté, C. B. Murray, L. C. Bassett, and C. R. Kagan. Red emission from copper-vacancy color centers in zinc sulfide colloidal nanocrystals. *ACS Nano*, 17(6):5963–5973, 2023. PMID: 36892080.

[139] C. Timm. Random transition-rate matrices for the master equation. *Phys. Rev. E*, 80:021140, Aug 2009.

[140] T. T. Tran, K. Bray, M. J. Ford, M. Toth, and I. Aharonovich. Quantum emission from hexagonal boron nitride monolayers. *Nat. Nanotechnol.*, 11, 2016.

[141] R. Ulbricht and Z.-H. Loh. Excited-state lifetime of the Nv^- infrared transition in diamond. *Phys. Rev. B*, 98:094309, Sep 2018.

[142] E. Van Oort, N. Manson, and M. Glasbeek. Optically detected spin coherence of the diamond nv centre in its triplet ground state. *Journal of Physics C: Solid State Physics*, 21(23):4385, 1988.

[143] R. Vocke Jr. Atomic weights of the elements 1997. *Pure and Applied Chemistry*, 71(8):1593–1607, 1999.

[144] M. Wahl. Technical notes: Time-correlated single photon counting. PicoQuant GmbH, 2014.

[145] D. F. Walls. Evidence for the quantum nature of light. *Nature*, 280, 1979.

[146] M. Widmann, S. Y. Lee, T. Rendler, N. T. Son, H. Fedder, S. Paik, L. P. Yang, N. Zhao, S. Yang, I. Booker, A. Denisenko, M. Jamali, S. A. Momenzadeh, I. Gerhardt, T. Ohshima, A. Gali, E. Janzén, and J. Wrachtrup. Coherent control of single spins in silicon carbide at room temperature. *Nat. Mater.*, 14, 2015.

[147] D. Wirtitsch, G. Wachter, S. Reisenbauer, M. Gulka, V. Ivády, F. Jelezko, A. Gali, M. Nesladek, and M. Trupke. Exploiting ionization dynamics in the nitrogen vacancy center for rapid, high-contrast spin, and charge state initialization. *Phys. Rev. Res.*, 5:013014, Jan 2023.

[148] G. Wolfowicz, F. J. Heremans, C. P. Anderson, S. Kanai, H. Seo, A. Gali, G. Galli, and D. D. Awschalom. Quantum guidelines for solid-state spin defects. *Nature Reviews Materials*, 6:906–925, 2021.

[149] X. Liu and M.C. Hersam. 2d materials for quantum information science. *Nat. Rev. Mater.*, 4, 2019.

[150] Y. Arakawa and M. J. Holmes. Progress in quantum-dot single photon sources for quantum information technologies: A broad spectrum overview. *Appl. Phys. Rev.*, 7, 2020.

[151] B. Zhang, J. Zerubia, and J. C. Olivo-Marin. Gaussian approximations of fluorescence microscope point-spread function models. *Applied Optics*, 46(10):1819–1829, 2007.

[152] T. Zhang, G. Pramanik, K. Zhang, M. Gulka, L. Wang, J. Jing, F. Xu, Z. Li, Q. Wei, P. Cigler, and Z. Chu. Toward quantitative bio-sensing with nitrogen–vacancy center in diamond. *ACS Sensors*, 6(6):2077–2107, 2021. PMID: 34038091.

[153] J. Ziegler, A. Blaikie, A. Fathalizadeh, D. Miller, F. S. Yasin, K. Williams, J. Mohrhardt, B. J. McMorran, A. Zettl, and B. Alema. Single-Photon Emitters in Boron Nitride Nanococoons. *Nano Letters*, 18(4):2683–2688, 2018.

[154] Ádám Gali. Ab initio theory of the nitrogen-vacancy center in diamond. *Nanophotonics*, 8(11):1907–1943, 2019.